



Theses and Dissertations

2013-12-01

Ferritin-Based Photo-Oxidation of Biomass for Nanoparticle Synthesis, Bioremediation, and Hydrogen Evolution

Oscar Petrucci
Brigham Young University - Provo

Follow this and additional works at: <https://scholarsarchive.byu.edu/etd>



Part of the [Biochemistry Commons](#), and the [Chemistry Commons](#)

BYU ScholarsArchive Citation

Petrucci, Oscar, "Ferritin-Based Photo-Oxidation of Biomass for Nanoparticle Synthesis, Bioremediation, and Hydrogen Evolution" (2013). *Theses and Dissertations*. 4308.
<https://scholarsarchive.byu.edu/etd/4308>

This Dissertation is brought to you for free and open access by BYU ScholarsArchive. It has been accepted for inclusion in Theses and Dissertations by an authorized administrator of BYU ScholarsArchive. For more information, please contact scholarsarchive@byu.edu, ellen_amatangelo@byu.edu.

Ferritin-Based Photo-Oxidation of Biomass for Nanoparticle Synthesis,
Bioremediation, and Hydrogen Evolution

Oscar D. Petrucci

A dissertation submitted to the faculty of
Brigham Young University
in partial fulfillment of the requirements for the degree of

Doctor of Philosophy

Richard K. Watt, Chair
Roger G. Harrison
John T. Prince
Jeffrey K. Farrer
John C. Price

Department of Chemistry and Biochemistry

Brigham Young University

December 2013

Copyright © 2013 Oscar D. Petrucci

All Rights Reserved

ABSTRACT

Ferritin-Based Photo-Oxidation of Biomass for Nanoparticle Synthesis, Bioremediation, and Hydrogen Evolution

Oscar D. Petrucci

Department of Chemistry and Biochemistry, BYU

Doctor of Philosophy

The cell is the basic unit of all living organisms. It is an amazing machine capable of self-replicating, growing, and synthesizing and shuttling thousands of compounds. To perform all of these activities the cell needs energy. The original source of energy for all living beings is the Sun. The energy of the sun is collected by the autotrophs (mostly plants) through photosynthesis and stored in the chemical bonds of carbohydrates and lipids through carboxylic acid intermediates; animals use these compounds to obtain the energy for their cells. Most of the energy extracted by the cell comes from the citric acid cycle. Therefore, two crucial energy transfer checkpoints are photosynthesis and citric acid cycle.

With growing need for energy, the limited supply of fossil fuel, and the search for a cleaner environment, scientists have turned to the Sun (directly or indirectly through wind, tides, biomass, etc.) to satisfy the needs of modern society trying to reach the dual Holy Grail of energy: harvesting energy through Artificial Photosynthesis and Low Temperature Biomass Oxidation.

This work represents one more step toward reaching these Holy Grails.

The core reagent used in our technique is ferritin. Ferritin recapitulates some of the essential features of a plant cell: it contains a semiconductor capable of charge separation, like chlorophyll, acts as a membrane to isolate compartments, and has an enzymatic activity that prevents charge build up and oxidative damage.

The energy absorbed by ferritin from the artificial “solar” radiation is used to extract reducing equivalents from stable and partially oxidized compounds, mainly carboxylic acids. The energized electrons produced are then used for a number of technical applications, from synthesis of catalytically active nanoparticles, to reductive precipitation of contaminant heavy metals (i.e.: mercury), to hydrogen evolution.

Keywords: ferritin, artificial photosynthesis, biomass, carboxylic acids, photochemistry, photo catalyst, photosynthesis, renewable energy, gold nanoparticles, mercury, decontamination, bioremediation, silver nanoparticles, hydrogen evolution, hydrogen catalyst, methyl viologen, platinum nanoparticles, palladium nanoparticles.

ACKNOWLEDGEMENTS

I dedicate this work to my wife Kristin, who with patience and love sustained me over the last three years; also to my parents, who taught me to work hard, be patient, forgive, give to all with open heart, and trust in the Lord.

Dedico quest'opera a mia moglie Kristin, che con pazienza e amore mi ha sostenuto durante questi ultimi tre anni; la dedico anche ai miei genitori, che mi hanno insegnato a lavorare duro, a perdonare, a dare a tutti, a farlo di cuore e a confidare nel Signore.

TABLE OF CONTENTS

CHAPTER 1: Ferritin as a Model for Developing 3rd Generation Nano Architecture	
Inorganic/Organic	1
Hybrid Photo Catalysts for Energy Conversion.....	1
Abstract.....	1
Introduction.....	2
1. The development of inexpensive, abundant, non-toxic charge separation catalysts that absorb visible light;.....	12
2. Development of stable catalysts with high turnover numbers that possess self-healing mechanisms to prevent photo corrosion.	15
3. Development of photo catalysts capable of oxidizing a broad range of electron donors.	16
4. Developing Hybrid organic/inorganic nano architectures that bridge charge flow from electron donors, through the catalyst to electron acceptors.	17
Future Directions	19
References.....	22
Chapter 2: Mechanistic Study of Ferritin Photochemistry	30
Introduction.....	30
Discussion.....	35
Core Size –Coordination Numbers	35
Core Size –The Capacitor Theory.....	38
Core Size –Quantum Confinement and Band Gap	41
Phosphate Layer.....	41

The Influence of Oxygen on the Lag Phase.....	43
Core Mineral Composition	43
Core Crystallinity.....	43
Calculating the Nucleation Event Time Point	46
Conclusions.....	47
References.....	49
CHAPTER 3: A Ferritin Mediated Photo Chemical Method to Synthesize Biocompatible Catalytically Active Gold Nanoparticles: Size Control Synthesis for Small (~2 nm), Medium (~7 nm) or Large (~17 nm) Nanoparticles	51
Abstract.....	51
Introduction.....	53
Materials and Methods.....	59
Catalytic properties of the AuNPs	61
Results.....	62
Varying Ftn Concentrations.....	62
Varying Citrate Concentrations	64
Varying Gold Concentrations	67
Effect of ferritin iron core size and phosphate content on photo catalysis	70
Oxidation state of the gold ions	75
Catalytic Activity of the AuNPs	77
Conclusions.....	78
References.....	84

Chapter 4: Precipitation of Mercury from Aqueous Solutions Using a Ferritin Photochemical

Reaction	88
Abstract	88
Introduction.....	89
Materials and Methods.....	93
Quantitative Analysis of Hg.....	95
UV-Vis spectrophotometry.....	95
Transmission electron microscopy and energy-dispersive X-ray spectroscopy.....	95
X-ray photoelectron spectroscopy	95
X-ray diffraction	96
Gas chromatography-Mass Spectrometry.....	96
Quantitative Analysis of Hg.....	97
Inductively coupled plasma optical emission spectroscopy	97
Results.....	97
Pathways of Hg(II) Precipitation	98
Reactions in the Absence of Chloride Ions.....	98
Reactions in the Presence of Chloride.....	102
Studying Intermediates to Understand the Mechanism of Hg(II) Photo Reduction.....	102
Organomercury Compounds.....	108
Quantitative Analysis on the Photo Catalysis Methods for Hg(II) Precipitation.....	110
Stability of Ferritin as a Photo Catalyst	110
Conclusions.....	116

References.....	118
CHAPTER 5: A Ferritin Photochemical Synthesis of Monodispersed Silver Nanoparticles that Possess Antimicrobial Properties.....	
Abstract.....	120
Introduction.....	121
Materials and Methods.....	123
Bacterial Growth Minimal Inhibitory Concentration Test.....	124
Results.....	125
Conclusions.....	130
References.....	133
Chapter 6: A Ferritin Photochemical Synthesis of Monodispersed Platinum and Palladium Nanoparticles	
Abstract.....	135
Introduction.....	136
Materials and Methods.....	136
Results.....	137
Conclusions.....	141
References.....	142
Chapter 7: Photochemical Evolution of Hydrogen by Methyl Viologen	
Abstract.....	143
Introduction.....	144
Materials and Methods.....	145

Results.....	147
Conclusions.....	163
References.....	165
Chapter 8: Conclusions and Outlook	167

CHAPTER 1: FERRITIN AS A MODEL FOR DEVELOPING 3RD GENERATION NANO ARCHITECTURE INORGANIC/ORGANIC HYBRID PHOTO CATALYSTS FOR ENERGY CONVERSION

This chapter has been reformatted for the dissertation but was previously published online: R.K. Watt, O. Petrucci, T. Smith. *Catal. Sci. Technol.*, 2013, 3 (12), 3103–3110.

Abstract

Solar power is the best option to replace fossil fuels to meet global energy demands. Current photovoltaic and artificial photosynthetic systems require improvements and include the development of: 1) inexpensive, abundant, non-toxic charge separation catalysts that absorb visible light; 2) stable catalysts with high turnover numbers that possess self-healing mechanisms to prevent photo corrosion; 3) catalysts capable of oxidizing a broad range of electron donors; and 4) hybrid organic/inorganic nano architectures that bridge charge flow from electron donors to electron acceptors. The ferritin nanocage is a model system of such an organic/inorganic hybrid catalyst capable of overcoming these photochemical limitations.

Introduction

The driving force to develop more efficient PV systems to replace fossil fuels has increased because of: 1) environmental problems related to CO₂ emissions; 2) dwindling fossil fuel reserves; and 3) political unrest in countries that have abundant oil supplies. These issues have caused an increase in market demand for renewable energy and have driven many advances in photovoltaic systems ¹.

The first commercially available photovoltaic (PV) systems or first-generation PV systems were constructed using silicon technology and used monocrystalline silicon, polycrystalline silicon or amorphous silicon (Fig 1A) ^{2, 3}. Silicon is not the best material for photovoltaic systems, because it requires thick layers ~100 μm for efficient light absorption, which increases the cost of the PV cells, but silicon-processing technologies allowed it to be a dominant material in early PV technology ³⁻⁵. Typical amorphous and polycrystalline silicon systems are less efficient but monocrystalline systems are more efficient (28%) ² and are reaching their theoretical limit of 31% ⁶.

Second-generation PV charge separation catalysts have been synthesized using thin films to try to produce PV cells at lower cost than silicon. Some of the most promising materials include cadmium telluride, gallium arsenide and copper indium gallium selenide ¹ (Fig 1B). These advances have provided new competitors for silicon PV systems as the efficiencies of these second-generation PV materials have recently passed 20 % ^{4, 7}. However, the low natural abundance of the elements used for these second-generation solar cells and toxicity issues make these photo catalysts unsuitable for large-scale mass production to replace fossil fuels ⁷. Other advances in the second-generation solar cell arena include, dye sensitized solar cells (DSSC),

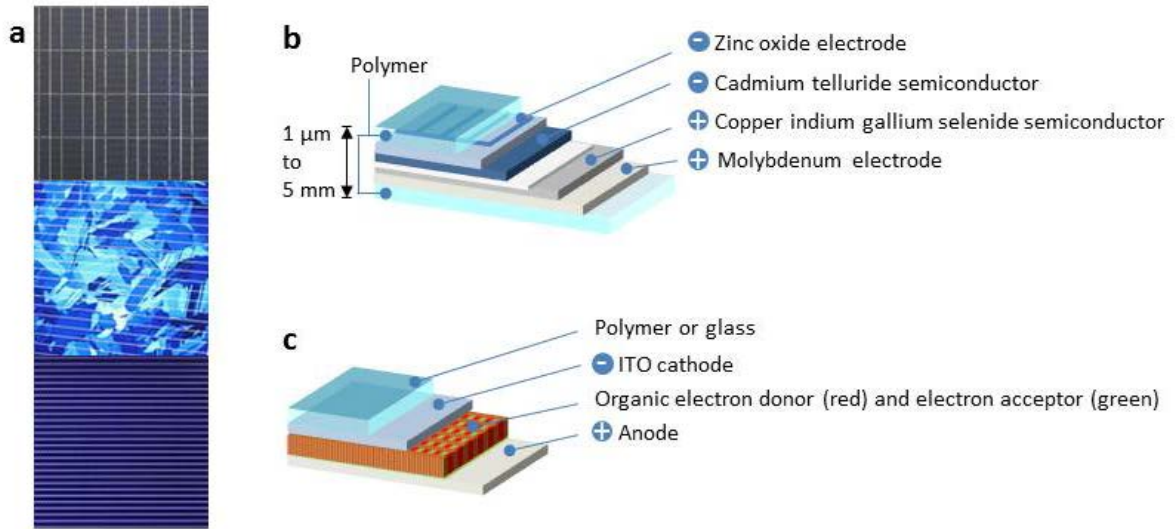


Figure 1-1. (a) Silicon solar cells: amorphous (top), polycrystalline (center), monocrystalline (bottom).
 (b) Thin film solar cell. (c) Organic solar cell.

with efficiencies around 10 % and organic solar cells (OSC) (Fig. 1C) with efficiencies over 10 %⁸⁻¹⁰. These advances are reaching efficiencies that make these second-generation PV systems competitive with silicon^{1, 4, 7, 10}.

Future PV systems must possess increased efficiency and lower production costs before solar power can replace fossil fuels. To achieve these goals, third-generation PV systems are focusing on nano-structure based devices and nano-material architectures that possess unique properties to maximize light harvesting and facilitate energy conversion reactions¹. Several promising technologies for third-generation PV systems include colloidal quantum dot PV systems where the quantum dots are imbedded in membranes¹¹, or hybrid systems composed of organic and inorganic mixtures^{1, 12}. Hybrid chemical/biological PV systems are one area of active research.

A comparison of photosynthesis to PV systems was performed to better understand how nature harvests light from the sun^{13, 14}. The ultimate goal is to mimic photosynthesis and oxidize water but it should be noted that Nature did not start by oxidizing water but started with more easily oxidized molecules. An example of this evolutionary process is purple photosynthetic bacteria where the electron donors were molecules such as sulfur-containing molecules, hydrogen or other organic molecules. Efforts to create artificial systems to oxidize biomass are following this same strategy.

Using the model provided by Nature, bio photo electrochemical fuel cells have been successfully developed^{15, 16}. Algae and cyanobacteria were used to harvest solar energy and transfer it to electron acceptors present in the growth medium^{17, 18}. Other systems include hybrid dye sensitized solar cells (DSSC) where enzymes break down biomass and convert oxidized substrates into electron rich molecules that subsequently donate electrons to the photo

anode in the fuel cells ¹⁹. These systems range from poor efficiency (0.3 - 2 %) to efficiencies similar to commercial PV systems (12 %). However, a major drawback to bio photo electrochemical fuel cells is the poor stability of the enzymes or cyanobacteria that act as catalysts.

The transition from biomass oxidation to water oxidation is a priority because of the abundance of water as a substrate and production of hydrogen as a product. Hydrogen represents a fuel that can be stored for use when solar radiation is not available (night) or less abundant (cloudy days or winter) ²⁰. We briefly outline efforts to develop water oxidation catalysts and how they are coupled to light harvesting systems to produce hydrogen gas.

A ruthenium complex known as the blue dimer was the first synthetic water oxidation catalyst ²¹. Since that seminal study, water oxidation has been observed with a variety of catalysts. Our intent here is not to review the field of water oxidation catalyst as that has been done in several recent reviews ^{14, 22-25}. However, we emphasize that many of these successful studies have used expensive catalysts or noble metal catalysts that will be cost prohibitive to mass-produce for global solar energy.

In contrast, the last 5 years have produced remarkable breakthroughs in water oxidation catalysts using earth abundant transition metals ^{20, 26-33}. This has driven a renewed effort for studying these metals and their metal oxides, sulfides, phosphates and borates, for oxygen and hydrogen evolution. Remarkably these catalysts have been coupled to light harvesting devices and the solar energy has been harvested and used to drive water splitting ^{23, 30}.

The successful synthesis of third-generation PV systems is proposed to require a combination of organic/inorganic hybrid nanomaterials made from earth abundant transition metals. To be successful, these third generation catalysts must overcome several significant

challenges to achieve global solar energy. First, earth abundant catalysts need to be developed that will absorb visible light because 44% of solar energy is found in the visible region of the spectrum. One solution is to develop stacked cells (see Fig. 2A) with a variety of light harvesting molecules that absorb different wavelengths of light^{34, 35}. A second method to increase efficiency is through carrier multiplication or allowing each photon to cause multiple electronic excitation events. Schaller et al. reported carrier multiplication reactions with PbS and PbSe that maximize the number of electrons that are excited (up to seven excitons by a single photon) (Fig 2B)³⁶. Second, production of stable catalysts with high turnover numbers is required. One method to improve turnover numbers is to develop self-healing catalysts to maximize catalyst stability²⁸. Third, biomass oxidation may be an intermediate between current systems and water oxidation. The development of catalysts capable of oxidizing a broad range of electron donors such as glucose or glycerol may rapidly enhance progress towards the ultimate goal of water oxidation. A fourth goal is to increase the rate and efficiency of electron transfer out of the charge transfer catalyst to the electron acceptor in order to prevent charge recombination. One mechanism to do this is to tether the charge separation catalyst directly to the electron harvesting molecules so that the excited electrons can be siphoned away from the charge separation catalyst to drive the reaction forward. The development of molecules or architectures that bridge the electron donor and electron acceptor molecules to limit recombination and improve electron transfer to the electron acceptor is required^{14, 36, 37}.

In this review we outline how ferritin possesses important properties that can be used as a model system for the development of future third generation photo catalysts. Ferritin is a protein complex composed of 24 similar polypeptide subunits that assemble into a hollow spherical

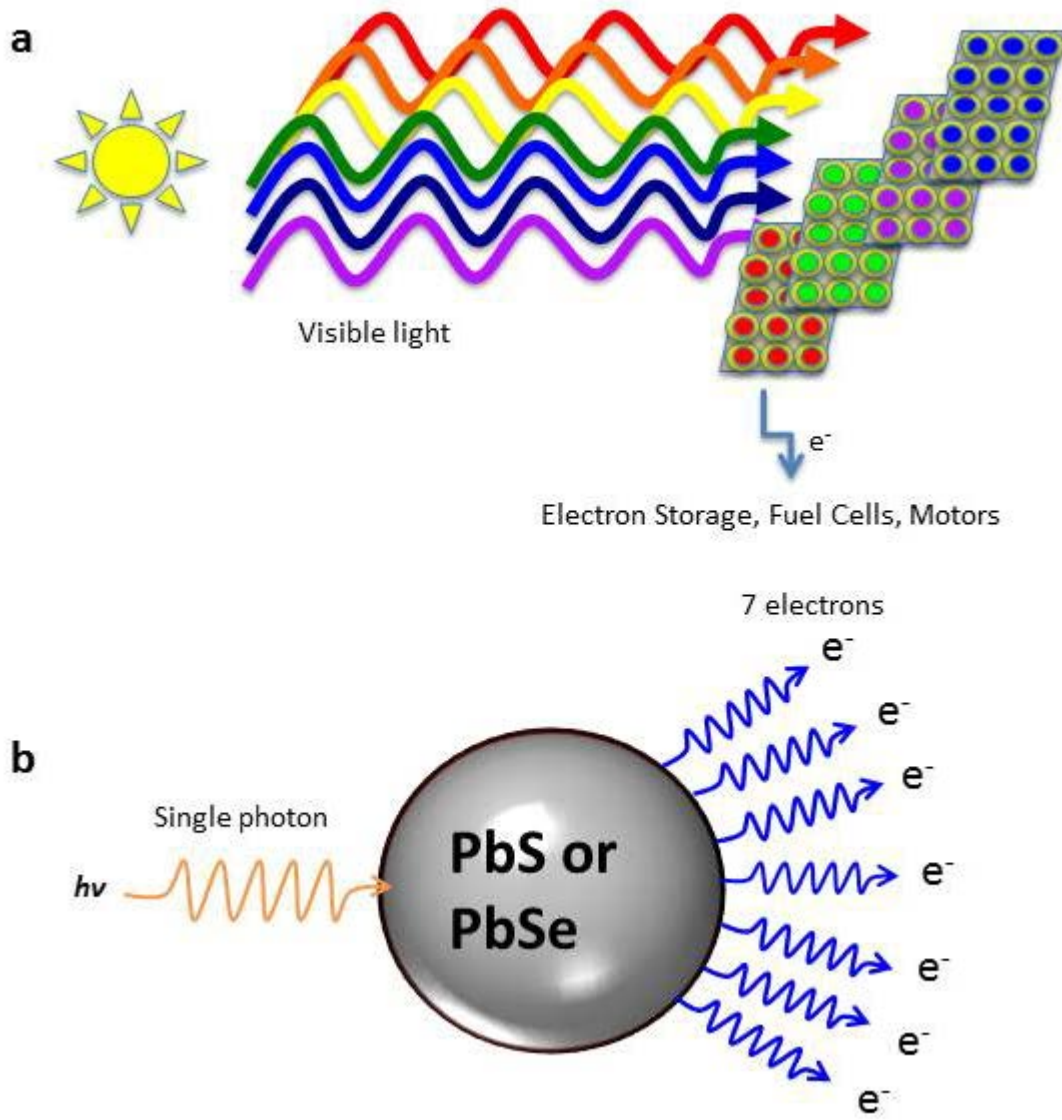


Figure 1-2. (a) Stacked solar cells. (b) Carrier multiplication (see reference 36)

protein nanocage and possesses channels that allow metal ions to enter and leave the cavity (Fig. 3)³⁸. Nucleation sites on the interior of the ferritin cavity allow for mineralization of metal oxides making it a naturally occurring organic/inorganic hybrid material. Ferritin has an exterior diameter of 12 nm and an interior diameter of 8 nm resulting in a 2 nm thick (light transparent) protein shell that separates the mineral from the exterior solution. Ferritin can accommodate up to 4500 Fe ions as a ferrihydrite mineral. It is a thermo stable protein (up to 80° C) and has good pH tolerance that ranges between pH 5-10. Ferritin naturally binds iron and in addition, non-native metals have been incorporated inside ferritin including transition metal oxides, sulfides, selenides and oxoanions (Table 1). Additionally, once these transition metals have been deposited inside ferritin it is possible to reduce them to their elemental form using strong reductants³⁹.

Metal oxides are known semiconductors and light is known to excite electronic transitions in these minerals. Ferritin has been studied for its photochemical properties as it promotes important oxidation and reduction reactions⁴⁰⁻⁴². Figure 4 represents the photochemical reactions that take place. The photochemical properties of ferritin are described in more detail in Section 1 below.

A variety of techniques can be used to organize ferritin and its encapsulated cargo can be organized into nano architectures⁴³. For example, ferritin can be organized into 2-dimensional and 3-dimensional arrays producing ordered structures of ferritin and its encapsulated cargo⁴³. (Figures of nano architectures of ferritin and the characterization of these assemblies are available in the reference of Yamashita (2010)). These nano architectures might possess unique

Table 1-1. Materials Synthesized Inside Ferritin ^a

Ferritin Mineral	Metals /Ferritin ^b	Band Gap (eV) ^c	Reference ^d
Metals			
Ag	380		39, 81, 82
Au	ND		83
Co	ND		84
Cu	350-2000		85
Ni	ND		84
Pd	~500		86
Pt	250-1000		87
CoPt	ND		88
Metal Minerals			
FeOOH	~4500	2.5-3.5	
Fe ₃ O ₄	3000	0.14	89
CoOOH	2250	1.4-1.8	63
MnOOH	3000		64
Cr hydroxide	4500	2.75	90
Ni hydroxide	8000	3.7	90
Ti(OH) ₃	ND	3	91
EuOOH	ND	ND	91
U	800	1.3	92
Iron phosphate, arsenate, vanadate, molybdate	~2000	ND	61
Lutetium phosphate	500	ND	93
Lu	ND	ND	94
Quantum Dots Minerals			
CdS	275	2.42	95
CdSe	1000	1.74	96
ZnSe	1500	2.7	97
Au ₂ S	3000	1.8	98
PbS	ND	0.37	99
FeS	3000	0.95	100

^a Table updated and modified from ¹⁰¹.

^b This value represents the range or maximal number of metals/ferritin reported in the literature.

^c Estimate of band gap based on bulk materials or nanoparticle data in literature.

^d Representative reference for this class of materials prepared in ferritin.

ND - values not determined.

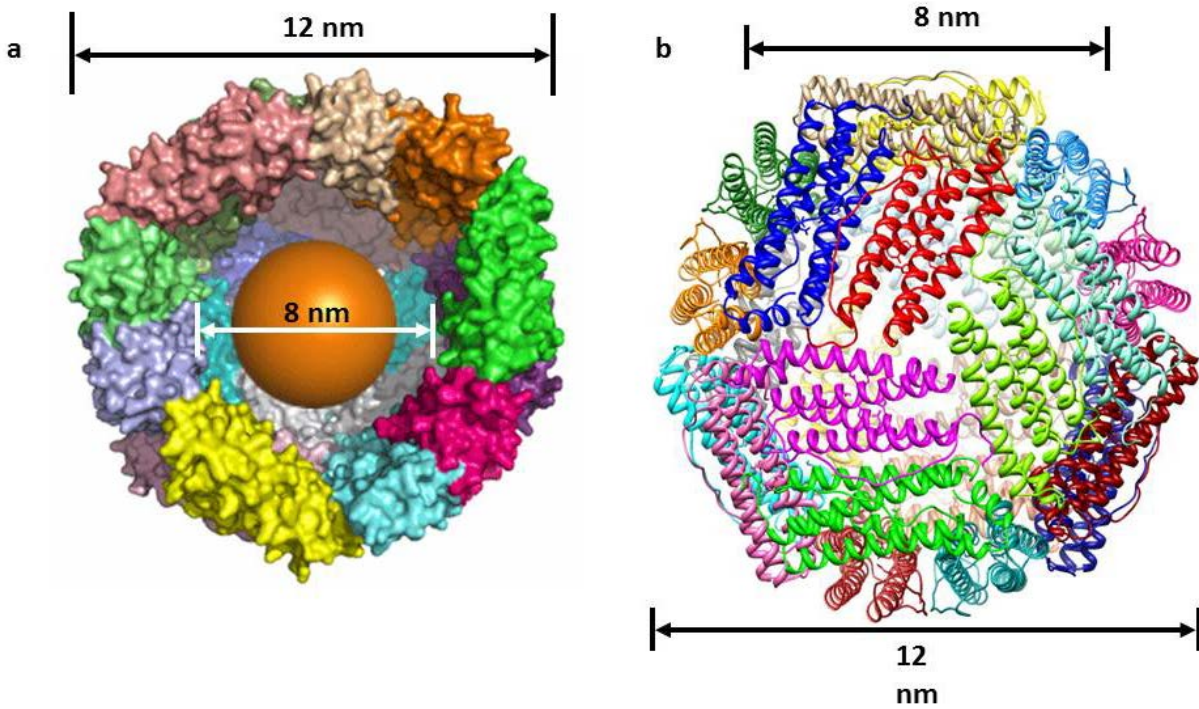


Figure 1-3. (a) Ferritin representing the 24 subunits assembled to form the hollow spherical protein with a 12 nm diameter exterior and an 8 nm diameter interior cavity with an encapsulated mineral. (b) Ribbon diagram representation of the ferritin protein crystal structure. Note that the opening at the center of the figure represents the 3-fold channel where iron enters and leaves ferritin. (Ribbon diagram prepared using the UCSF Chimera program accessing 1MFR file in the RCSB Protein Data Bank)

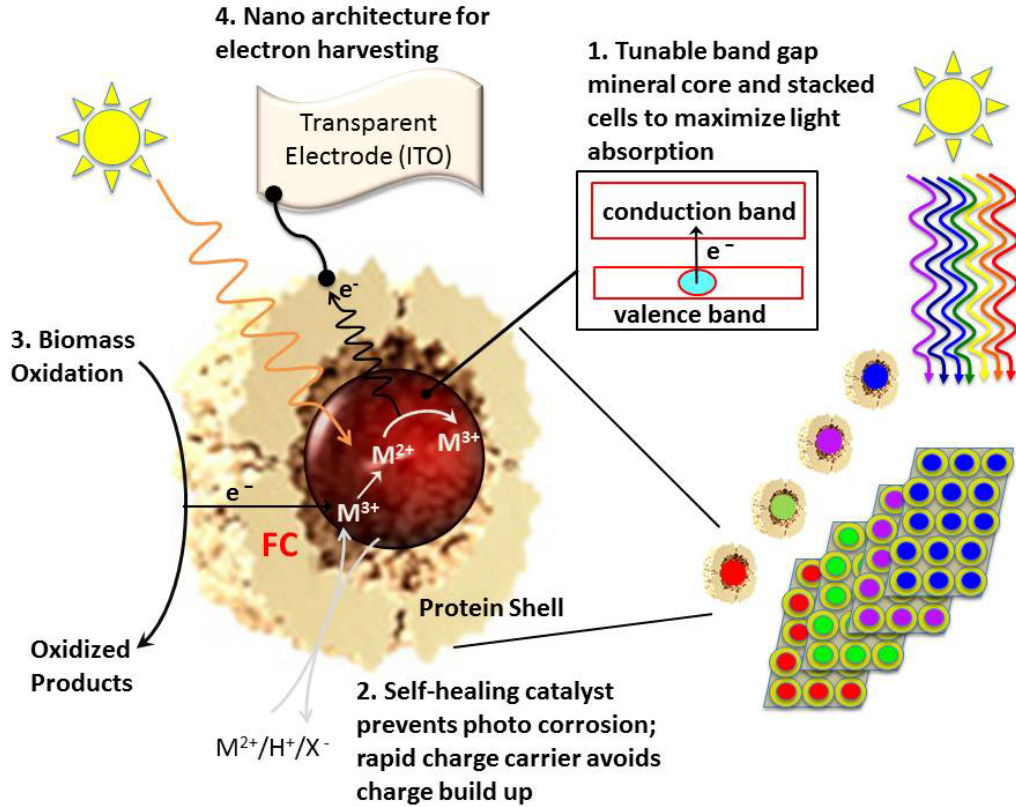


Figure 1-4. Challenges of the 3rd generation photo catalysts that ferritin can overcome:

1. Ferritin can be prepared with a variety of mineral cores with different band gaps. This allows the synthesis of tunable band gap materials in ferritin. Ferritin can also be attached and potentially layered to transparent electrodes to create stacked light harvesting arrays. 2. Self-healing catalysts are important for durability. Ferritin possesses a ferroxidase center (FC) with ferroxidase activity that prevents photo corrosion allowing the photo catalyst mineral to be re-synthesized if photo corrosion occurs. 3. Ferritin is capable of biomass oxidation. Ferritin has been used to successfully oxidize organic acids, sulfhydryl groups, alcohols, Good's buffers, amines, glucose, gluconic acid, glycerol, dihydroxyacetone and glyceraldehyde. 4. Ferritin can form nano architectures and can be functionalized for electron harvesting capabilities. These properties can limit charge recombination and direct electrons to electrodes for battery and fuel cell applications. Ferritin can donate electrons to metal ions (e.g.: Cu, Au), redox dyes (viologens) and proteins (cytochrome c).

properties for light harvesting or for oxidative charge separation reactions. Additionally the exterior of ferritin can be functionalized with chemical “handles” to allow the attachment of light absorbing molecules or to trigger assembly of nano architectures^{44, 45}. Ultimately, the recent advances in transition metal oxide water oxidation catalysts^{20, 26-33} and the ability to assemble ferritin into nano architectures might be combined to produce third generation photo catalysts capable of light harvesting and water oxidation to produce hydrogen²³. Below we expand on the four goals listed in the abstract that are required to improve photo catalysis and demonstrate that ferritin possesses or can be chemically altered to exhibit these desired properties. Figure 4 represents the properties ferritin possesses that make it a model system for achieving these goals and this figure will be referred to throughout the review.

1. The development of inexpensive, abundant, non-toxic charge separation catalysts that absorb visible light;

Iron oxides are photo catalysts that undergo charge separation reactions when illuminated⁴⁶. In addition, light can catalyze the photochemical oxidation of organic molecules complexed with iron^{47, 48}. Colloidal suspensions of iron oxide nanoparticles function as photo catalysts but their solubility is limited and their catalytic stability is short due to photo-corrosion in aqueous solutions. Photo corrosion occurs when Fe(III) is photo reduced to Fe² followed by oxidation back to Fe³⁺ which rapidly precipitates as rust. Metal oxides of other metals possess the same photochemical properties and also undergo photo corrosion^{49, 50}.

Metal oxide nanoparticles are not soluble but when metal oxides are encapsulated inside ferritin, the protein shell, which is soluble, allows the metal oxides to be dispersed in solution. Relatively high concentrations of the metal oxides can be achieved when solubilized in ferritin.

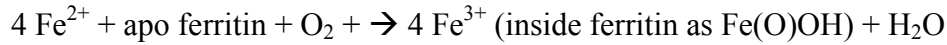
For example, a 10-mg/mL solution of ferritin containing 2000 metal ions per ferritin would have a metal concentration of 44 mM. The ability of ferritin to disperse the metal oxide minerals in solution effectively increases the probability of light interacting with these metal oxide catalysts to improve the probability of charge separation reactions.

The first photochemical studies of ferritin were demonstrated in plant ferritin,⁵¹ followed by UV light exposure studies to determine if iron in ferritin could be photo reduced and release Fe^{2+} as a catalyst for the formation of reactive oxygen species (ROS)⁵²⁻⁵⁴. Since these initial reports of ferritin photochemistry, ferritin has been shown to act as a powerful reducing agent for photo reducing redox dyes (viologens), proteins (cytochrome c) and metal ions (Cu^{2+} and Au^{3+})⁴⁰.

Nikandrov proposed and evaluated a variety of mechanisms for electron transfers from the iron oxide interior, through the ferritin protein shell, to the electron acceptors. After a series of control experiments he concluded that the reaction proceeded through a valence band (VB) to conduction band (CB) transition and electron tunneling through the protein shell^{40, 55, 56}.

The work described above used near UV light to catalyze the photochemical reactions. The ability to efficiently harvest the full solar spectrum from UV light throughout the entire visible range to the near IR is an important goal to achieve. Therefore, developing ferritin photo catalysts that absorb light at different wavelengths in the visible portion of the spectrum is an essential goal for maximizing light harvesting. Ferritin, with a ferrihydrite core, has a reported band gap in the range of 2.5 – 3.5 eV, which means that light between 350 nm to 500 nm will excite electrons from the CB to the VB^{57, 58}.

Remarkably, the iron can be removed from iron-containing ferritin (referred to as holoferritin) by reduction and chelation of the iron producing an iron-free protein shell called apo ferritin. The iron core can be reconstituted inside ferritin by the following reaction.



Divalent metal ions of most of the first row transition metals can be substituted into this reaction equation to prepare cores of Mn(O)OH, Co(O)OH, Ni(O)OH, as well as other metal hydroxide species (Table 1). Similar strategies have been used to synthesize a variety of other minerals and quantum dot materials inside ferritin. The procedures and methods for these synthetic materials can be found in references in Table 1.

The ability to synthesize ferritin with a large variety of mineral cores (Table 1) with different VB to CB transitions provides the opportunity to create “wavelength tunable” photo catalysts inside ferritin ⁵⁹. For example, replacing the ferrihydrite mineral core (2.5 – 3.5 eV, 350 – 500 nm) with CdS (2.4 eV, 516 nm), CdSe (1.8 eV, 688 nm) or GaAs (1.42 eV, 873 nm) will change the wavelength of light required to excite electrons from the VB to the CB. Altering the minerals sequestered inside ferritin will allow the tuning of the wavelength of light that is absorbed by ferritin Fig. 4. Additionally, altering the anions from oxide to phosphate, borate or sulfide provides other methods for tuning the band gaps and altering the wavelengths absorbed by the minerals ^{60, 61}. Efforts are underway in our laboratory to use these techniques to prepare ferritin minerals that absorb strongly in the visible portion of the spectrum.

Generally, one photon of light is able, at best, to produce one charge separation event. Schaller et al. reported that PbS and PbSe nanoparticles are able exhibit multiple carrier effects

where one photon was able to produce multiple excitons (Fig 2B)³⁶. In fact, their study showed that up to 7 excitations could be generated by one photon of light using PbS. Bulk materials are less likely to perform carrier multiplication effects but nanoparticles possess the ability to produce this charge carrier phenomenon. PbS has been synthesized inside ferritin but these samples have not yet been tested for charge multiplication effects. Perhaps the hybrid nature of ferritin containing PbS or other charge multiplication effect materials will further enhance solar energy harvesting.

2. Development of stable catalysts with high turnover numbers that possess self-healing mechanisms to prevent photo corrosion.

Nanoparticles of ferrihydrite ($\text{Fe}(\text{O})\text{OH}$) can catalyze photo reduction reactions, but their activity is short lived because the ferrihydrite particles undergo reductive photo corrosion^{49, 50}. Photo catalysis stops when Fe^{2+} ions are oxidized to Fe^{3+} and precipitate by hydrolysis forming an amorphous precipitate.

Ferritin can overcome photo corrosion and maintains the $\text{Fe}(\text{O})\text{OH}$ mineral in an active form. The protein shell is transparent to light and allows light to interact with the $\text{Fe}(\text{O})\text{OH}$ mineral causing charge separation to occur in the semi-conductor mineral. If Fe^{2+} forms, it migrates to an enzyme site called the ferroxidase center, where it is re-oxidized to Fe^{3+} ⁶². The ferroxidase center catalytic site is found at the center of the H-ferritin subunits so Fe^{2+} does not leave the protective confines of the ferritin protein shell. Once iron is oxidized at the ferroxidase center, the Fe^{3+} ions are reincorporated into the mineral core. Ferroxidase activity stops iron from moving into the surrounding solution and keeps the catalytic particle substantially unaltered.

For most catalysts, the surface of the catalyst is critical for activity so interactions of the protein shell with the catalyst surface might impose limitations to the reaction. In the case of ferritin, these interactions appear to be required to sustain an active catalyst because control reactions with Fe(O)OH nanoparticles show rapid photo corrosion and precipitation of iron.

Similar reactions occur with other metals artificially deposited inside ferritin suggesting that the ferroxidase enzyme active site can function as a self-healing mineralization enzyme for photochemical reactions ^{63, 64}. Ensign demonstrated that ferritin was capable of repeated photochemical reactions without changes to the rate of Cu(0) nanoparticle formation and with only a small amount of protein degradation ⁴¹. However, the long-term stability of photochemical reactions of metal oxides inside ferritin has not been extensively studied. In general, ferritin is a very stable protein and potentially ferritin from thermophilic organisms will enhance its stability in photochemical reactions ^{65, 66}.

3. Development of photo catalysts capable of oxidizing a broad range of electron donors.

One goal of this work is to mimic Nature and develop synthetic photo catalysts capable of oxidizing abundant sources of biomass such as glucose or glycerol with the future goal of developing photo catalysts capable of oxidizing water. Nikandrov et al. showed that illumination of ferritin with light below 400 nm catalyzes the photo-oxidation of organic molecules and donates the electrons to external electron acceptors. A variety of electron donors have been studied and include organic acids, sulfhydryl groups, alcohols, Good's buffers and amines ^{40, 58, 67}, and additionally we have observed the oxidation of glucose, gluconic acid, glycerol, dihydroxyacetone and glyceraldehyde (unpublished data). Although the mechanism of oxidation

of these electron donors is not yet established, it is possible that the ferroxidase center of ferritin may be involved in the oxidation of these molecules as reported by Zhang et al. for 3-(N-morpholino)propanesulfonic acid (MOPS) buffer⁶⁸.

4. Developing Hybrid organic/inorganic nano architectures that bridge charge flow from electron donors, through the catalyst to electron acceptors.

A variety of electron acceptors have been used in the ferritin photochemical system and include Cr(VI), Cu(II), Au(III), viologens and cytochrome c^{40-42, 57}. The redox potential of the electron acceptors characterized to date include acceptors with positive potentials such as Au³⁺ (+ 1.18 V) and negative potentials such as viologens (-0.360 V). To harvest energy, the excited electrons must be accepted by molecules that will transfer the electrons to electrodes for fuel cell applications or for storage in batteries. Alternatively, the electrons can be used to produce energy rich molecules that can be used as fuels. For example the reduction of viologen species is promising because viologens are excellent mediators for donating electrons to electrodes in electrochemical cells. Additionally, methyl viologen has been used to successfully reduce protons to hydrogen, which is a fuel that can be stored⁶⁹. The fact that gold and copper nanoparticles are synthesized within ferritin (copper) or on the exterior surface of ferritin (gold) may allow these metals to be “built in” in situ electrodes for electrochemical applications^{41, 42}.

Additionally, ferritin is known to naturally bind directly to gold and indium tin oxide electrode surfaces or can be chemically modified for covalent attachment to electrodes⁷⁰⁻⁷⁵. Attaching ferritin to a light transparent indium tin oxide electrode (ITO) is particularly useful for photochemical applications⁷⁶. Ferritin possesses inherent redox properties in the protein shell that allows efficient electron transfer from the iron core, through the protein, directly to the

electrode. Additionally, ferritin isolated from bacteria contains up to 12 heme groups that function to mediate electron transfer across the protein shell ^{44, 77}. If electron transfer becomes limiting in reactions with mammalian ferritin, a switch to bacterial ferritin may further enhance electron transfer to electrodes. The direct linkage of ferritin to electrodes will couple photochemical oxidation of biomass molecules directly into battery or fuel cell systems.

There are two critical issues associated with the electrons as they move through photochemical systems that limit the efficiency of the reactions. The first issue is charge recombination where excited electrons fall back to the original state ⁷⁸. The second limitation is charge build-up that occurs when local concentrations of charge inhibit the reactions from proceeding.

The hybrid organic/inorganic nature of ferritin prevents charge recombination by stabilizing the excited electronic state. Nikandrov demonstrated that light caused the excitation of an electron into the conduction band of the iron oxide cluster of ferritin and the excited electron was relatively stable (microsecond time scale) because: 1) the hole created in the valence band is rapidly filled by oxidation of the sacrificial electron donors; 2) the ferritin iron core is capable of delocalizing the electron throughout the core to enhance stability; and 3) both the iron core and the protein shell are redox active and can “store” the electron(s) until an electron acceptor is encountered in solution ^{40, 56}.

Photosynthesis prevents charge build-up reactions by proton-coupled electron transport ¹⁴. Electron and proton transport pathways have evolved in trans membrane protein complexes that allow rapid equilibration of charge to prevent charge build up that is inhibitory to the next charge separation event. Artificial systems are limited by charge build up and this slows the reactions and limits the energy produced by the charge separation ⁷⁸.

Remarkably ferritin has evolved mechanisms to alleviate charge build up. As iron enters or leaves ferritin, the oxidation state of the iron changes between Fe^{2+} and Fe^{3+} . These redox reactions involve electron transfer across the protein shell for iron oxidation or reduction and require efficient proton-coupled electron transfer to allow positive charge to accompany the negative charge of the electron. The ferritin protein shell is redox active and mediates these redox reactions⁵⁶. These properties allow ferritin to act as a “membrane” that mediates charge transfer reactions and controls ion gradients similar to the cellular membranes that allow photosynthetic reactions in plants^{55, 56, 79}. Additionally, ferritin possesses other ion transport mechanisms where anions are selectively and rapidly transported into and out of ferritin to balance charge (Fig 4)⁸⁰.

The ferritin protein contains a large number of amino acid R groups or functional groups that provide handles for adding a variety of chemical functional groups and assembling architectures (Fig 4)^{44, 45}. Without any modifications ferritin can be deposited in monolayers and in multi-layers on a variety of surfaces in very ordered arrays⁴³. These assemblies may further enhance light harvesting, enhance charge separation reactions and mediate the flow of charge carriers to increase efficiency of solar energy harvesting. Additionally, light-harvesting molecules may be attached to the exterior of ferritin to further enhance light absorption and increase solar energy harvesting (Fig 4)⁴⁴.

Future Directions

The recent progress developing water oxidation catalysts from earth abundant transition metals such as cobalt, manganese and iron provides feasible materials for the development of hydrogen production by oxidizing water^{20, 26-33}. Incorporating these water-oxidizing catalysts

into hybrid inorganic/organic light harvesting nano architectures with enhanced charge separation and electron transfer pathways will further improve the usefulness of these catalysts. Additionally, tuning the band gap of these light-harvesting architectures to absorb solar radiation in the visible spectrum will increase the energy harvested. Figure 5 shows proposed goals for light harvesting applications using the ferritin photochemical system. We propose that mineralizing the right blend of metals and anions inside ferritin will allow us to create light harvesting semiconductors or quantum dots. The ferritin protein shell also provides handles for chemical functionalization where other light harvesting molecules can be attached to ferritin or permits ferritin to be assembled into arrays or attached to electrodes. These advantages of ferritin will provide a strong model system for studying the ability of hybrid inorganic/organic nano architectures to function in solar energy harvesting.

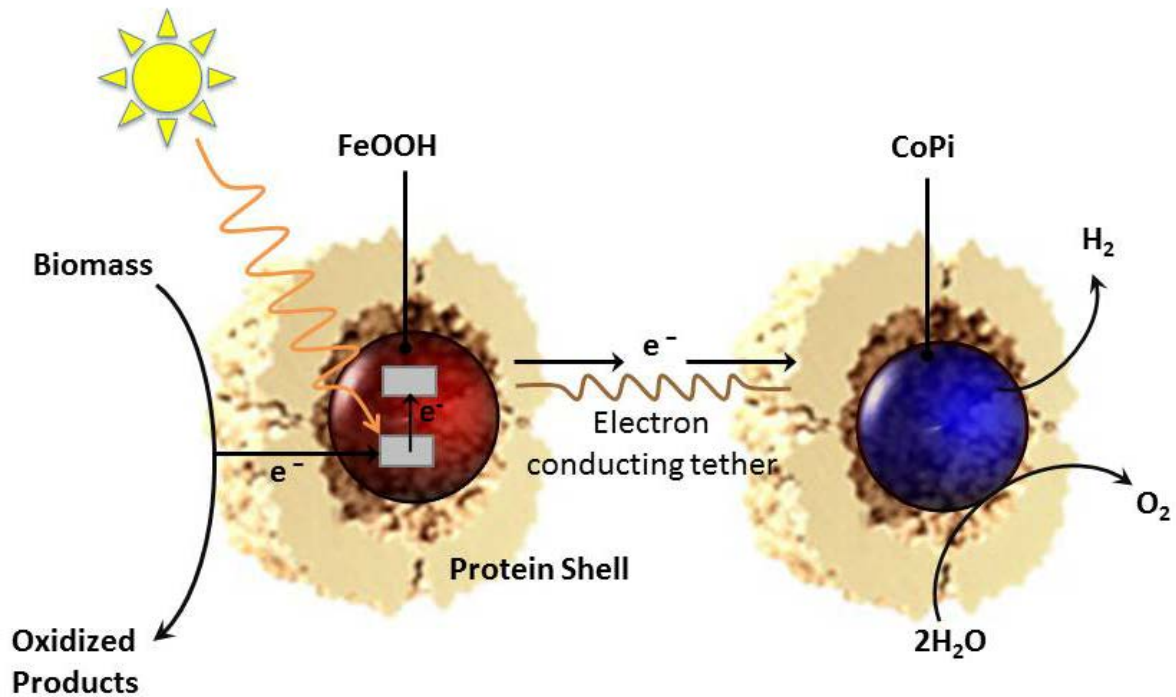


Figure 1-5. Ferritin nano architecture for light harvesting and water oxidation. Our ultimate goal is to combine the light harvesting properties of ferritin with the water oxidizing or hydrogen evolving properties of the metal oxide catalysts. This figure represents a model where such a goal could be realized.

References

1. G. Zhang, S. Finefrock, D. Liang, G. G. Yadav, H. Yang, H. Fang and Y. Wu, *Nanoscale*, 2011, 3, 2430-2443.
2. V. V. Tyagi, N. A. A. Rahim, N. A. Rahim and J. A. L. Selvaraj, *Renewable & Sustainable Energy Reviews*, 2013, 20, 443-461.
3. A. Goetzberger, J. Luther and G. Willeke, *Solar Energy Materials and Solar Cells*, 2002, 74, 1-11.
4. L. M. Peter, *Philosophical Transactions of the Royal Society a-Mathematical Physical and Engineering Sciences*, 2011, 369, 1840-1856.
5. B. Sinha, *Current Science*, 2011, 100, 654-660.
6. W. Shockley and H. J. Queisser, *Journal of Applied Physics*, 1961, 32, 510-519.
7. J. Schmidtke, *Opt. Express*, 2010, 18, A477-A486.
8. F. Sauvage, S. Chhor, A. Marchioro, J. E. Moser and M. Graetzel, *Journal of the American Chemical Society*, 2011, 133, 13103-13109.
9. F. Sauvage, D. H. Chen, P. Comte, F. Z. Huang, L. P. Heiniger, Y. B. Cheng, R. A. Caruso and M. Graetzel, *Acs Nano*, 2010, 4, 4420-4425.
10. N. Yeh and P. Yeh, *Renewable & Sustainable Energy Reviews*, 2013, 21, 421-431.
11. I. J. Kramer and E. H. Sargent, *Acs Nano*, 2011, 5, 8506-8514.
12. A. L. Rogach, *Nano Today*, 2011, 6, 355-365.
13. R. E. Blankenship, D. M. Tiede, J. Barber, G. W. Brudvig, G. Fleming, M. Ghirardi, M. R. Gunner, W. Junge, D. M. Kramer, A. Melis, T. A. Moore, C. C. Moser, D. G. Nocera, A. J. Nozik, D. R. Ort, W. W. Parson, R. C. Prince and R. T. Sayre, *Science*, 2011, 332, 805-809.
14. I. McConnell, G. Li and G. W. Brudvig, *Chem Biol*, 2010, 17, 434-447.

15. R. W. Bradley, P. Bombelli, S. J. L. Rowden and C. J. Howe, *Biochemical Society Transactions*, 2012, 40, 1302-1307.
16. K. Woronowicz, S. Ahmed, A. A. Biradar, A. V. Biradar, D. P. Birnie, 3rd, T. Asefa and R. A. Niederman, *Photochemistry and Photobiology*, 2012, 88, 1467-1472.
17. T. Yagishita, S. Sawayama, K. I. Tsukahara and T. Ogi, *Solar Energy*, 1997, 61, 347-353.
18. T. Yagishita, S. Sawayama, K. I. Tsukahara and T. Ogi, *Journal of Fermentation and Bioengineering*, 1998, 85, 546-549.
19. M. Hambourger, G. Kodis, M. D. Vaughn, G. F. Moore, D. Gust, A. L. Moore and T. A. Moore, *Dalton Trans*, 2009, 9979-9989.
20. M. W. Kanan, Y. Surendranath and D. G. Nocera, *Chem Soc Rev*, 2009, 38, 109-114.
21. S. W. Gersten, G. J. Samuels and T. J. Meyer, *Journal of the American Chemical Society*, 1982, 104, 4029-4030.
22. R. Brimblecombe, G. C. Dismukes, G. F. Swiegers and L. Spiccia, *Dalton Transactions*, 2009, 9374-9384.
23. V. Artero and M. Fontecave, *Comptes Rendus Chimie*, 2011, 14, 799-810.
24. E. S. Andreiadis, M. Chavarot-Kerlidou, M. Fontecave and V. Artero, *Photochemistry and Photobiology*, 2011, 87, 946-964.
25. F. Puntoriero, A. Sartorel, M. Orlandi, G. La Ganga, S. Serroni, M. Bonchio, F. Scandola and S. Campagna, *Coordination Chemistry Reviews*, 2011, 255, 2594-2601.
26. Y. Surendranath, M. Dinca and D. G. Nocera, *J Am Chem Soc*, 2009, 131, 2615-2620.
27. M. W. Kanan, J. Yano, Y. Surendranath, M. Dinca, V. K. Yachandra and D. G. Nocera, *J Am Chem Soc*, 2010, 132, 13692-13701.

28. D. A. Lutterman, Y. Surendranath and D. G. Nocera, *J Am Chem Soc*, 2009, 131, 3838-3839.
29. J. G. McAlpin, Y. Surendranath, M. Dinca, T. A. Stich, S. A. Stoian, W. H. Casey, D. G. Nocera and R. D. Britt, *J Am Chem Soc*, 2010, 132, 6882-6883.
30. J. J. Pijpers, M. T. Winkler, Y. Surendranath, T. Buonassisi and D. G. Nocera, *Proc Natl Acad Sci U S A*, 2011, 108, 10056-10061.
31. V. Artero, M. Chavarot-Kerlidou and M. Fontecave, *Angewandte Chemie-International Edition*, 2011, 50, 7238-7266.
32. M. Dinca, Y. Surendranath and D. G. Nocera, *Proc Natl Acad Sci U S A*, 2010, 107, 10337-10341.
33. Y. Surendranath, M. W. Kanan and D. G. Nocera, *J Am Chem Soc*, 2010, 132, 16501-16509.
34. W. Guter, J. Schone, S. P. Philipps, M. Steiner, G. Siefer, A. Wekkeli, E. Welser, E. Oliva, A. W. Bett and F. Dimroth, *Applied Physics Letters*, 2009, 94, 223504-223503.
35. G. Konstantatos and E. H. Sargent, *Nat Nanotechnol*, 2010, 5, 391-400.
36. R. D. Schaller, M. Sykora, J. M. Pietryga and V. I. Klimov, *Nano Lett*, 2006, 6, 424-429.
37. P. W. M. Blom, V. D. Mihailetschi, L. J. A. Koster and D. E. Markov, *Advanced Materials*, 2007, 19, 1551-1566.
38. R. R. Crichton and J.-P. Declercq, *Biochimica et Biophysica Acta (BBA) - General Subjects*, 2010, 1800, 706-718.
39. C. A. Butts, J. Swift, S. G. Kang, L. Di Costanzo, D. W. Christianson, J. G. Saven and I. J. Dmochowski, *Biochemistry*, 2008, 47, 12729-12739.

40. V. V. Nikandrov, C. K. Gratzel, J. E. Moser and M. Gratzel, *J Photochem Photobiol B*, 1997, 41, 83-89.
41. D. Ensign, M. Young and T. Douglas, *Inorg. Chem.*, 2004, 43, 3441-3446.
42. J. D. Keyes, R. J. Hilton, J. Farrer and R. K. Watt, *J. Nanopart. Res.*, 2011, 13, 2563-2575.
43. I. Yamashita, K. Iwahori and S. Kumagai, *Biochimica et Biophysica Acta (BBA) - General Subjects*, 2010, 1800, 846-857.
44. B. Fernandez, N. Galvez, P. Sanchez, R. Cuesta, R. Bermejo and J. M. Dominguez-Vera, *J Biol Inorg Chem*, 2008, 13, 349-355.
45. M. Sengonul, A. Sousa and M. Libera, *Colloids and Surfaces B: Biointerfaces*, 2009, 73, 152-155.
46. J. K. Leland and A. J. Bard, *Journal of Physical Chemistry*, 1987, 91, 5076-5083.
47. J. H. Carey and C. H. Langford, *Canadian Journal of Chemistry-Revue Canadienne De Chimie*, 1975, 53, 2436-2440.
48. H. B. Abrahamson, A. B. Rezvani and J. G. Brushmiller, *Inorganica Chimica Acta*, 1994, 226, 117-127.
49. S. M. Gupta and M. Tripathi, *High Energy Chem.*, 2012, 46, 1-9.
50. A. L. Stroyuk, V. V. Shvalagin, A. E. Raevskaya, A. I. Kryukov and S. Y. Kuchmii, *Theor. Exp. Chem.*, 2008, 44, 205-231.
51. J. P. Laulhere, A. M. Laboure and J. F. Briat, *Biochem J*, 1990, 269, 79-84.
52. M. Aubailly, R. Santus and S. Salmon, *Photochem Photobiol*, 1991, 54, 769-773.
53. M. Aubailly, S. Salmon, J. Haigle, J. C. Bazin, J. C. Maziere and R. Santus, *J Photochem Photobiol B*, 1994, 26, 185-191.

54. P. Morliere, S. Salmon, M. Aubailly, A. Risler and R. Santus, *Biochim Biophys Acta*, 1997, 1334, 283-290.
55. G. D. Watt, D. Jacobs and R. B. Frankel, *Proc Natl Acad Sci U S A*, 1988, 85, 7457-7461.
56. R. K. Watt, R. B. Frankel and G. D. Watt, *Biochemistry*, 1992, 31, 9673-9679.
57. I. Kim, H. A. Hosein, D. R. Strongin and T. Douglas, *Chem. Mater.*, 2002, 14, 4874-4879.
58. R. J. Hilton, J. D. Keyes and R. K. Watt, SPIE Smart Structures/NDE 2010, San Diego, CA, 2010.
59. T. Rakshit and R. Mukhopadhyay, *Langmuir*, 2011, 27, 9681-9686.
60. G. Liu, H. Wu, J. Wang and Y. Lin, *Small*, 2006, 2, 1139-1143.
61. J. Polanams, A. D. Ray and R. K. Watt, *Inorganic Chemistry*, 2005, 44, 3203-3209.
62. F. Bou-Abdallah, *Biochimica et Biophysica Acta (BBA) - General Subjects*, 2010, 1800, 719-731.
63. T. Douglas and V. T. Stark, *Inorg. Chem.*, 2000, 39, 1828-1830.
64. F. C. Meldrum, T. Douglas, S. Levi, P. Arosio and S. Mann, *J Inorg Biochem*, 1995, 58, 59-68.
65. A. E. Yevenes, V. Marquez and R. K. Watt, *Biochimie*, 2011, 93, 352-360.
66. J. Tatur, W. R. Hagen and P. M. Matias, *JBIC Journal of Biological Inorganic Chemistry*, 2007, 12, 615-630.
67. R. J. Hilton, J. D. Keyes and R. K. Watt, SPIE Smart Structures/NDE 2010, San Diego, CA, 2010.
68. B. Zhang, P. E. Wilson and G. D. Watt, *Journal Of Biological Inorganic Chemistry: JBIC: A Publication Of The Society Of Biological Inorganic Chemistry*, 2006, 11, 1075-1086.

69. J. Kiwi and M. Gratzel, *Angewandte Chemie-International Edition in English*, 1979, 18, 624-626.
70. J. W. Choi, Y. J. Kim, S. U. Kim, J. Min and B. K. Oh, *Ultramicroscopy*, 2008, 108, 1356-1359.
71. K. Won, M. J. Park, H. H. Yoon and J. H. Kim, *Ultramicroscopy*, 2008, 108, 1342-1347.
72. T. D. Martin, S. A. Monheit, R. J. Niichel, S. C. Peterson, C. H. Campbell and D. C. Zapien, *Journal of Electroanalytical Chemistry*, 1997, 420, 279-290.
73. R. J. Cherry, A. J. Bjornsen and D. C. Zapien, *Langmuir*, 1998, 14, 1971-1973.
74. M. S. Pyon, R. J. Cherry, A. J. Bjornsen and D. C. Zapien, *Langmuir*, 1999, 15, 7040-7046.
75. F. Caruso, D. N. Furlong and P. Kingshott, *Journal of Colloid and Interface Science*, 1997, 186, 129-140.
76. D. S. Hecht, L. B. Hu and G. Irvin, *Advanced Materials*, 2011, 23, 1482-1513.
77. N. E. Le Brun, A. Crow, M. E. P. Murphy, A. G. Mauk and G. R. Moore, *Biochimica et Biophysica Acta (BBA) - General Subjects*, 2010, 1800, 732-744.
78. W. J. Youngblood, S. H. Lee, K. Maeda and T. E. Mallouk, *Acc Chem Res*, 2009, 42, 1966-1973.
79. R. K. Watt, R. J. Hilton and D. M. Graff, *Biochimica et Biophysica Acta (BBA) - General Subjects*, 2010, 1800, 745-759.
80. R. J. Hilton, B. Zhang, L. N. Martineau, G. D. Watt and R. K. Watt, *Journal of Inorganic Biochemistry*, 2012, 108, 8-14.
81. O. Kasyutich, A. Ilari, A. Fiorillo, D. Tatchev, A. Hoell and P. Ceci, *J Am Chem Soc*, 2010, 132, 3621-3627.

82. R. M. Kramer, C. Li, D. C. Carter, M. O. Stone and R. R. Naik, *J Am Chem Soc*, 2004, 126, 13282-13286.
83. R. L. Fan, S. W. Chew, V. V. Cheong and B. P. Orner, *Small*, 2010, 6, 1483-1487.
84. N. Galvez, P. Sanchez, J. M. Dominguez-Vera, A. Soriano-Portillo, M. Clemente-Leon and E. Coronado, *Journal of Materials Chemistry*, 2006, 16, 2757-2761.
85. N. Galvez, P. Sanchez and J. M. Dominguez-Vera, *Dalton Trans*, 2005, 7, 2492-2494.
86. T. Ueno, M. Suzuki, T. Goto, T. Matsumoto, K. Nagayama and Y. Watanabe, *Angewandte Chemie International Edition*, 2004, 43, 2527-2530.
87. Q. Y. Deng, B. Yang, J. F. Wang, C. G. Whiteley and X. N. Wang, *Biotechnol Lett*, 2009, 31, 1505-1509.
88. B. Warne, O. I. Kasyutich, E. L. Mayes, J. A. L. Wiggins and K. K. W. Wong, *Ieee Transactions on Magnetics*, 2000, 36, 3009-3011.
89. F. C. Meldrum, B. R. Heywood and S. Mann, *Science*, 1992, 257, 522-523.
90. M. Okuda, K. Iwahori, I. Yamashita and H. Yoshimura, *Biotechnology and Bioengineering*, 2003, 84, 187-194.
91. M. T. Klem, J. Mosolf, M. Young and T. Douglas, *Inorg. Chem.*, 2008, 47, 2237-2239.
92. J. F. Hainfeld, *Proceedings of the National Academy of Sciences of the United States of America*, 1992, 89, 11064-11068.
93. H. Wu, M. H. Engelhard, J. Wang, D. R. Fisher and Y. H. Lin, *Journal of Materials Chemistry*, 2008, 18, 1779-1783.
94. K. Dardenne, T. Schafer, P. Lindqvist-Reis, M. A. Denecke, M. Plaschke, J. Rothe and J. I. Kim, *Environ Sci Technol*, 2002, 36, 5092-5099.
95. K. K. W. Wong and S. Mann, *Advanced Materials*, 1996, 8, 928-932.

96. I. Yamashita, J. Hayashi and M. Hara, *Chemistry Letters*, 2004, 33, 1158-1159.
97. K. Iwahori, K. Yoshizawa, M. Muraoka and I. Yamashita, *Inorganic Chemistry*, 2005, 44, 6393-6400.
98. K. Yoshizawa, K. Iwahori, K. Sugimoto and I. Yamashita, *Chemistry Letters*, 2006, 35, 1192-1193.
99. B. Hennequin, L. Turyanska, T. Ben, A. M. Beltrán, S. I. Molina, M. Li, S. Mann, A. Patané and N. R. Thomas, *Advanced Materials*, 2008, 20, 3592-3596.
100. T. Douglas, D. P. E. Dickson, S. Betteridge, J. Charnock, C. D. Garner and S. Mann, *Science*, 1995, 269, 54-57.
101. L. Zhang, J. Swift, C. A. Butts, V. Yerubandi and I. J. Dmochowski, *J Inorg Biochem*, 2007, 101, 1719-1729.

CHAPTER 2: MECHANISTIC STUDY OF FERRITIN PHOTOCHEMISTRY

Introduction

Ferritin (Ftn) is known to behave as a photo catalyst. In chapter 1 we reviewed that Nikandrov was the first to report that ferritin acted as a photocatalyst in the reduction of propyl viologen and cytochrome c.¹ The Douglas group reported the photo reduction of Cr(VI) to Cr(III) and of Cu(II) to Cu(0) nanoparticles.^{2 3} Keyes reported that ferritin could photo reduce Au(III) to Au(0) NPs.^{4 5} Each of these reactions is based on the principle that ferritin contains a semi-conductor iron mineral that possesses a band gap. Electrons can be promoted to the conduction band by light producing a hole in the valence band that can oxidize sacrificial electron donors in solution (Scheme 1 and Figure 1).⁶

Ferritin is a unique molecule: it is a robust, hybrid organic/inorganic protein, organized into a hollow, spherical nanostructure, and is capable of encapsulate a variety of minerals. These characteristics confer to ferritin the following properties: stability in a broad range of pH, salinity, and temperatures; solubility of the protein and its cargo in aqueous solutions; control of its band gap; organization in arrays on various surfaces, including electrodes; resistance to photo-corrosion; prevention of charge build up during electron transfer; and oxidization of biomass (Fig. 1-4). Scheme 1 and Scheme 2 are two representations of what would be required to design an artificial photosynthesis system. The charge separation capabilities of ferritin, along with the other properties listed above are applied in this dissertation to design a test of the light harvesting or charge separation properties (see Chapter 1), the photo-oxidation properties, and electron donor capabilities (Chapters 3-7) of a ferritin-based artificial photosynthesis system.

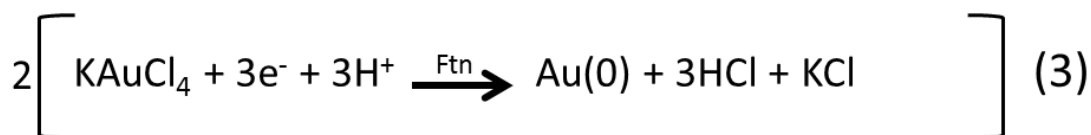
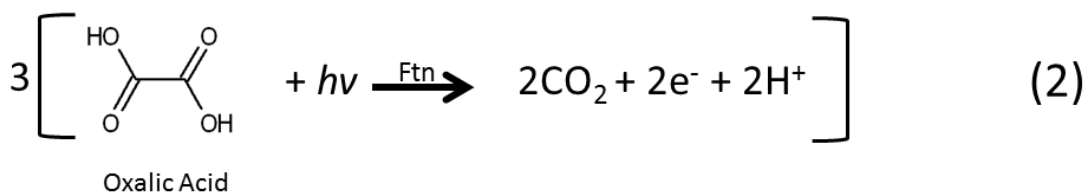
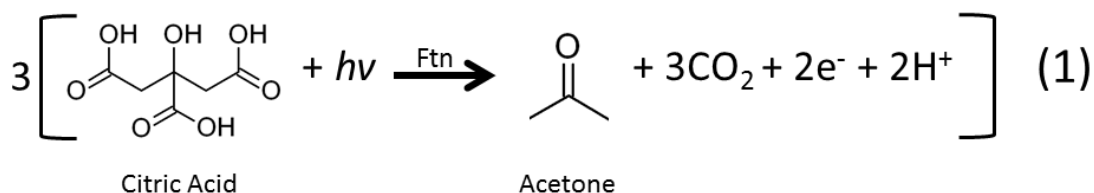
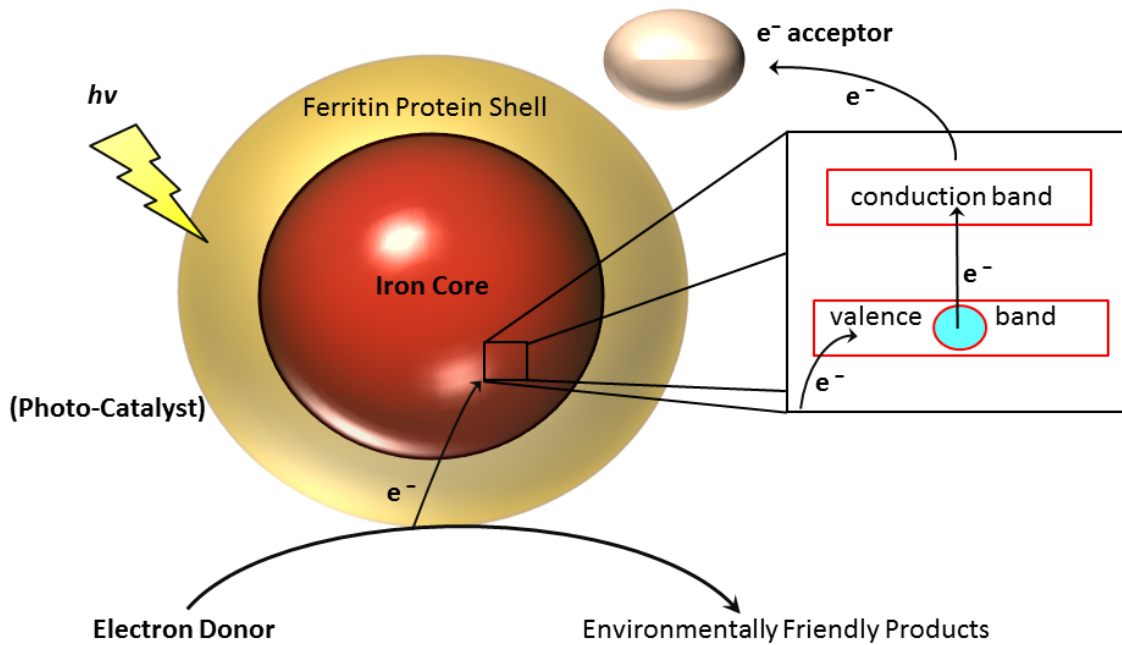
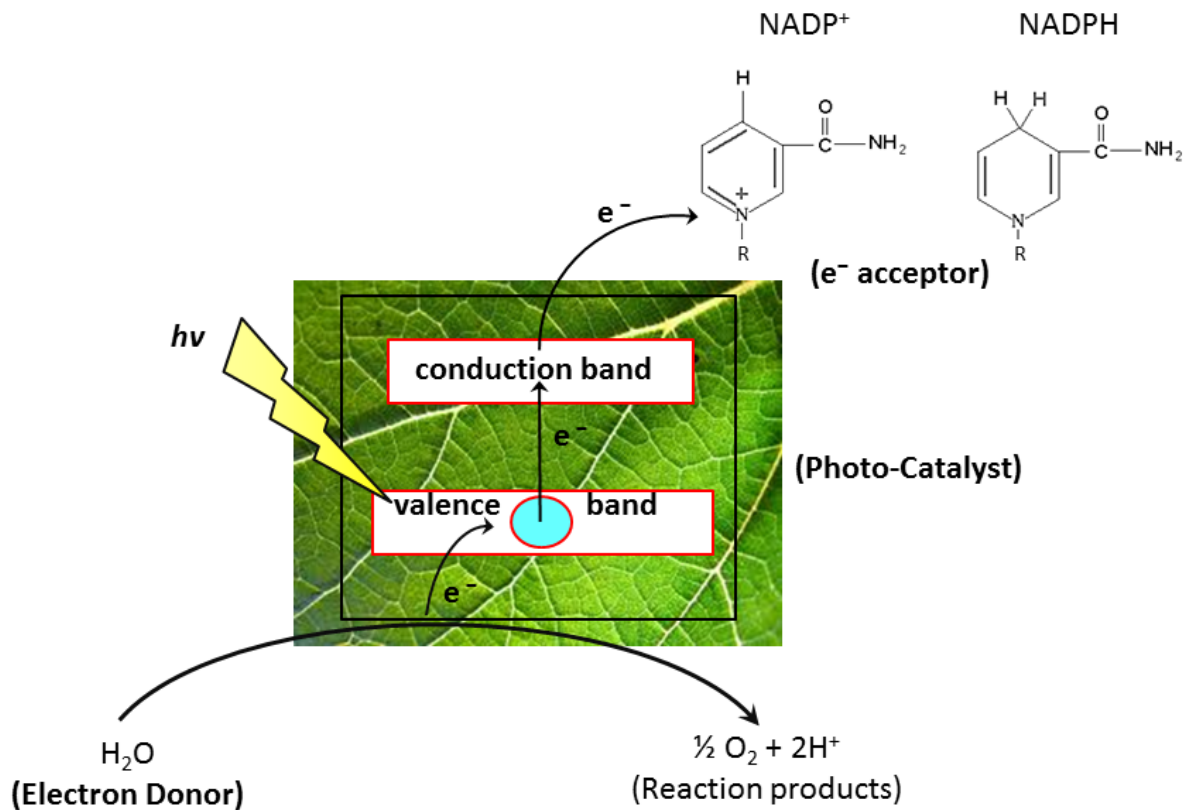


Figure 2-1. Proposed photo chemical redox reactions. Citric acid (1) and oxalic acid (2) are two electron donors utilized in the photo catalytic experiments. The electrons and the protons released by the decomposition of either electron donor reduces the Au(III) to AuNPs and lowers the pH of the medium (3).



Scheme 2-1. Ferritin electron transfer pathway. Photons hitting the ferritin semi-conductor ferrihydrite core excite electrons from the valence band to the conduction band; these excited electrons can then be captured by an electron acceptor. The hole left in the valence band is filled by the oxidation of a sacrificial electron donor.



Scheme 2-2. Photosynthetic electron transfer pathway. Chlorophyll (photo-catalyst) harvest light energy and transfer the energy to a special pair of chlorophyll capable of charge separation reactions. This reaction oxidizes a manganese cluster that extracts electrons from water (electron donor). The acceptor side of the charge separation reaction siphons the electrons away to prevent charge recombination reactions. Ultimately, electrons are transferred to NADP^+ (electron acceptor).

In order to achieve artificial photosynthesis, one should try to understand the mechanism that lies behind the photochemical electron transport system of ferritin. Photosynthesis can be split into three basic components: a source of electrons (electron donor), a charge separation photo catalyst, and an electron donor (marked in bold in Scheme 2). By comparing Schemes 1 and 2 one can notice that the mechanisms of ferritin electron transfer and photosynthesis are quite similar.

As a first step we identified an electron donor (citrate) and an electron acceptor (Au(III)): citrate had been previously used as a source of electrons in gold nanoparticle (AuNP) formation; ^{1 7} Au(III) has a favorable reduction potential (+1.1 V) and could produce gold nanoparticles (AuNPs), which have numerous applications. Previous results from our laboratory demonstrated the reduction of Au(III) to AuNPs by ferritin photo catalysis. ^{5 8 4}

In Chapter 3 we achieved the synthesis of size-controlled AuNPs by ferritin photo catalysis by modifying the concentrations of the three main components of the reaction (ferritin, citrate and Au(III)) or the redox state of the electron acceptor (Au(III) vs. Au(I)).

The kinetic plots monitored by spectrophotometry during AuNPs growth show that changing the reaction conditions affects the lag phase and the slope of the curve (see Figures in Chapter 3). Jennings *et al.* state that AuNPs produce a surface plasmon resonance (SPR) signal at 520-530 nm only after reaching a 2 nm size. ⁹ Therefore, the lag phase represents the time it takes for the AuNPs to grow up to 2 nm. The slope correlates with the AuNP growth speed once the AuNP starts producing an SPR signal. Ensign *et al.* suggest that the lag phase is due to a slow nucleation phase followed by a quick growth phase. ³ Therefore, the reaction conditions must affect both the nucleation event and the efficiency of electron transfer. Other tests showed that buffers, temperature, and salts all affected the characteristics of the AuNPs produced. ^{5 4 8}

The type of electron donor, the pH, and the redox state of the acceptor also modify the dynamics of the reaction (Fig. 2, Fig. 3, and Fig. 3-9).

We hypothesize that the conditions mentioned above may affect electron transfer and NP formation by altering one or multiple of the following phenomena: band gap, semiconductor redox potential, or mineral core K_{sp} . Furthermore, we also hypothesize that the lag phase may not be completely due to the lack of SPR band up to the critical 2 nm size, or to a slow nucleation event (suggested by Ensign but not explained mechanistically), but by other factors that will be described in the next sections.

Discussion

Core Size –Coordination Numbers

Ensign *et al.* suggested that smaller cores might react (transfer electrons) faster than larger cores. Results from our experiments confirm this hypothesis and show that smaller cores reduce the lag phase and increase the slope of the kinetic formation of AuNPs (Fig. 3-8). Additionally, the presence of a phosphate layer on the surface of the FeOOH core recapitulates, to a lesser degree, the behavior of the smaller cores (Fig. 3-8).

To evaluate the effect of core size we prepared and tested samples of (100 Fe/Ftn, 600 Fe/Ftn, 1800 Fe/Ftn) while keeping the concentration of the ferritin protein, and therefore number of cores, constant. In samples containing larger cores both the mass and the total surface area of the cores are higher than those containing the smaller cores. The higher reactivity of the smaller cores can instead be explained by a more loose crystal structure that renders the Fe atoms more readily available for chemical reactions or by the availability of surface atoms with low coordination numbers.^{10, 11}

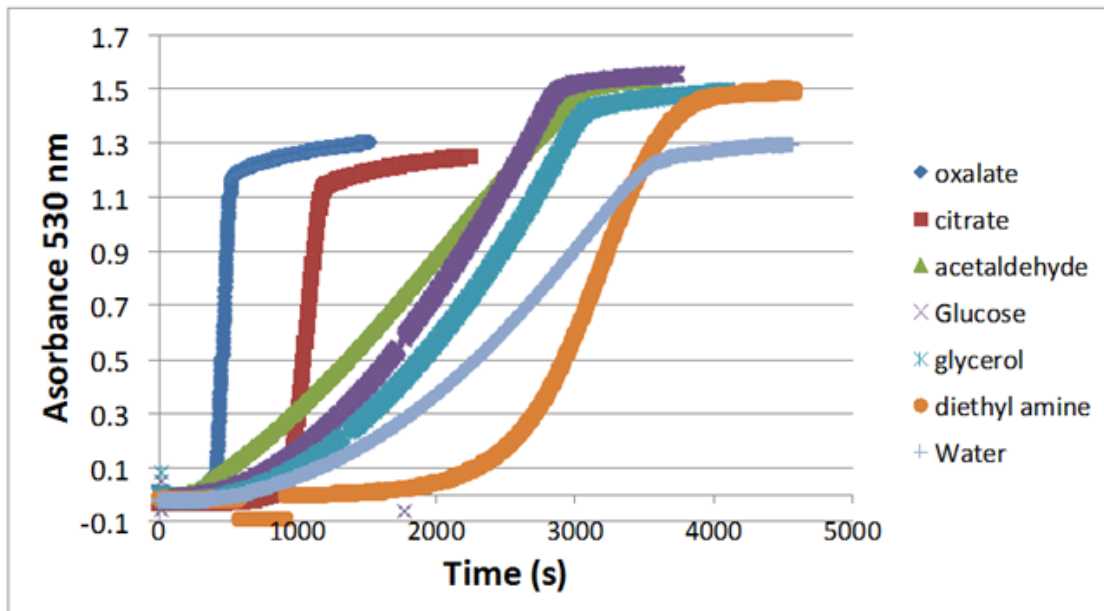


Figure 2-2. Kinetic plots of AuNPs formation using different electron donors. Each electron donor affects the electron transfer, as shown by the variable lag phases and slopes. (Graph produced by Robert Hilton).

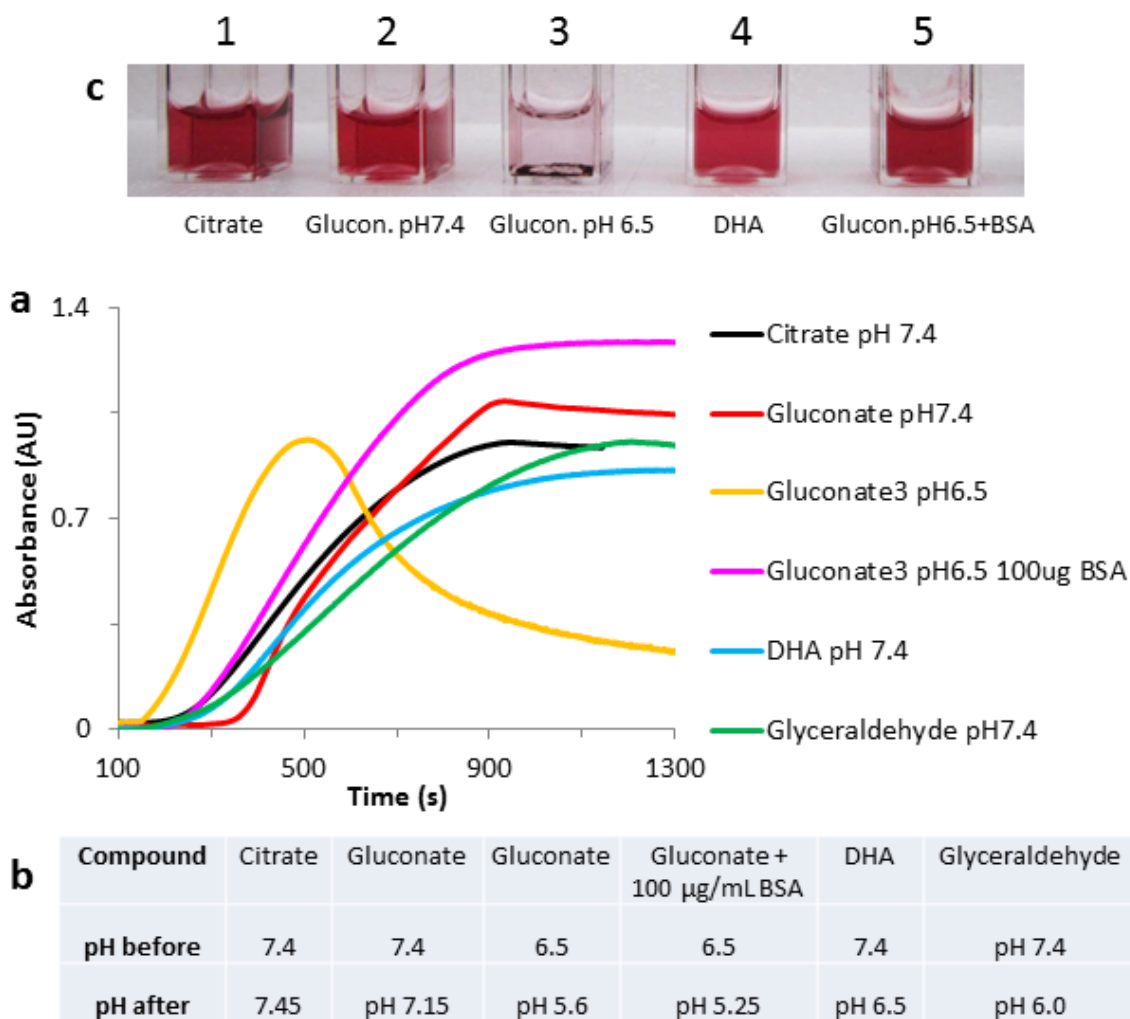


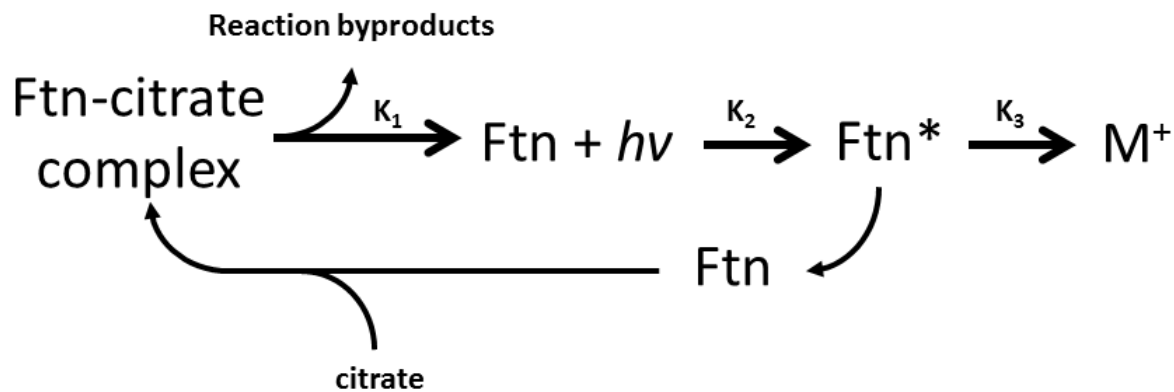
Figure 2-3. AuNPs formation using different electron donors. (a) Kinetic plots of AuNP formation. Each electron donor affects the electron transfer, as shown by the variable lag phases and slopes. (b) pH before and after the photo reaction. The chemistry of the redox reaction influences the final pH. Lower pH increases the efficiency of the reaction but destabilizes the protein shell (yellow line, Fig. A and precipitate Ftn-AuNPs in cuvette #3, Fig. C) (the isoelectric point of ferritin is ~ 5.5). Adding a capping agent like bovine serum albumin (BSA) prevents the precipitation of the products at lower pH (cuvette #5, Fig. C). The reaction product of glyceraldehyde at pH 7.4 looked very similar to cuvette #3, Figure C.

Core Size –The Capacitor Theory

Another possible explanation for the lag phase is the possibility that ferritin acts as a capacitor for storing electrons. As the electron repulsion forces grow with the accumulation of electrons in the FeOOH nanoparticle (NP), the number of electrons transferred to the acceptor increases until reaching equilibrium. The equilibrium is dictated by: first, the electron loading into the particle, which correlates with the concentration of the electron donor; second, the electron excitation dependent on the intensity of the light source, minus the electron-hole recombination events; third, the efficiency of the electron transfer from the mineral core to the acceptor, which is influenced by the concentration and reduction potential of the electron acceptor and by the band gap of the core in a given matrix.

The speed with which electrons are transferred from the electron donor to the final acceptor depends from the slower step of the electron transfer chain (Fig. 4).

It is possible to test the validity of the capacitor theory by observing the formation and the disappearance of a current at the beginning of and after the photolysis. In an experiment performed by Trevor Smith, ferritin was attached to an indium-tin-oxide electrode, immersed in a solution containing citrate and NaCl, and photolysed. A delay in the formation and in the disappearance of a current, respectively, would be consistent with the capacitor model. The formation of a current was observed ammeter. Preliminary data produced by Trevor Smith, from our group, seem to confirm the capacitor theory (Fig. 5). Figure 5 suggests that part of the lag phase during AuNP formation is due to the ability of ferritin to absorb electrons (capacitor effect).



K_1	K_2	K_3
e^- donor	[Ftn]	e^- acceptor
[e^- donor]	Core size	[e^- acceptor]
	[Phosphate]	[O_2]
	$h\nu$ intensity	
Salt, [Salt], Buffer, [Buffer], pH, core composition, temperature		

Figure 2-4. Reaction cycle diagram (top) and parameters affecting the electron transfer (bottom).

The movement of electrons from the electron donor (e.g. citrate), through the photo-catalyst (Ftn), to the electron acceptor (e.g. metal ion) is governed by constants affected by the parameters listed in the table.

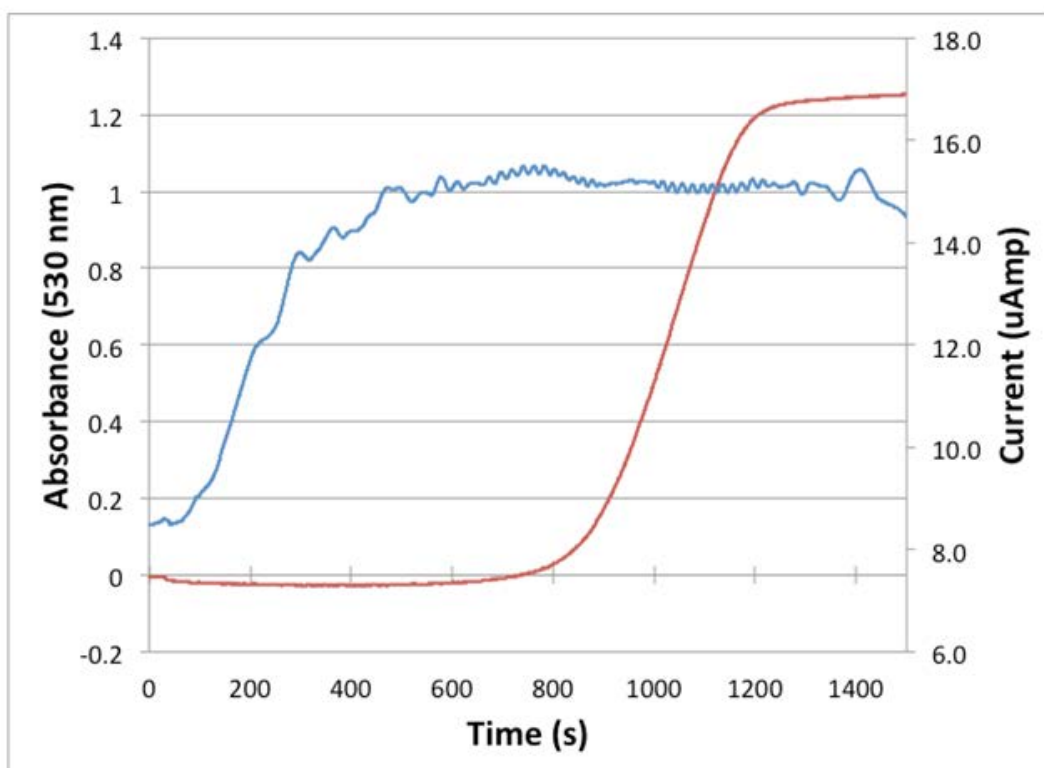


Figure 2-5. Current produced and AuNPs formation by ferritin photochemistry. The left Y axis represents the absorbance at 530 nm measured by UV-Vis spectrometry to monitor the formation of AuNPs (red line). The right Y axis represents the current measured during illumination of a ferritin sample attached to the surface of an ITO electrode. The 800 second lag phase represents the time it took to the AuNPs to reach 2 nm size. The delay and the slow increase in current formation upon illumination before reaching a plateau (blue line) and the slow decrease in current intensity after turning off the light (not shown in this graph) shows that the ferrihydrite core of ferritin acts as a capacitor during the photocatalytic electron transfer. (Graph produced by Trevor Smith).

One elegant experiment similar to that shown in Figure 5, but performed with ferritins bearing various size cores would further confirm the capacitor effect; as the light is turned on, the current produced by smaller cores should appear after a shorter lag phase and increase (or decrease when the light is turned off) more rapidly, when compared to larger cores.

Core Size –Quantum Confinement and Band Gap

The core size can affect the electron transfer also by quantum confinement. Smaller cores should have a higher band gap and should absorb higher energy photons (lower wavelength).¹² The electrons excited to a higher energy level could then be more easily transferred to a variety of electron donors, potentially increasing the effective electron transfer and reducing the electron-hole recombination. An experiment performed by Trevor Smith, a graduate student from our group, confirmed that smaller iron cores possess larger band gaps (Table 1). He has recently submitted a paper that looks at the ability to tune the band gap in ferritin by altering the size, ionic strength and capping agents that are present in the ferritin interior.

Phosphate Layer

Similarly to what was observed with smaller cores, cores bearing a phosphate layer also reduce the lag phase and increase the reaction speed, when compared to same size cores without phosphate. The presence of phosphate might affect the electron transfer efficiency in the following ways: first, by influencing the crystal structure and, as a consequence, the band gap and the surface chemistry; second, by altering the reduction potentials (the extent of the change in electron potential can be measured electrochemically);¹³ third, by changing the Ksp value, which affects the diffusion rate of Fe²⁺ ions outside ferritin. The Ksp of Fe(OH)₃ and iron(III) phosphate are 10⁻³⁶ and 10⁻²², respectively. The band gap could be measured as it was done for

	E_{indirect} (eV)	$E_{\text{defect binding}}$ (eV)	E_{direct} (eV)
native	2.140 ± 0.015	0.220 ± 0.010	3.053 ± 0.080
500 Fe core	2.237 ± 0.012	0.315 ± 0.008	3.119 ± 0.020
1000 Fe core	2.027 ± 0.015	0.266 ± 0.010	3.012 ± 0.030
1500 Fe core	1.916 ± 0.015	0.252 ± 0.010	2.896 ± 0.030

Table 2-1. Band gaps of iron cores of different sizes. The band gap increases as the core size decreases. (Table produced by Trevor Smith).

the various iron core sizes (Table 1). Also, high magnification TEM imaging can be applied to measure the crystal lattice of the core with or without phosphate. The reduction potential of ferritin containing a defined number of iron atoms, with or without phosphate, can be measured electrochemically.

The Influence of Oxygen on the Lag Phase

The photo reduction reactions involving the ferritin photo catalyst and metal ions as electron acceptors were carried out in aerobic environments. In these conditions, oxygen competes with the metal ions in solution for accepting electrons. The magnitude of the effect of oxygen on the lag phase is exemplified in Figure 6. As the stirring speed increases so does the diffusion of oxygen in the solution, which in turn extends the lag phase and slows down the initial particle growth (as visible by the prolonged slower portion of the slope).

Core Mineral Composition

The mineral composition also affects the electron transfer from the electron donor to the electron acceptor as it is evident from the lag phases and the kinetics curves produced by different minerals as shown in Figure 7 (data from David Buck). The mineral composition acts on the electron transfer by altering the reduction potential of the core and the band gap (see Table 1-1).

Core Crystallinity

We noticed differences in the crystallinity of the FeOOH core of native, ferritin reconstituted by adding Fe salts in batches, or ferritin reconstituted by slowly adding Fe salts at a constant rate. In fact, from TEM imaging it seems that the cores of native ferritin have a reduced crystallinity when compared to reconstituted ferritin, which is consistent with the

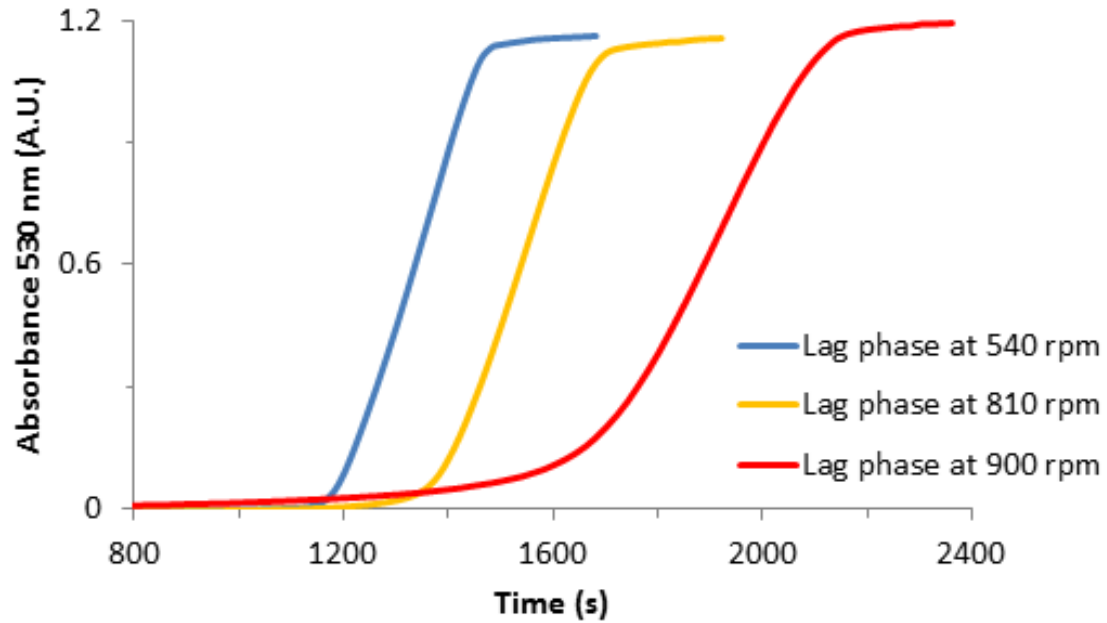


Figure 2-6. Lag phase observed at various revolutions per minute (rpm) of the stir bar. The presence of oxygen contributes to the lag phase and the change in slope of the reaction. Higher stirring speeds increase the diffusion of oxygen into the aqueous solutions delaying the formation and prolonging the initial slow growth phase of NPs, manifested by the longer lag phase and the prolonged duration of the first (more shallow) slope.

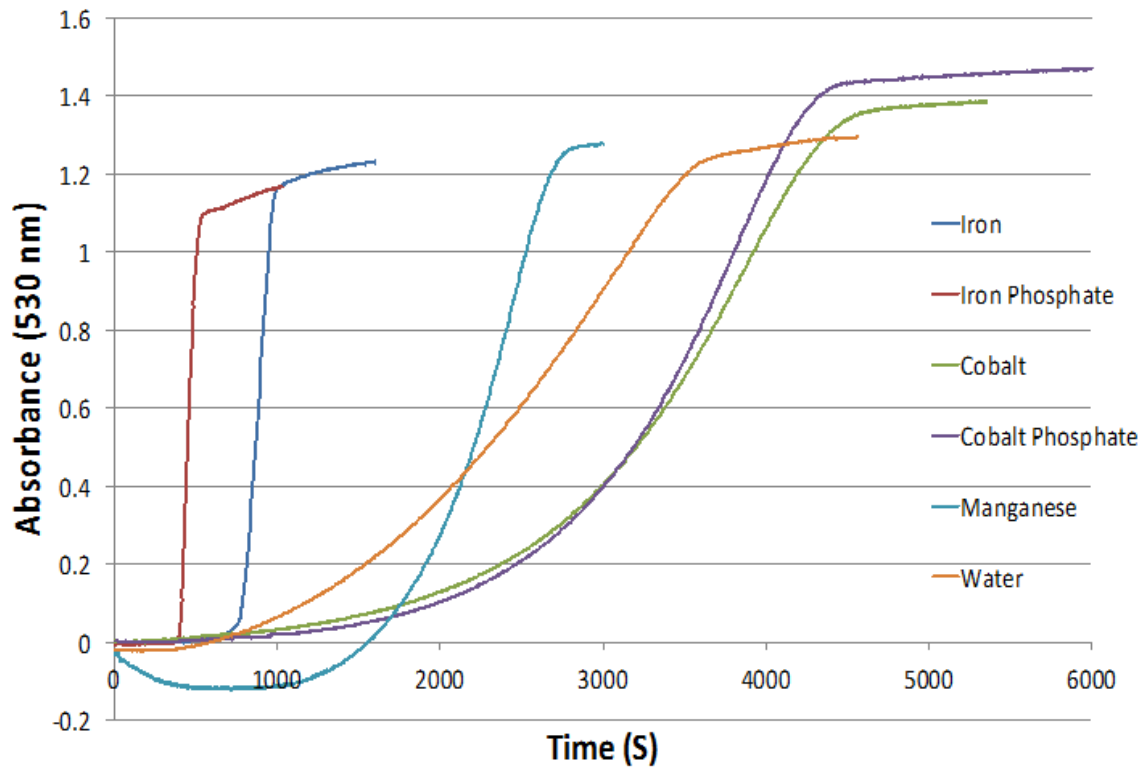


Figure 2-7. Kinetic plots of AuNPs formation using different mineral cores. The mineral core affects the electron transfer (as shown by the variable lag phases and slopes) because each mineral has a different redox potential, band gap, and surface chemistry. (Graph produced by David Buck).

phosphate content that reduces the Fe-O-Fe bridges in native ferritin. Reconstituted ferritin can be prepared by adding iron(II) ammonium sulfate to an apoferritin solution; this can be done in two ways: adding 100-500 Fe/Ftn in batches, spaced out by 30 minute loading times, until the desired ferritin iron load is reached, or by slowly and linearly adding the iron salt over a period of 2-3 hours with a micropump. The iron core seems to be more crystalline when reconstituted slowly. We noticed that apoferritin batches reconstituted slowly produce longer lag phases when utilized in the photochemical synthesis of AuNPs. Furthermore, the lag phase becomes longer as the reconstituted ferritin sample ages. We ascribe the prolonged lag phase of slowly iron-loaded apoferritin and aging holoferritin (ferritin containing a mineral core) to the increased order of crystallinity of the core, but more experiments are needed to confirm this hypothesis. Larger cores have also higher crystallinity,¹⁴ which may further contribute (beside what was said earlier in the Core Size –Quantum Confinement and Band Gap paragraph) to the lower reactivity of the larger iron cores. The change in crystallinity affects the absorbance (as shown by Snow et al.¹⁴), the Ksp, the surface chemistry, and possibly the band gap.

Ferritin Composition

Ferritin is made up of H and L subunits. L subunits possess nucleation sites on the interior of ferritin (not to be confused with the gold nucleation sites on the outside of ferritin) where iron mineral seeds form and begin to grow into the ferrihydrite crystal mineral. The number of nanoparticles inside ferritin can be influenced by the ferritin subunit composition.¹¹

Calculating the Nucleation Event Time Point

As explained in the Capacitor Theory section, by attaching Ftn to an electrode and monitoring the appearance of a current (Fig. 5) one can estimate the time it takes for the photo catalyst to start transferring electrons to the electron donor. What happens between the first

electron transfer (at about 100 seconds according to Fig. 5) and the appearance of the SPR signal between 600 and 1200 seconds (depending on the core size and presence of phosphate, Fig. 3-8) is unclear. The only event that can be assumed is the nucleation of the first gold atom. Figure 8 shows the kinetic curves of AuNP growth mediated by various Ftn cores, with or without a phosphate shell. In figure 8b the a kinetic curve has been split into three sections: 1) an initial linear slow AuNP growth after reaching the 2 nm size (the point where the SPR band is detected by the spectrophotometer); 2) a transition exponential phase, and 3) a linear fast AuNP growth. By using the slope of the slow phase of each kinetic curve one can calculate at which time point the AuNP = 0.27 nm (2 x gold atomic radius). This time point is a good estimate for the nucleation time point event.

Conclusions

As discussed in the previous sections, a variety of factors can influence the mechanism of electron transfer by ferritin photo catalysis. In this chapter I analyzed some of these factors in the attempt to better understand (and potentially optimize) ferritin photo catalytic electron transfer. More experiments suggested along the text of this chapter will further increase our understanding of said mechanism.

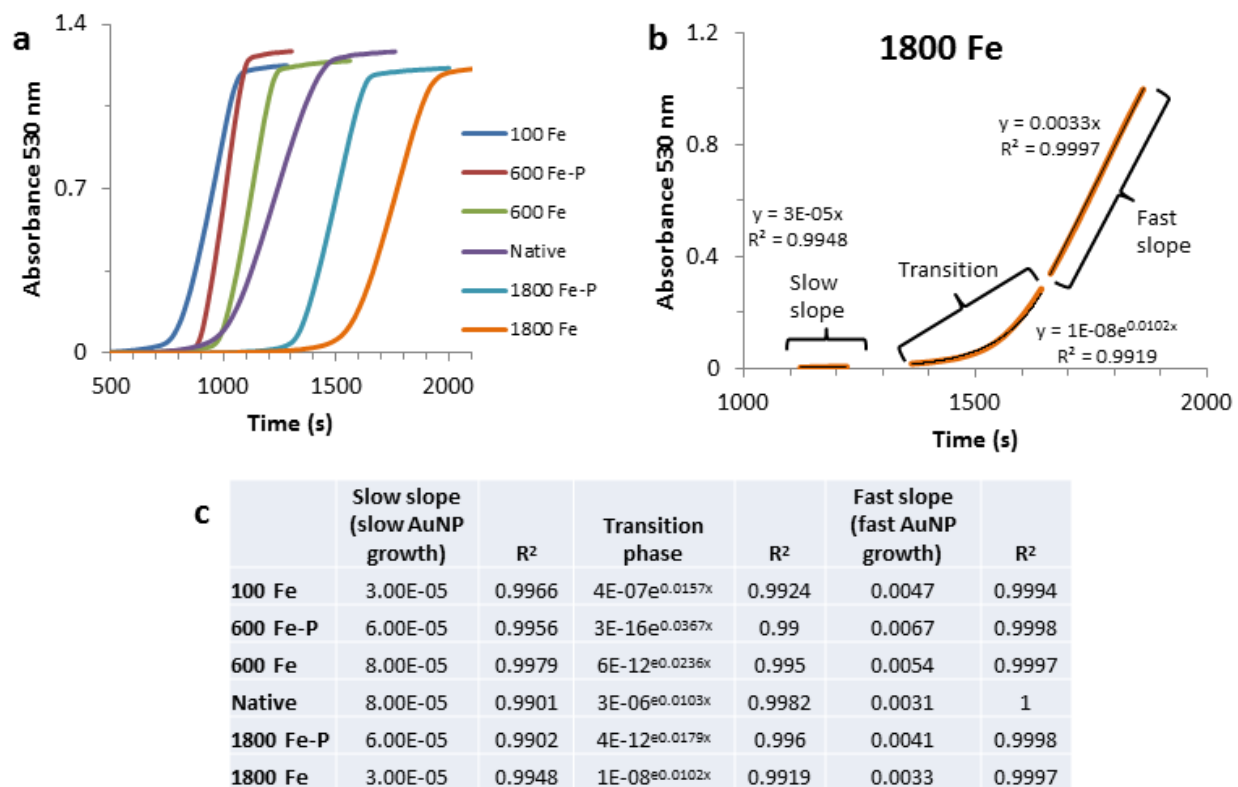


Figure 2-8. Kinetic plots of AuNPs formation using different mineral cores. The mineral core affects the electron transfer (as shown by the variable lag phases and slopes) because each mineral has a different redox potential, band gap, and surface chemistry. (Graph produced by Robert Hilton).

References

1. V. V. Nikandrov, C. K. Gratzel, J. E. Moser and M. Gratzel, *J Photochem Photobiol B*, 1997, **41**, 83-89.
2. I. Kim, H. A. Hosein, D. R. Strongin and T. Douglas, *Chem. Mater.*, 2002, **14**, 4874-4879.
3. D. Ensign, M. Young and T. Douglas, *Inorg. Chem.*, 2004, **43**, 3441-3446.
4. R. J. Hilton, J. D. Keyes and R. K. Watt, SPIE Smart Structures/NDE 2010, San Diego, CA, 2010.
5. J. D. Keyes, R. J. Hilton, J. Farrer and R. K. Watt, *J. Nanopart. Res.*, 2011, **13**, 2563-2575.
6. H. B. Abrahamson, A. B. Rezvani and J. G. Brushmiller, *Inorganica Chimica Acta*, 1994, **226**, 117-127.
7. J. Kimling, M. Maier, B. Okenve, V. Kotaidis, H. Ballot and A. Plech, *The journal of physical chemistry. B*, 2006, **110**, 15700-15707.
8. R. J. Hilton, J. D. Keyes and R. K. Watt, SPIE Smart Structures/NDE 2010, San Diego, CA, 2010.
9. T. Jennings and G. Strouse, in *Bio-Applications of Nanoparticles*, Springer-Verlag Berlin, Berlin, Editon edn., 2007, vol. 620, pp. 34-47.
10. B. Hvolbaek, T. V. W. Janssens, B. S. Clausen, H. Falsig, C. H. Christensen and J. K. Nv[[rskov, *Nano Today*, 2007, **2**, 14-18.
11. J. D. Lopez-Castro, J. J. Delgado, J. A. Perez-Omil, N. Galvez, R. Cuesta, R. K. Watt and J. M. Dominguez-Vera, *Dalton Transactions*, 2012, **41**, 1320-1324.
12. E. O. Chukwuocha, *World Journal of Condensed Matter Physics*, 2012, **02**, 96-100.
13. H. Heqing, R. K. Watt, R. B. Frankel and G. D. Watt, *Biochemistry*, 1993, **32**, 1681-1687.

14. C. L. Snow, L. N. Martineau, R. J. Hilton, S. Brown, J. Farrer, J. Boerio-Goates, B. F. Woodfield and R. K. Watt, *J Inorg Biochem*, 2011, **105**, 972-977.

CHAPTER 3: A FERRITIN MEDIATED PHOTO CHEMICAL METHOD TO SYNTHESIZE BIOCOMPATIBLE CATALYTICALLY ACTIVE GOLD NANOPARTICLES: SIZE CONTROL SYNTHESIS FOR SMALL (~2 NM), MEDIUM (~7 NM) OR LARGE (~17 NM) NANOPARTICLES

A version of this chapter has been published: O. D. Petrucci, D. C. Buck, J. Farrer and R. K. Watt, *RSC Adv.*, 2014, 4, 3472–3481.

Abstract

Ferritin (Ftn) undergoes photo-induced charge separation reactions that oxidize organic substrates. The liberated electrons are transferred through the protein shell to reduce Au ions to gold nanoparticles (AuNPs). We systematically varied the concentrations of citrate (electron donor), Au^{3+} or Au^+ (electron acceptor), and ferritin (photo catalyst) to determine if careful control of these reactant concentrations would: 1) provide size control; 2) alter the morphology of the resulting AuNPs; and 3) alter the catalytic activity of the resulting AuNPs. The size and phosphate content of the ferritin iron core was also evaluated for its influence in this photo catalysis reaction. We report that as the Ftn concentration was increased to an optimal range, the number of AuNPs increased and showed smaller size, more spherical shape, and narrower distribution. Increasing the citrate concentration (electron donor) increased the rate of AuNP formation producing more spherical, uniform sized AuNPs. Increasing the Au^{3+} concentrations increased the number and sizes of the AuNPs. Since Au^{3+} reduction requires 3-electrons we

proposed that using Au^+ would increase the rate of the reaction. The photochemical reaction with Au^+ was faster and produced 2.4 ± 1.0 nm diameter AuNPs providing another method of size control. AuNPs were tested as reduction catalysts to convert 4-nitrophenol into 4-aminophenol. The smaller spherical AuNPs were better reduction catalysts than the larger AuNPs. In summary, using a single photochemical synthesis method we can reproducibly control the size, uniformity and catalytic activity of the resulting AuNPs simply by varying the concentrations or oxidation states of the reactants.

Introduction

Gold Nanoparticles (AuNPs) have been the focus of major research efforts over the last ten years ¹⁻³. Nanoparticles (NP) offer large surface to volume ratios and size constraints that leave exposed atoms capable of catalysing reactions otherwise impossible for the same elements as bulk materials ⁴. The characteristics essential for NP catalytic ability are: small size, narrow size range, and consistent shape ⁵. Many laboratories have devoted a significant effort to improve their AuNP synthesis in order to reduce the size, control the size distribution, and avoid aggregation of the resulting AuNPs ^{1, 6-8}. In this study, our goal was to use a single synthesis method, and by varying the concentrations of the reactants, control the size, morphology, and catalytic activity of the resulting AuNPs.

Another important goal was to prepare AuNPs in biocompatible media because of the increasing number of biomedical applications for AuNPs ^{9, 10}. Many AuNP synthesis protocols utilize surfactants, polymers, or substituted allylic compounds like tri-*n*-octylphosphine oxide, polyvinylpyrrolidone, or dialkyl sulfides to prevent AuNPs from clustering and/or precipitating ¹¹⁻¹³. These compounds are either toxic or their safety in biological systems have been called into question ¹⁴⁻¹⁶. The method described in this study uses all biocompatible reactants to synthesize AuNPs.

AuNPs have been used in a variety of biological applications. Remarkably, AuNPs preferentially accumulate at tumor sites ¹⁷ so using AuNPs as vehicles to deliver drugs to tumors is an obvious application ^{17 18 19 20 21 22}. Other applications include imaging ¹⁸, biosensing ¹⁸, other targeted drug delivery applications, conjugation to drugs, and photo thermal therapy treatments in oncology ^{18 17 19 20 21 22}. The structure, size, shape and surface ligation of these AuNPs are critical for each application.

Recently ferritin (Ftn) has been used to synthesize AuNPs inside Ftn^{23,24}, or outside Ftn where the AuNPs assemble on the Ftn exterior^{25, 26}. Ftn is a 24-subunit protein complex (450 kDa) with a spherical structure measuring 12 nm in diameter with an 8 diameter nm hollow interior²⁷. Ftn has evolved to bind Fe(II), oxidize it to Fe(III) with its catalytic enzyme site known as the ferroxidase center, and sequester the iron in its interior to form ferrihydrite (FeOOH)^{28,29}.

In this work our goal was to synthesize AuNPs on the exterior of Ftn. For AuNP synthesis on the Ftn exterior, the protein nano cage appears to have a two-fold purpose. First, Ftn possesses ideal AuNP nucleation sites on the external surface at the 3-fold channels because there are three cysteine residues at the opening of this channel (Fig. 1)²⁵⁻²⁷. The cysteine residues are ideal as a nucleation site for AuNP deposition because of the thiophilic nature of gold^{30, 31}. Once bound, Au(III) can be reduced to Au(0) by chemical reductants or by light-driven reactions^{25, 26}. Second, Ftn prevents the aggregation and precipitation of the AuNPs by acting as a capping agent²⁶. Keyes et al. demonstrated that the AuNPs co-migrated with ferritin through a gel filtration column indicating a sufficiently strong interaction that could be used for targeted AuNP delivery based on cellular destinations for serum ferritin²⁵. Remarkably, tumor cells are often iron-deficient and iron-deficient cells express receptors that endocytose ferritin to satisfy iron needs³². Preparing Ftn-AuNP conjugates may be an additional mechanism to deliver AuNPs to tumor cells.

The photochemical method to synthesize AuNPs with Ftn has additional advantages because it eliminates any contamination from strong chemical reducing agents or their by-products. Ftn is a photo catalyst because the ferrihydrite semi-conductor mineral core can undergo charge separation reactions when exposed to light. Illumination of Ftn promotes an

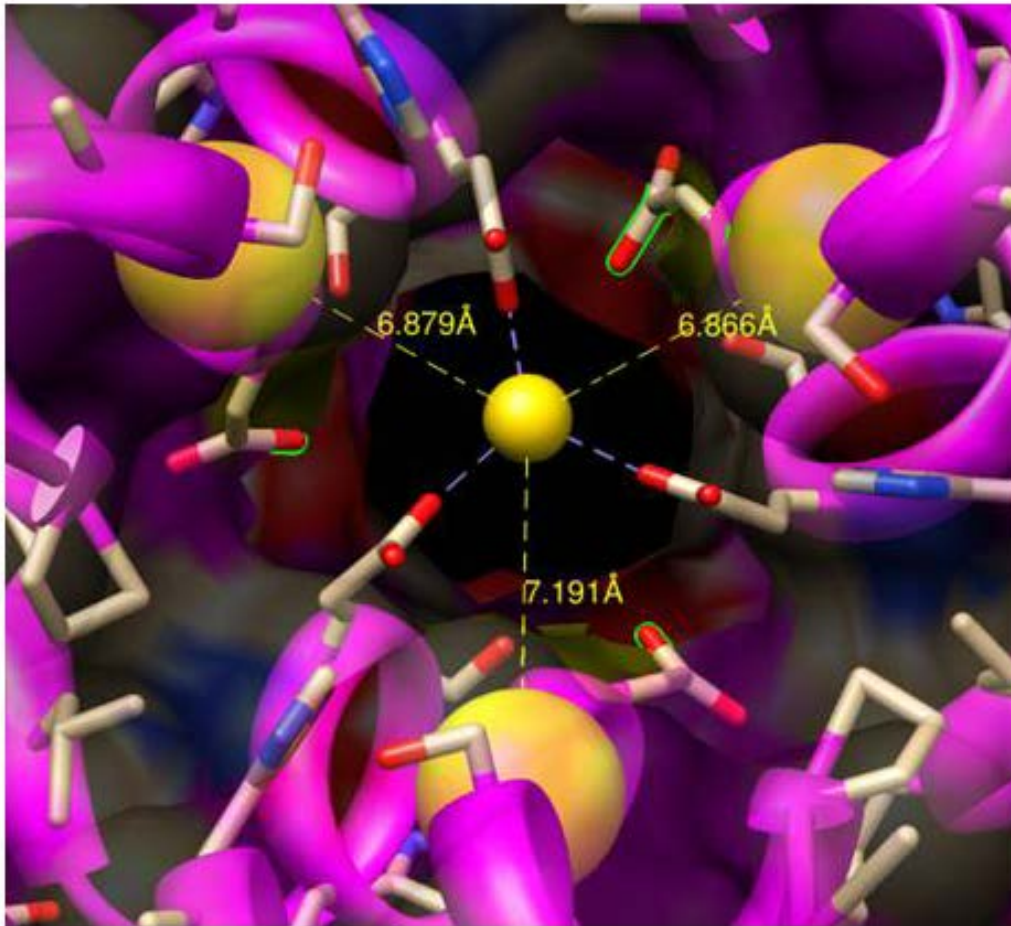
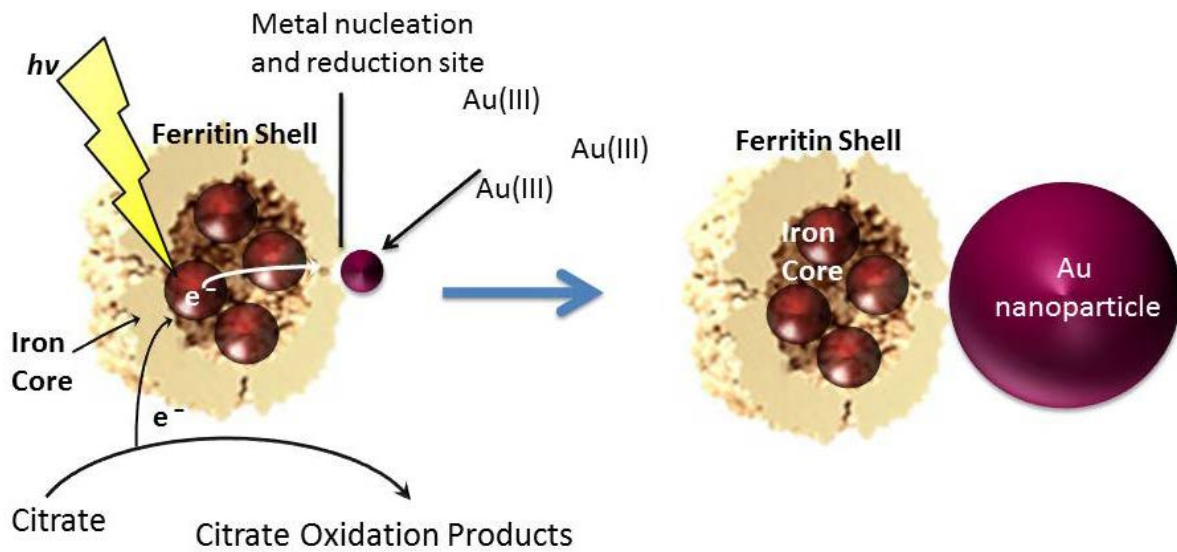


Figure 3-1. Crystal Structure of the 3-fold channel of ferritin – Proposed gold nucleation site. This view is from the outside of ferritin looking toward the interior. The conserved negative residues (red atoms) in the 3-fold channel of ferritin attract the cations; the three cysteine residues (the three large yellow spheres) bind the gold atoms facilitating the nucleation of the AuNP.

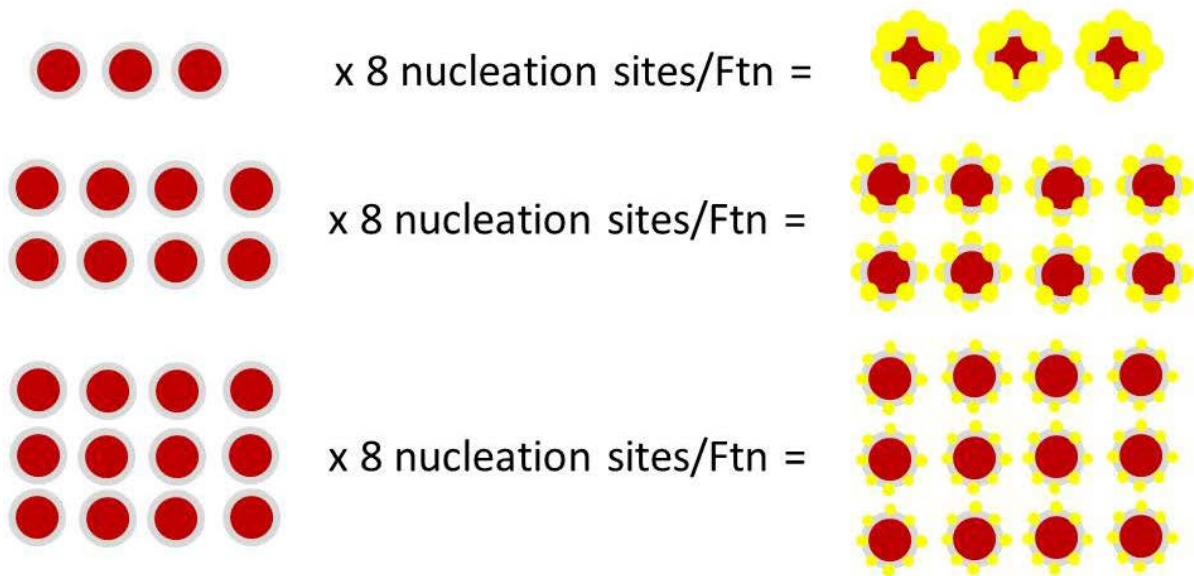
electron from the valence band to the conduction band (2.5-3.5 eV)³³ and the excited electrons are ultimately transferred to Au(III) ions bound on the exterior surface of Ftn²⁵. The electron donors in this system are sacrificial bio-organic molecules that donate electrons to fill the hole created by the photochemical reactions and are typically citrate, tartrate, or oxalate. Scheme 1 represents this process and shows the formation of AuNPs on Ftn.

In this study, reaction conditions were varied to allow control over the morphology, size, and catalytic properties of the resulting AuNPs synthesized by the photochemical method. We hypothesized that changing the concentrations of Ftn, citrate, and AuCl_4^- could influence the size, shape, quantity, and aggregation state of the AuNPs. Based on the proposal that the cysteine residues in the 3-fold channels of Ftn act as AuNP nucleation sites (Fig. 1), we predicted that higher Ftn concentrations would produce more AuNPs with smaller sizes using the same AuCl_4^- concentration, whereas lower Ftn concentrations would produce fewer but larger AuNPs (Scheme 2). Because AuNPs can also act as nucleation sites for Au^{3+} , we also predicted that the AuNPs formed with low Ftn concentrations would be more irregularly shaped due to the non-specific nucleation of Au^{3+} on the growing AuNPs (gold seed effect)²⁶.

We also hypothesized that high citrate concentrations should favour the specific Ftn-mediated photo-catalysis reactions and minimize the non-specific reactions. Additionally, citrate will assist in the passivation of the AuNPs, whereas low citrate concentrations would increase non-photo catalysed nucleation and synthesis events and gold seed growth. Also, in low citrate conditions Ftn can act as an electron donor; thus under limited electron donor conditions Ftn is damaged by photo-oxidation³⁴. Therefore, low citrate concentrations could lead to enhanced Ftn



Scheme 2-1. Ferritin containing an iron mineral absorbs light and transfers the excited electrons to Au(III) ions bound to the nucleation sites on the exterior of the ferritin protein shell. This process oxidizes citrate to replenish the electrons for further reactions. Continued light exposure allows the AuNPs to grow to larger sizes.



Scheme 3-2. AuNPs formation model. The NP size is affected by the concentration of ferritin (Ftn) in solution and by the number of nucleation sites. At low concentrations of Ftn the gold concentrates on fewer nucleation sites, thus forming larger particles (top figure). If more nucleation sites are present the Au^{3+} will be distributed on a larger number of AuNPs, which will remain smaller (center and bottom figure).

oxidation and decreased AuNP passivation. The resulting AuNPs would show increased clustering and precipitation and reduced catalysis. Hence, the results of the lower citrate concentrations should somewhat resemble those of low Ftn concentrations. Finally, increasing the AuCl_4^- concentration should favour self-nucleating (gold seeds) and auto catalytic events, whereas lower AuCl_4^- concentrations should slow down the formation of AuNPs. The results presented in this paper are consistent with the model explained above and summarized in Scheme 2.

Materials and Methods

Horse spleen Ftn (also referred to as native Ftn) was purchased from Sigma-Aldrich (Sigma F4503) and treated by the thioglycolic method to prepare iron-free or apo Ftn (Apo) as described previously³⁵. Ftn protein concentrations were determined by the Lowry method³⁶. After the preparation of apo Ftn, the buffer was exchanged by dialysis to 25 mM 3-(N-morpholino)propanesulfonic acid (MOPS) pH 7.4 with 100 mM NaCl. The concentration of the Apo after the dialysis steps was 28 mg/mL.

Two, 2 mL samples of the Apo were reconstituted with 600 or 1800 Fe/Ftn, by adding the appropriate volumes of ferrous ammonium sulfate prepared in 40 mM HCl and maintaining the pH of the Ftn sample above 7.0 by adding NaOH. The Fe^{2+} -HCl and the NaOH solutions were injected at 6 $\mu\text{L}/\text{min}$ into the Apo solution using a micro-syringe device (Harvard Instruments) while aerobically stirring the solution throughout the titration. The re-mineralized or reconstituted Ftn was dialyzed against 100 mM NaCl and 10 mM TRIS-HCl pH 7.4 to exchange the buffer.

After the dialysis, 1 mL of the 600 Fe/Ftn and 1 mL of the 1800 Fe/Ftn were removed from the dialysis bags, transferred into clean tubes, and stored at 4°C, while 1 mL of both the 600 Fe/Ftn and the 1800 Fe/Ftn samples were left in the dialysis bag and further dialyzed against 100 mM NaCl and 10 mM TRIS-HCl pH 7.4 containing 5 mM phosphate. After 48 hours both samples were dialyzed again (three times) against 100 mM NaCl and 10 mM TRIS-HCl pH 7.4 to remove the unbound phosphate. The protein, phosphate, and iron contents in all Ftn samples were quantified using the Lowry, the phospho-molybdate, and the bipyridyl methods described previously³⁷.

Samples (1.0 mL in quartz cuvettes) were prepared for the photochemistry reactions in an Agilent 8453 UV/Vis spectrophotometer with a temperature controlled water-jacketed cuvette holder maintained at 25°C by a circulating water bath. Each sample was exposed to a UV-Vis floodlight (Integrated Dispensing Solutions, Inc.) equipped with a 400 W metal halide bulb and the reaction was monitored in the 200-1100 nm range in kinetic mode for the length of the reaction.

We took advantage of AuNP surface plasmon resonance (SPR) to monitor the progress of the photo catalytic AuNP synthesis in real time. When AuNPs reach 2 nm in diameter they start producing a SPR peak between 520-530 nm³⁸. The peak of absorbance shifts to wavelengths longer than 530 nm (red-shift) when the AuNPs grow larger than 20 nm, or if the AuNPs cluster together.

Our synthesis utilized Ftn both as photo-catalyst and capping agent, citrate as sacrificial electron donor and additional capping agent, and AuCl₄⁻ or AuCl as sources of Au(III) and Au(I), respectively. A UV-Vis floodlight (Integrated Dispensing Solutions, Inc.) provided the

energy necessary to transfer the electrons from the citric acid to the Au^{3+} ions. A similar photochemical system to form nanoparticles has been used by others^{25, 39-41}.

We were interested in discovering how varying the concentrations of the reagents used in the photochemical synthesis of AuNPs affect the rate of the reaction and the characteristics of the final AuNPs produced. The conditions reported by Keyes *et al.* were used as our starting (basal) conditions to create the AuNP²⁵ and are: 50 mM NaCl, 20 mM TRIS-HCl pH 7.4, 400 μM KAuCl_4 , 30 mM Na-citrate, 150 $\mu\text{g/mL}$ Ftn (0.34 μM) (all from Sigma-Aldrich).

We systematically altered one variable in each experiment as follows: Ftn (300 $\mu\text{g/mL}$, 150 $\mu\text{g/mL}$, 50 $\mu\text{g/mL}$, 10 $\mu\text{g/mL}$, and zero Ftn as the no Ftn control), citrate (100 mM, 30 mM, 10 mM, 2mM, and zero citrate), and Au^{3+} (500 μM , 400 μM , 300 μM , 200 μM , and 40 μM). For AuNPs synthesis from Au^+ the following reagent concentrations were used: 50 mM NaCl, 20 mM TRIS-HCl pH 7.4, 400 μM AuCl, 100 mM Na-citrate, 200 $\mu\text{g/mL}$ Ftn (0.45 μM).

Transmission electron microscopy (TEM) and high-resolution electron microscopy (HRTEM) experiments were performed on a Tecnai F30 operating at 300 kV. AuNP samples for TEM analysis were collected at the peak of absorbance measured at 530 nm.

Catalytic properties of the AuNPs

As a model to test the catalytic properties of the AuNPs produced by our method we followed the protocol described by Zhang *et al.*²⁶ modified as follows: 1.25 mL of deionized water, 500 μL of 0.2 mM 4-nitrophenol, and 50 μL of freshly prepared 0.1 M NaBH_4 solutions were placed in a standard quartz cuvette, which was then placed in the spectrophotometer cuvette holder set at 25°C under constant stirring. The spectrophotometric recording was started in kinetic mode at 10 seconds intervals upon addition of 200 μL of freshly prepared AuNPs.

Reaction controls contained buffer and citrate alone or buffer, citrate, and ferritin, but without AuNPs (Fig. 2-10a).

Results

Spectrophotometric methods have been used previously to monitor the photochemical formation of AuNPs^{25, 26, 42-44}. In this report, a series of experiments were performed varying the concentrations of the reactants to determine if changes in reactant concentrations could be used to control the size, morphology or catalytic reactivity of the resulting AuNPs. The rate of the reactions was monitored and the resulting products were characterized.

Varying Ftn Concentrations

Figure 2A monitors kinetically the formation of the AuNPs by following the appearance of the AuNPs surface plasmon resonance (SPR) at 530 nm⁴⁵. It is important to note that each reaction has a lag phase prior to the initiation of AuNP absorbance. The plasmon resonance of AuNPs is not observable until the AuNPs are ~2 nm in diameter so the AuNPs must reach this size before they are detected by the spectrophotometer. No formation of AuNPs occurs in the absence of Ftn or the absence of light, demonstrating the absolute requirement of Ftn as the photo catalyst.

The first point of interest in Figure 2A is that the highest Ftn concentration has the longest lag phase before AuNP detection occurs. The model in Scheme 2 shows that as Ftn increases, the number of AuNPs increases but the size of the AuNPs decreases. The large number of seed AuNPs bound to the higher concentrations of Ftn all compete for Au³⁺ ions in solution and it requires a longer time for each of these seed AuNPs to reach 2 nm where the SPR absorbance occurs. When the Ftn concentration is low, there are fewer nucleation sites allowing

the few AuNPs that form to grow more rapidly because there are fewer AuNPs competing for free Au^{3+} ions in solution. These particles reach 2 nm more rapidly and have a shorter lag phase.

The slope in Figure 2A monitors the rate of formation of the AuNPs once the AuNPs reaches the 2 nm diameter threshold where the SPR can be observed. As the Ftn concentration increases, the rate of AuNPs formed will also increase because there will be more seed AuNPs for growth. Consistent with this hypothesis, Figure 2A shows the slope increasing with increasing Ftn concentrations, up to 150 μg Ftn/mL. It is interesting to note that the slope decreases in the 300 μg Ftn/mL sample (Fig. 2A). The decrease in slope in the 300 μg Ftn/mL sample occurs because the formation of the large number of AuNP seed particles has depleted the Au^{3+} ions in solution, and the Au^{3+} ions are limiting in the reaction. In fact, using more gold (800 μM) in the presence of 300 μg Ftn/mL increases the steepness of the slope as expected if the gold ions were limiting in the previous reaction (data not shown).

Figure 2B shows the final spectrum of each of the samples prepared at varying Ftn concentrations. The no Ftn control shows very little production of AuNPs (no absorbance peak at 530 nm). The 10 μg Ftn/mL sample has a broad absorption peak around 560 nm but as the Ftn concentration increases the AuNP peak wavelength moves to shorter wavelengths and becomes sharper. These data suggest that the AuNPs forming at higher concentrations of Ftn are smaller and do not aggregate⁴⁵. Figure 2C shows photos of the samples at the end of the reactions demonstrating the effect of altered Ftn concentrations on the colour of the final product.

The TEM images shown in Figure 3 confirm that the AuNPs formed in the presence of 10 and 50 μg Ftn/mL are larger, more irregularly shaped particles, and tend to aggregate more than the samples that form at higher Ftn concentrations (150 and 300 μg Ftn/mL). Histograms in Figure 3 (sizes measured from multiple TEM images, some exemplified in Supplemental

Figure 1) demonstrate that as the Ftn concentration increases, the number of AuNPs increases and the resulting AuNPs are smaller due to the larger number of nucleation sites and the capping of the AuNPs by Ftn. Additionally, as the Ftn concentration increases, the distribution in size of the particles decreases (compare the distribution of the 50 $\mu\text{g/mL}$ sample with the 150 $\mu\text{g/mL}$ sample). TEM images confirm that when Ftn concentrations are 150-300 $\mu\text{g Ftn/mL}$, the formation of AuNPs is more consistent in size and shape with an average diameter around 7 nm.

Varying Citrate Concentrations

Figure 4A and 4B show the kinetics and spectra for the formation of AuNPs as the citrate concentration is varied. The standard citrate concentration used by Keyes *et al.* (30 mM) yields a sigmoidal shape for the kinetic curve of AuNP formation. Increasing the concentration of citrate to 100 mM reduces the lag phase and makes the slope steeper, consistent with a more abundant supply of electrons (Fig 4A). Additionally, the higher concentration of citrate shifts the absorbance maximum peak from 530 nm to 520 nm (Fig. 4B), producing a lighter red solution (Fig. 4C), and forms spherical AuNPs of smaller average size (Fig 5). The lower overall absorbance of the AuNPs at 100 mM citrate is due to the lower extinction coefficient of smaller AuNP⁴⁵. Taken together, these data suggest that the higher citrate concentration enhances the photo catalysed AuNP formation reactions by providing an abundant supply of electrons.

When the citrate concentration is decreased below 30 mM, the lag phase shortens, the kinetic slope becomes shallow (Fig. 4A), the spectrum broadens and shifts to longer wavelengths (Fig. 4B), and the particles become fewer, larger, and more irregularly shaped (Fig. 5). These observations are all consistent with slower reactions that are associated with a decreased source of electrons and less capping of the AuNPs as they form, resulting in non-specific AuNP production²⁵. Additionally, the lack of passivation by citrate contributes to

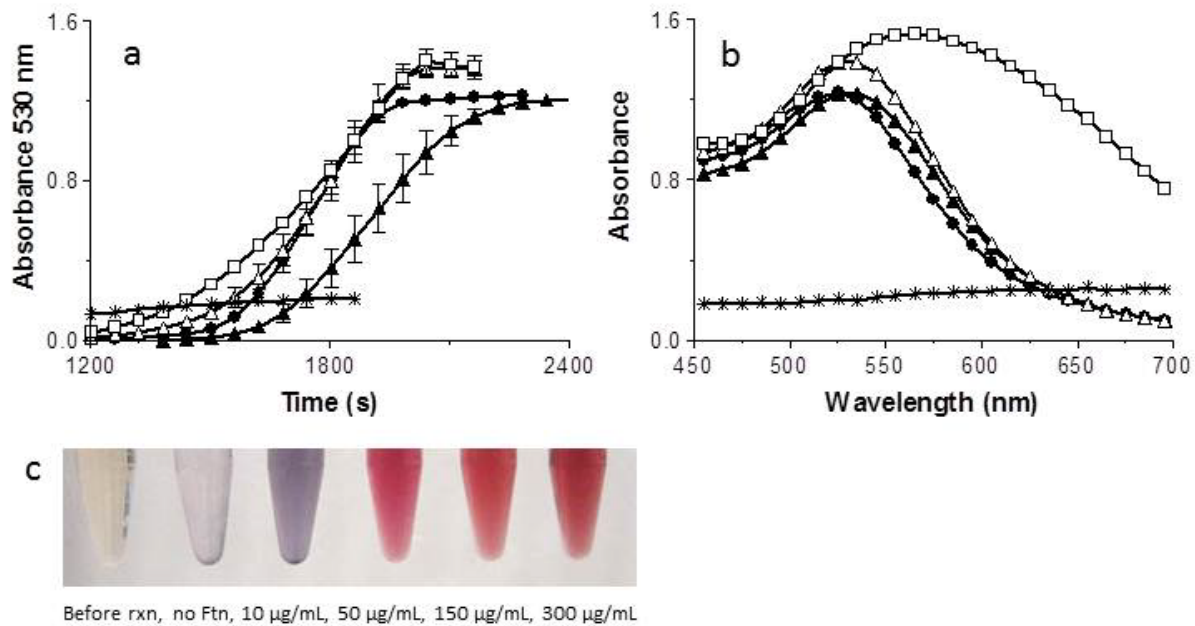


Figure 3-2. Kinetic traces (a) and absorption spectra (b) of AuNPs formed in the presence of no ferritin (Ftn) (*), 10 $\mu\text{g}/\text{mL}$ Ftn (\square), 50 $\mu\text{g}/\text{mL}$ Ftn (Δ), 150 $\mu\text{g}/\text{mL}$ Ftn (\bullet), or 300 $\mu\text{g}/\text{mL}$ Ftn (\blacktriangle). The results are the means \pm the S.D. of at least two independent experiments. (c) Tubes containing the AuNP reaction solutions before the reaction (far left), with no Ftn (reaction control, second from the left), and with increasing concentrations of Ftn corresponding to the samples shown in a) and b) (10 $\mu\text{g}/\text{mL}$ Ftn (\square), 50 $\mu\text{g}/\text{mL}$ Ftn (Δ), 150 $\mu\text{g}/\text{mL}$ Ftn (\bullet), or 300 $\mu\text{g}/\text{mL}$ Ftn (\blacktriangle)). No reactions occurred in the absence of light.

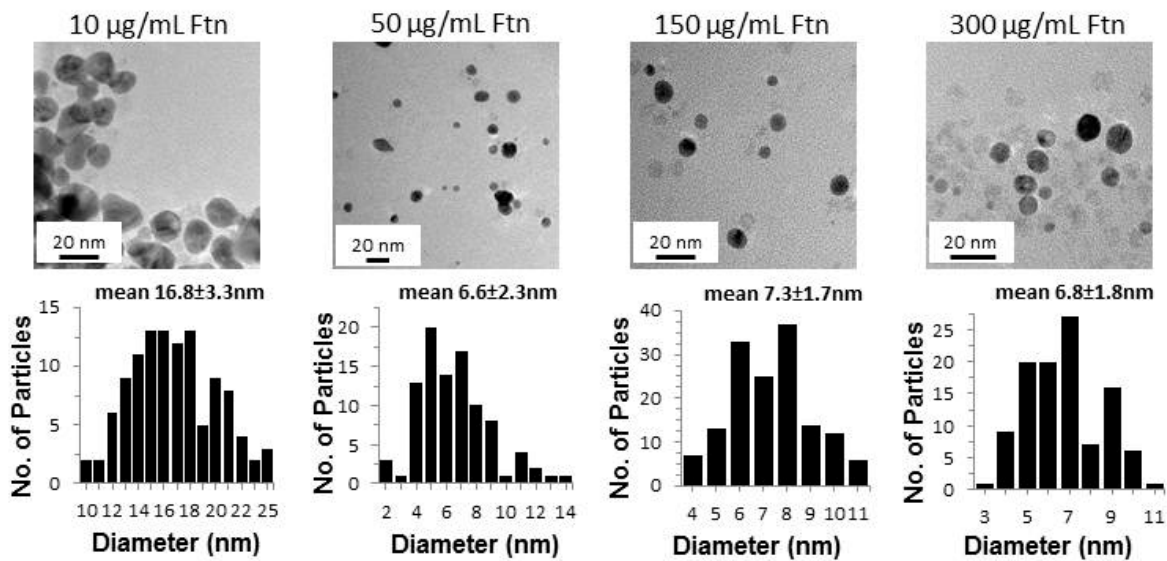


Figure 3-3. TEM images of the AuNPs at increasing concentrations of ferritin (Ftn) (top row, left to right) and histograms of the corresponding particle size distributions (bottom row). The size distribution of the particles is the result of data collected from several micrographs. The light grey dots visible in the micrographs are the 7-8 nm iron cores of ferritin.

the formation of larger NP due to aggregation⁴⁶. One piece of data that seems inconsistent with this interpretation is the fact that the lag phase is shorter with lower citrate concentrations. Nikandrov also reported this phenomenon and demonstrated that in the absence of a suitable electron donor, the Ftn protein shell became the electron donor and was degraded³⁴. The protein-mediated reduction of AuNPs and the resulting damage to the protein causes an increase in the absorbance throughout the entire spectrum of the sample and caused a shortened lag phase. Also, all of the gold ions available will assemble onto the few particles formed, allowing them to quickly grow above 2 nm, thus recapitulating the results seen at low Ftn concentrations.

Figure 3-5 shows the TEM micrographs and size histograms (sizes measured from multiple TEM images, some exemplified in Supplemental Fig. 2) of AuNPs in the presence of 150 µg/mL of Ftn with 2 mM, 10 mM, 30 mM, and 100 mM citrate, respectively. At 2 mM citrate the NP tend to grow larger than 20 nm, fuse to each other and take an amorphous shape, whereas the AuNPs become smaller and more spherical as the citrate concentration increases from 10 mM to 100 mM. Other evidence of the increase in size can be seen visually (Fig. 4C) as the samples change from red to purple with the decrease of the citrate concentration. It is clearly visible that the 10 mM and 2 mM citrate samples appear a blue-violet colour instead of the red colour observed in the other samples. The aggregated AuNPs in the 2 mM sample partially precipitated in a few hours.

Varying Gold Concentrations

Varying the Au³⁺ concentration produced some obvious challenges because gold is absolutely essential for product formation. Figure 6A and B show the kinetics and spectra of the AuNP formation at various Au³⁺ concentrations. At 40 µM Au³⁺ there is almost no formation of

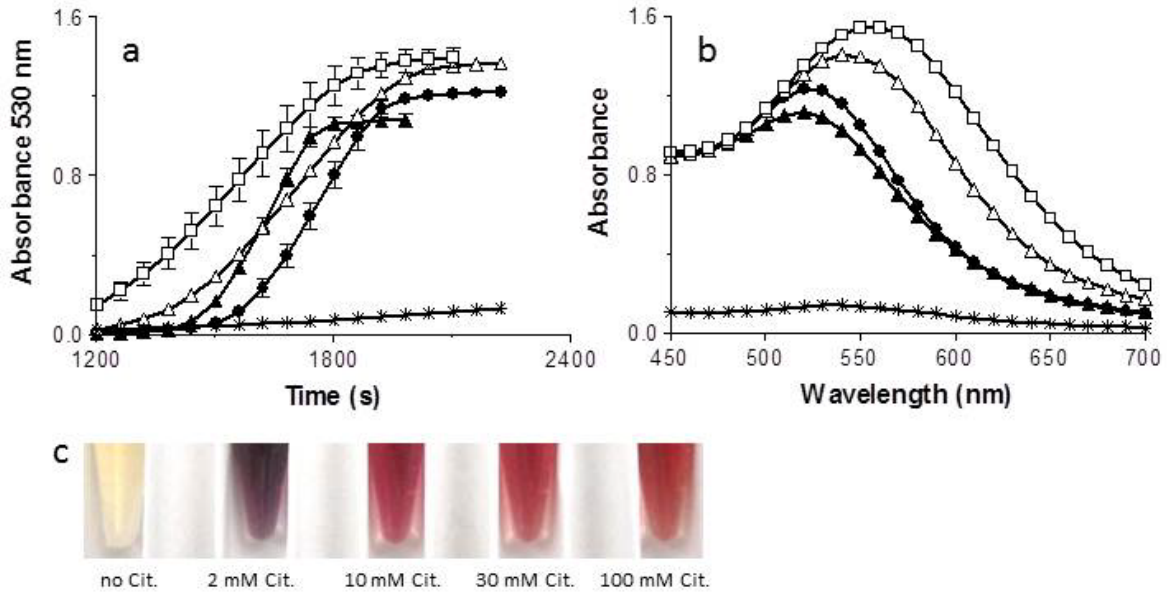


Figure 3-4. Kinetic traces (a) and absorption spectra (b) of AuNPs formation in the presence of no citrate (*), 2 mM (□), 10 mM (Δ), 30 mM (●), or 100 mM citrate (▲). The results are the means \pm the S.D. of at least two independent experiments. (c) Tubes containing the AuNP reaction solutions with no citrate (far left), and with increasing concentrations of citrate (left to right) corresponding with the concentrations given above (2 mM (□), 10 mM (Δ), 30 mM (●), or 100 mM citrate).

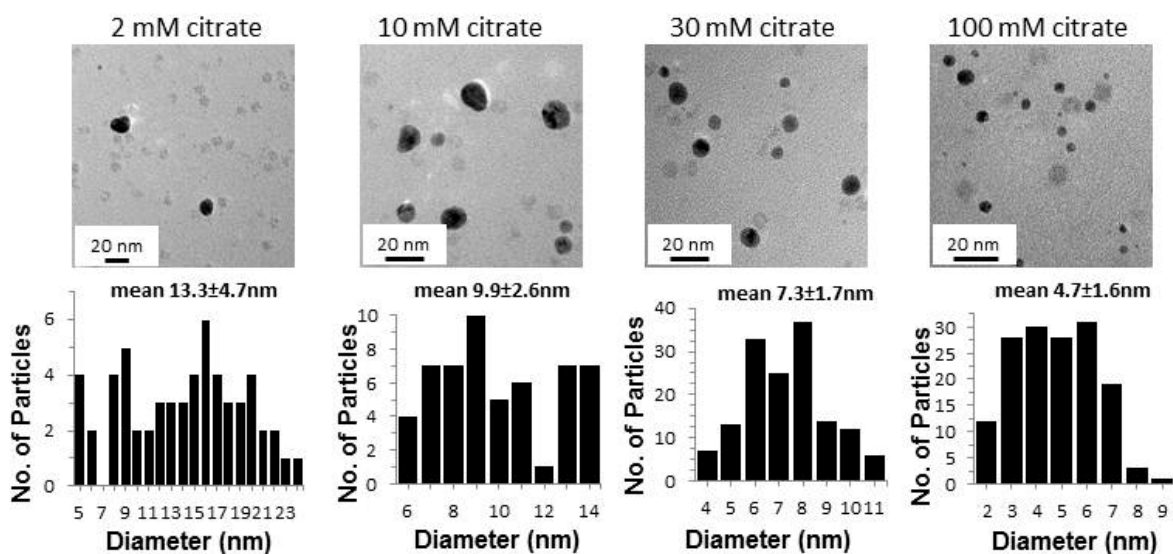


Figure 3-5. TEM images of the AuNPs at increasing concentrations of citrate (top row, left to right) and histograms of the corresponding particle size distributions (bottom row). The size distribution of the particles is the result of data collected from several micrographs. The light grey dots visible in the micrographs are the 7-8 nm iron cores of ferritin.

AuNP as is evident by no change in the kinetic plot (Fig. 6A) and the almost-zero absorbance throughout the whole spectrum (Fig. 6B). The absorbance increases and the lag phase decreases as the Au^{3+} concentration increases from 200 to 500 μM (Fig. 6A). The spectra peak at 520 shifts to higher wavelengths as the Au^{3+} concentration increases (it shifts about 2 nm for every 100 μM increase in Au^{3+} concentration up to 600 μM). Beyond 600 μM the red shift is rapid (data were collected but are not shown here because the absorbance was above the detection limit of the spectrophotometer). As expected, increasing the Au^{3+} concentration increases the final absorbance due to more AuNP formation. This is evident upon visual inspection as the samples become darker as the Au^{3+} concentration increases (Fig 6C). The TEM images and histograms (Fig. 7) confirm an increase in the number of the AuNP as well as a slight increase in size of the particles as the gold concentration increases from 200 to 500 μM Au^{3+} (see supplemental figure 3 for additional TEM images. Note that the 40 μM Au^{3+} sample did not produce sufficient particles for a proper histogram.

Effect of ferritin iron core size and phosphate content on photo catalysis

An important part of controlling the size of the AuNPs is gaining a better understanding of the catalyst that is being used. Ensign *et al.* reported that smaller cores react faster than larger cores during the reduction of Cu(II) to Cu(0) ³⁹. However, in their experiments they keep the concentration of the total iron constant but doubled the concentration of the protein. Therefore, as they state in their paper, “it is not certain whether the higher speed of reaction of the smaller core should be attributed to the smaller cores or to the higher concentration of Ftn”.

We desired to further evaluate the influence of the core size and, additionally, the effect

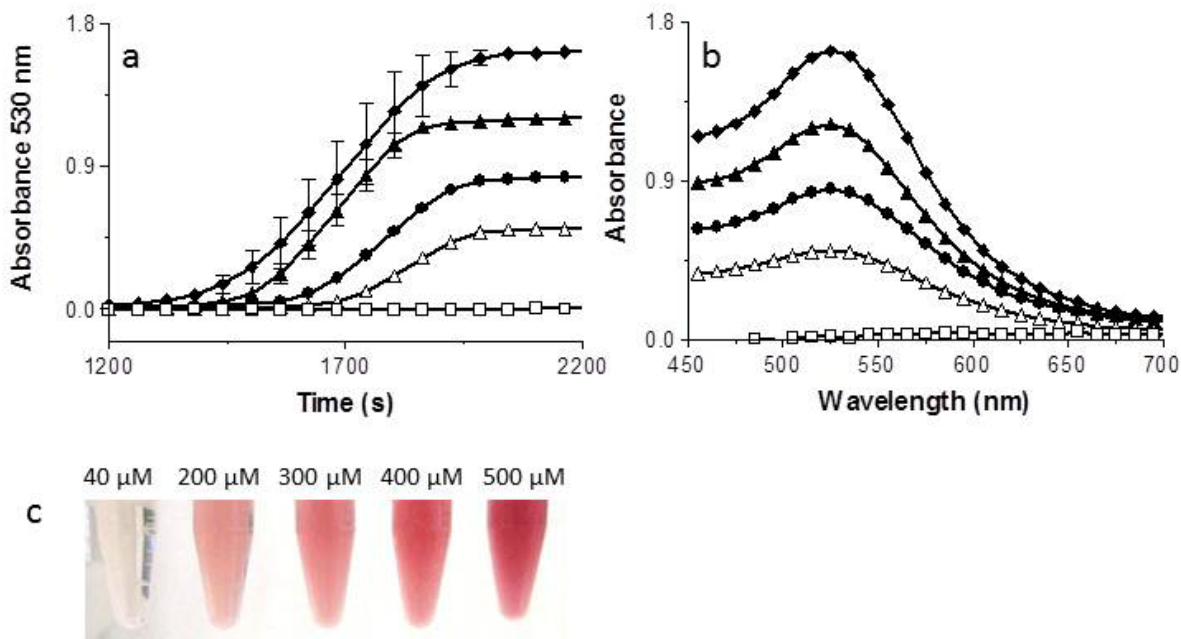


Figure 3-6. Kinetic traces (a) and absorption spectra (b) of AuNPs formation in the presence of 40 μM (\square), 200 μM (Δ), 300 μM (\bullet), 400 μM (\blacktriangle), or 500 μM Au^{3+} (\blacklozenge). The results are the means \pm the S.D. of at least two independent experiments. (c) Tubes containing the AuNP solutions with increasing concentrations of Au^{3+} (left to right).

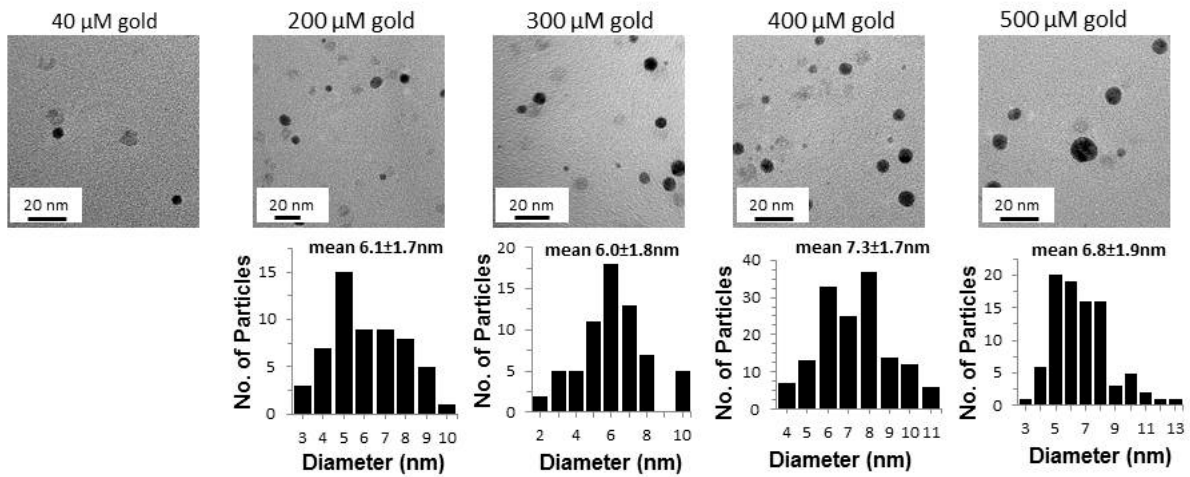


Figure 3-7. TEM images of the AuNPs at increasing concentrations of Au³⁺ (top row, left to right) and histogram of the corresponding particle size distributions (bottom row). Too few particles were formed at 40 μM gold, hence a statistically significant particle size distribution graph could not be created (bottom left). The size distribution of the particles is the result of data collected from several micrographs. The light grey dots visible in the micrographs are the 7-8 nm iron cores of ferritin.

of phosphate associated with the iron core on the rate of AuNP formation. Samples were prepared by reconstituting Ftn with 100 Fe/Ftn, 600 Fe/Ftn, or 1800 Fe/Ftn. The 600 Fe/Ftn and 1800 Fe/Ftn samples were divided into two fractions and one fraction of each metal concentration was incubated with phosphate to add a phosphate layer onto the iron mineral as previously reported by Treffrey *et al.*³⁵. The samples incubated with phosphate were characterized. The ratios of phosphate/Fe were 1 phosphate for every 16.5 in the 600 Fe/Ftn sample and 1 phosphate for every 19 Fe in the 1800 Fe/Ftn. The rate of AuNP formation by these samples was compared to the native horse spleen Ftn sample that contained a natural core with 1800 Fe/Ftn with 1 phosphate for every 9.5 Fe.

Each of these samples successfully formed AuNPs, however, the length of the lag phase and the steepness of the slope of the reactions differed significantly among these samples (Fig. 8). The trend showed that the smaller cores produced a much shorter lag phase and a steeper slope indicating that they formed AuNP seeds reaching 2 nm faster and that once these AuNP seeds formed, the growth of the AuNPs was faster. Our data indicate that the smaller iron cores catalyse the photochemical reaction faster and that the increased reaction rate is independent of the concentration of the protein. In addition, for Ftn samples that contained the same number of iron atoms, the presence of phosphate decreased the lag phase. Both a smaller core and the presence of phosphate are able to decrease the lag phase and increase the reaction rate (Fig. 8). For example, among the samples containing 1800 iron atoms, the reconstituted 1800 Fe/Ftn iron core with no phosphate had the longest lag phase and the native ferritin sample with 1800 Fe/Ftn that contained the most phosphate/Fe (1 phosphate for every 9.5 Fe) had the shortest lag phase. The sample reconstituted with 1800 Fe/Ftn incubated with phosphate

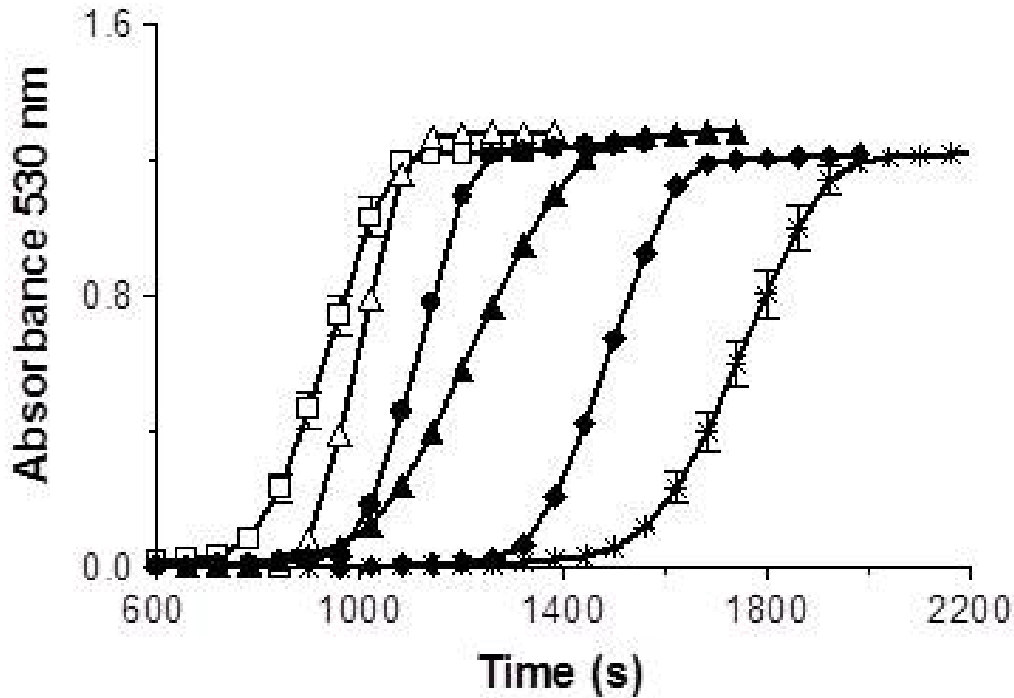


Figure 3-8. Kinetic traces of AuNP formation dependent on core size and phosphate content: a reconstituted 1800 Fe/ferritin (Ftn) sample (*), reconstituted 1800 Fe/Ftn sample containing phosphate with 1 phosphate for every 19 Fe (Ftn-P) (◆), Native Ftn sample with 1800 Fe/Ftn with 1 phosphate for every 9.5 Fe (▲), reconstituted 600 Fe/Ftn sample (●), 600 Fe/Ftn sample containing phosphate with 1 phosphate for every 16.5 Fe (Ftn-P) (Δ), reconstituted 100 Fe/Ftn sample (□). Each curve represents the means \pm the S.D. of at least two independent experiments (the error bars in the middle four curves are not visible because they are smaller than the size of the markers).

(1 phosphate for every 19 Fe) had a lag phase intermediate between the other 1800 Fe/Ftn samples. Similar results were observed for the 600 Fe/Ftn samples with and without phosphate. We propose that the phosphate coordinates the iron in the ferrihydrite core of the protein making it more reactive, probably by weakening the crystalline structure of ferrihydrite because phosphate is known to make the mineral core more amorphous⁴⁶ and/or by increasing the solubility constant (K_{sp} from 10^{-36} to 10^{-22}).

Oxidation state of the gold ions

Ensign *et al.* suggested that the reduction of Cu(II) to Cu(0) was a stepwise 1-electron at a time process³⁹. Additionally, Zhang *et al.* reported that chemical reduction of Au^{3+} to form Au(0) AuNPs on Ftn occurred through a 1-electron at a time pathway²⁶. If a similar step by step electron transfer mechanism is occurring with Au^{3+} in our photochemical system, we would predict that using Au^+ as the electron acceptor instead of Au^{3+} should result in a shorter lag phase and a more rapid production of AuNPs.

Photochemical reactions with Au^+ as the substrate occurred with a much shorter lag phase than Au^{3+} reactions to produce AuNPs, (Fig. 9A) suggesting that the 1-electron transfer observed by Ensign and Zhang occurs during the photochemical redox reaction as well. The AuNPs formed using Au^+ stopped growing at 1-3 nm diameter size (Fig. 9A–E) and are the smallest we have been able to reproducibly synthesize so far. These AuNPs are mono crystalline and spherical with a diameter size of 2.4 ± 1.0 nm (Fig. 9E). Thus, varying the oxidation state of the gold ion substrate has provided another layer of synthetic control over the desired size of the AuNPs produced by this method.

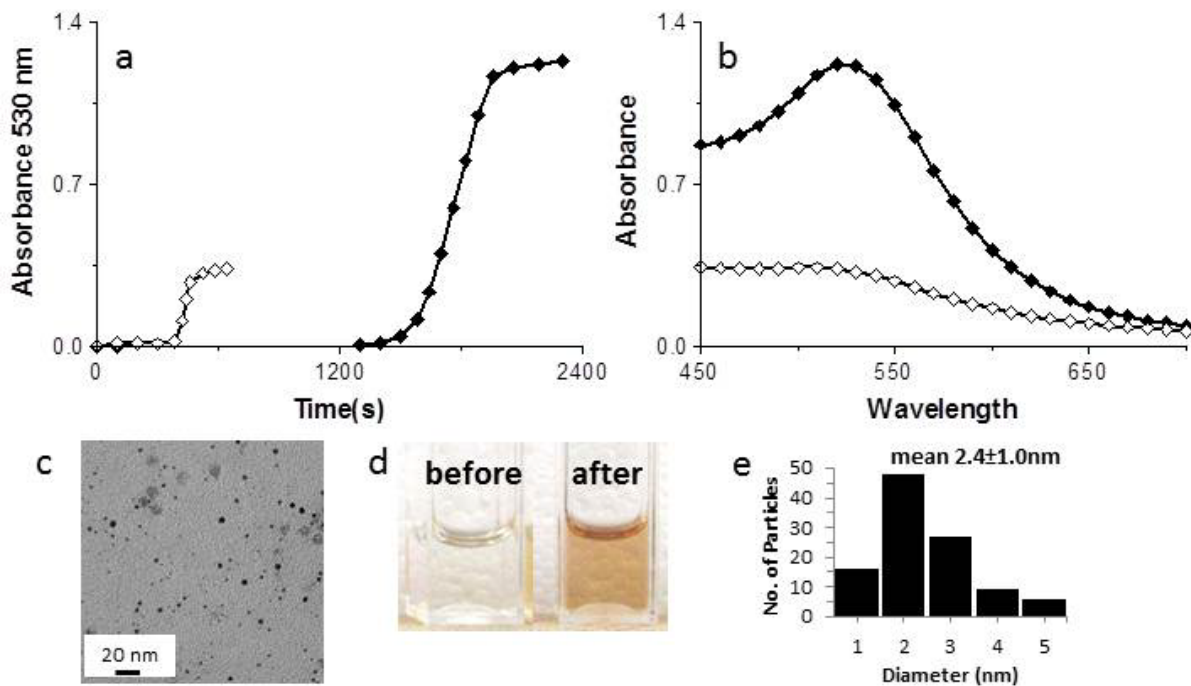
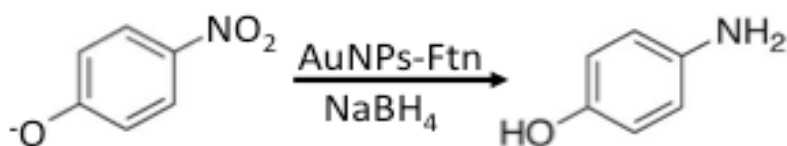


Figure 3-9. Kinetic traces (a) and absorption spectra (b) of AuNPs formation from AuCl (\diamond) vs. KAuCl₄ (\blacklozenge). (c) TEM image of AuNPs from Au⁺. (d) Cuvettes containing the AuNPs solutions before (left) and after (right) the photo reaction. (e) Histogram of the particle size distribution from the Au⁺ sample (106 particles analyzed).

All of the AuNPs smaller than 10 nm produced by our method are mono crystalline (Supplementary Fig. 3-4).

Catalytic Activity of the AuNPs

An important goal was to measure the catalytic activity of the AuNPs produced by this method. We used the reduction of 4-nitrophenol (PNP) to 4-aminophenol (PAP) with NaBH_4 as a model reaction to demonstrate the catalytic reactivity of the AuNPs produced by the Ftn photo catalytic method.



According to the literature, 2-3 nm AuNPs have the highest catalytic properties^{4, 47}. We tested AuNPs with diameters of 2.4, 7.3 and 20 nm as they catalysed the reduction of PNP in the presence of sodium borohydride (NaBH_4) to produce PAP²⁶. The rate constants for the reaction (using 10% volume Ftn-AuNPs solution as a catalyst - corresponding to 40 μM gold – or 7.9 ppm), are (linear fitting) $k = 5.34 \times 10^{-2} \text{ s}^{-1}$ for the 2.4 nm AuNPs (from Au^+), and $k = 2.91 \times 10^{-2} \text{ s}^{-1}$ for 7.3 nm AuNPs (from Au^{3+}). AuNPs with a 20 nm diameter did not catalyse the reaction within the time they were allowed to react (800 seconds, data not shown). Consistent with the literature, we observed that the smaller AuNPs were more catalytically active than the larger ones²⁶. Furthermore, PNP was not reduced by NaBH_4 in when the AuNPs were not present. These results are shown in Figure 10.

Conclusions

The synthesis and assembly of nanoparticles has become central to modern nanotechnology. Medicine, material science, energy research, catalysis, and semiconductor engineering all exploit the unique capabilities of the nanoparticles. The unique properties of nanoparticles are dependent on their size, shape, crystallinity, passivation, and biocompatibility. Synthesis methods developed so far have provided many structures that control these characteristics. Our goal was to develop a single method that could be used to synthesize a variety of sizes of AuNPs by simply altering the concentrations of the reactants.

Our work demonstrated that the Ftn-based nanoparticle photosynthesis method could be used to form a broad range of mono disperse AuNPs. Optimizing the reaction conditions allowed us to control the nanoparticle size and catalytic activity. Other than the Au ions, we utilized reagents that are already present in the human body and are therefore biocompatible by definition. Ftn-based photochemical reactions are quick, simple, and inexpensive in that it does not require complex and costly equipment (e.g.: lasers). This method will allow all laboratories to create their own nanoparticles freshly “in house” at the time they are needed. Our work demonstrates a method that allows us to reproducibly prepare biocompatible, quasi-mono disperse ~2, ~7 or ~17 nm diameter AuNPs without the need of additional separations steps. Additionally, the Ftn-citrate-capped AuNPs remain catalytically active and the catalytic activity of the desired particles correlates with the different sized AuNPs.

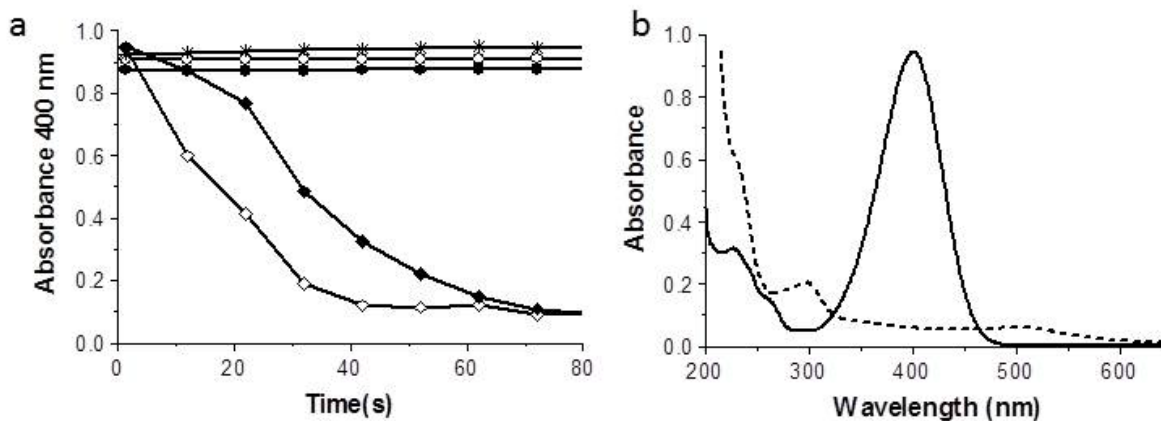
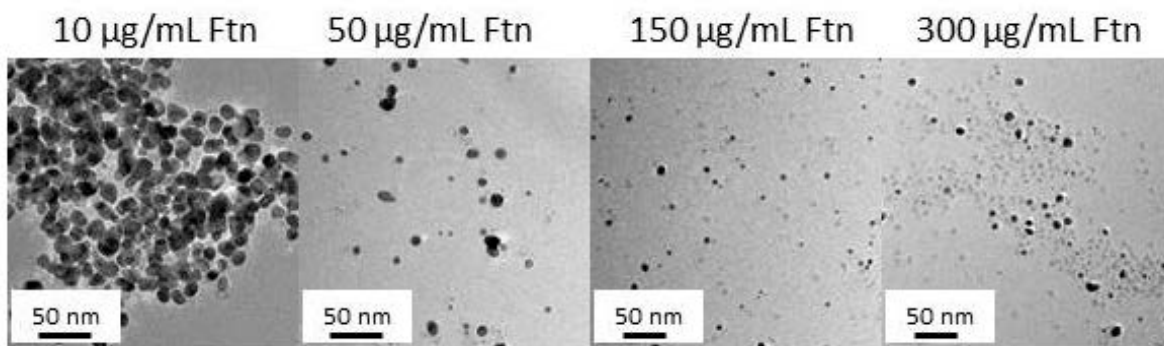
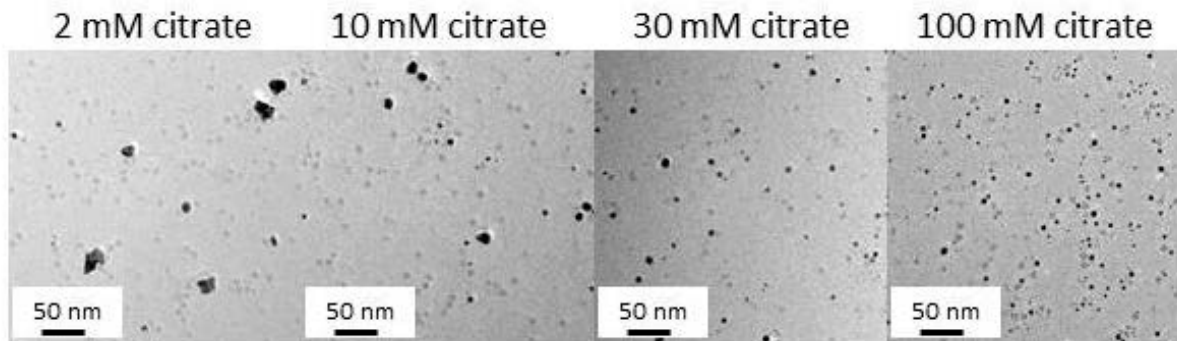


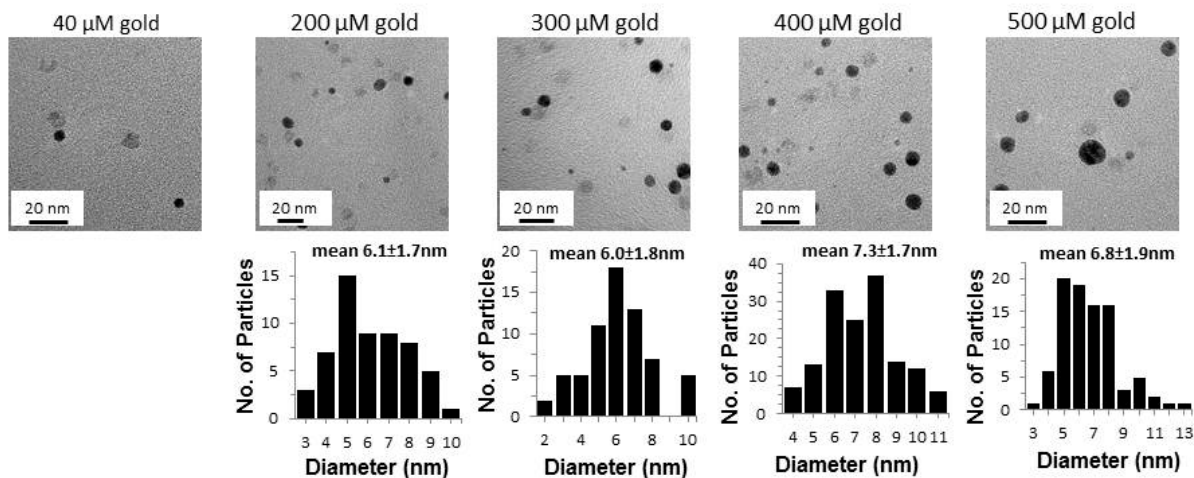
Figure 3-10. Kinetic traces (a) of the catalytic reduction of 4-nitrophenol (PNP, 50 μ M) to 4-aminophenol (PAP) by NaBH₄ (2.5 mM) in the presence of 20 nm (*), 7.3 nm (\blacklozenge), or 2.4 nm (\diamond) Ftn-AuNPs catalyst. Buffer/citrate alone (\bullet) or buffer/citrate+ferritin (\circ) reaction controls all in the presence of 2.5 mM NaBH₄. Absorption spectra (b) of 4-nitrophenol before (solid line) and after reduction (dashed line).



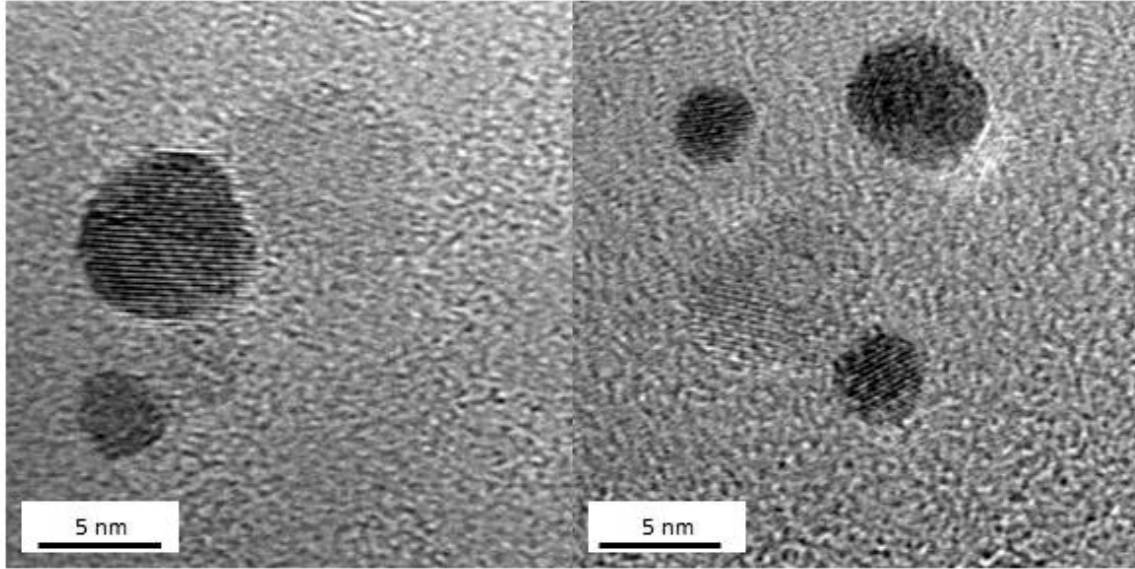
Supplementary figure 3-1. TEM images of the AuNPs at increasing concentrations of Ftn (left to right). Lower concentrations of ferritin (Ftn) form aggregates of larger particles (10 µg/mL Ftn) and few large ovoidal particles (50 µg/mL Ftn). Higher concentrations of Ftn form large numbers of small spherical or quasi-spherical particles.



Supplementary figure 3-2. TEM images of the AuNPs at increasing concentrations of citrate (left to right). Lower concentrations of citrate form few large irregularly-shaped particles. Higher concentrations of citrate form large numbers of small spherical or quasi-spherical particles.



Supplementary figure 3-3. TEM images of the AuNPs at increasing concentrations of Au^{3+} (left to right). Lower concentrations of Au^{3+} form few smaller particles. Higher concentrations of Au^{3+} form large numbers of particles with a slight increase in size. In each figure there are very dark nanoparticles (gold) and more faint nanoparticles (the iron core of ferritin). Most of the particles visible in the 40 μM gold (far left) are the Ftn iron cores (better distinguishable in figure 3-7).



Supplementary figure 3-4. Single-crystal nanoparticles. These images show two types of nanoparticles: the lighter ones are the iron cores of ferritin; the darker ones are AuNPs. The horizontal lines present on the AuNPs represent the atomic planes of the gold fcc crystal lattice.

References

1. L. Dykman and N. Khlebtsov, *Chem Soc Rev*, 2012, **41**, 2256-2282.
2. E. C. Dreaden, A. M. Alkilany, X. Huang, C. J. Murphy and M. A. El-Sayed, *Chem Soc Rev*, 2012, **41**, 2740-2779.
3. K. Saha, S. S. Agasti, C. Kim, X. Li and V. M. Rotello, *Chem Rev*, 2012, **112**, 2739-2779.
4. B. Hvolbaek, T. V. W. Janssens, B. S. Clausen, H. Falsig, C. H. Christensen and J. K. Nørskov, *Nano Today*, 2007, **2**, 14-18.
5. M.-C. Daniel and D. Astruc, *Chem Rev*, 2003, **104**, 293-346.
6. M. Grzelczak, J. Perez-Juste, P. Mulvaney and L. M. Liz-Marzan, *Chem Soc Rev*, 2008, **37**, 1783-1791.
7. I. Hussain, S. Graham, Z. Wang, B. Tan, D. C. Sherrington, S. P. Rannard, A. I. Cooper and M. Brust, *J Am Chem Soc*, 2005, **127**, 16398-16399.
8. J. T. Miller, A. J. Kropf, Y. Zha, J. R. Regalbuto, L. Delannoy, C. Louis, E. Bus and J. A. van Bokhoven, *J. Catal.*, 2006, **240**, 222-234.
9. P. C. Chen, S. C. Mwakwari and A. K. Oyelere, *Nanotechnol Sci Appl*, 2008, **1**, 67-78.
10. G. L. Prasad, in *Safety of Nanoparticles*, ed. T. J. Webster, Springer New York, Editon edn., 2009, pp. 89-109.
11. D. Prime, S. Paul, C. Pearson, M. Green and M. C. Petty, *Mater Sci Eng C Mater Biol Appl*, 2005, **25**, 33-38.
12. D. P. Stankus, S. E. Lohse, J. E. Hutchison and J. A. Nason, *Environ Sci Technol*, 2011, **45**, 3238-3244.

13. A. E. Lanterna, E. A. Coronado and A. M. Granados, *J PhysChem C*, 2012, **116**, 6520-6529.
14. L. A. McConnachie, D. Botta, C. C. White, C. S. Weldy, H. W. Wilkerson, J. Yu, R. Dills, X. Yu, W. C. Griffith, E. M. Faustman, F. M. Farin, S. E. Gill, W. C. Parks, X. Hu, X. Gao, D. L. Eaton and T. J. Kavanagh, *PLoS One*, 2013, **8**, e64165.
15. K. Yoshida, Y. Sakurai, S. Kawahara, T. Takeda, T. Ishikawa, T. Murakami and A. Yoshioka, *Int Arch Allergy Immunol*, 2008, **146**, 169-173.
16. R. Munday, E. Manns and E. A. Fowke, *Food Chem Toxicol*, 1990, **28**, 561-566.
17. X. Nie and C. Chen, *Sci China Life Sci*, 2012, **55**, 872-883.
18. N. Khlebtsov, V. Bogatyrev, L. Dykman, B. Khlebtsov, S. Staroverov, A. Shirokov, L. Matora, V. Khanadeev, T. Pylaev, N. Tsyganova and G. Terentyuk, *Theranostics*, 2013, **3**, 167-180.
19. S. Akhter, M. Z. Ahmad, F. J. Ahmad, G. Storm and R. J. Kok, *Expert Opin Drug Deliv*, 2012, **9**, 1225-1243.
20. M. Z. Ahmad, S. Akhter, Z. Rahman, M. Anwar, N. Mallik and F. J. Ahmad, *J Pharm Pharmacol*, 2013, **65**, 634-651.
21. E. C. Dreaden, L. A. Austin, M. A. Mackey and M. A. El-Sayed, *Ther Deliv*, 2012, **3**, 457-478.
22. A. Kumar, X. Zhang and X. J. Liang, *Biotechnol Adv*, 2013, **31**, 593-606.
23. R. L. Fan, S. W. Chew, V. V. Cheong and B. P. Orner, *Small*, 2010, **6**, 1483-1487.
24. C. A. Butts, J. Swift, S. G. Kang, L. Di Costanzo, D. W. Christianson, J. G. Saven and I. J. Dmochowski, *Biochemistry*, 2008, **47**, 12729-12739.

25. J. D. Keyes, R. J. Hilton, J. Farrer and R. K. Watt, *J. Nanopart. Res.*, 2011, **13**, 2563-2575.
26. L. Zhang, J. Swift, C. A. Butts, V. Yerubandi and I. J. Dmochowski, *J Inorg Biochem*, 2007, **101**, 1719-1729.
27. R. R. Crichton and J.-P. Declercq, *Biochim Biophys Acta - General Subjects*, 2010, **1800**, 706-718.
28. F. Bou-Abdallah, *Biochim Biophys Acta - General Subjects*, 2010, **1800**, 719-731.
29. R. K. Watt, *Chembiochem*, 2013, **14**, 415-419.
30. M. Brust, M. Walker, D. Bethell, D. J. Schiffrin and R. Whyman, *J Chem Soc Chem Commun*, 1994, 801-802.
31. M. Brust, J. Fink, D. Bethell, D. J. Schiffrin and C. Kiely, *J Chem Soc Chem Commun*, 1995, 1655-1656.
32. L. Li, C. J. Fang, J. C. Ryan, E. C. Niemi, J. A. Lebron, P. J. Bjorkman, H. Arase, F. M. Torti, S. V. Torti, M. C. Nakamura and W. E. Seaman, *Proc Natl Acad Sci U S A*, 2010, **107**, 3505-3510.
33. I. Kim, H. A. Hosein, D. R. Strongin and T. Douglas, *Chem. Mater.*, 2002, **14**, 4874-4879.
34. V. V. Nikandrov, C. K. Gratzel, J. E. Moser and M. Gratzel, *J Photochem Photobiol B*, 1997, **41**, 83-89.
35. A. Treffry and P. M. Harrison, *Biochem J*, 1978, **171**, 313-320.
36. O. H. Lowry, N. J. Rosebrough, A. L. Farr and R. J. Randall, *J. Biol. Chem.*, 1951, **193**, 265-275.

37. R. J. Hilton, M. C. Seare, N. D. Andros, Z. Kenealey, C. M. Orozco, M. Webb and R. K. Watt, *J Inorg Biochem*, 2012, **110**, 1-7.
38. M. M. Alvarez, J. T. Khoury, T. G. Schaaff, M. N. Shafigullin, I. Vezmar and R. L. Whetten, *J Phys Chem B*, 1997, **101**, 3706-3712.
39. D. Ensign, M. Young and T. Douglas, *Inorg. Chem.*, 2004, **43**, 3441-3446.
40. R. J. Hilton, J. D. Keyes and R. K. Watt, *SPIE Smart Structures/NDE 2010*, San Diego, CA, 2010.
41. R. J. Hilton, J. D. Keyes and R. K. Watt, *SPIE Smart Structures/NDE 2010*, San Diego, CA, 2010.
42. M. L. Marin, K. L. McGilvray and J. C. Scaiano, *J Am Chem Soc*, 2008, **130**, 16572-16584.
43. K. L. McGilvray, C. Fasciani, C. J. Bueno-Alejo, R. Schwartz-Narbonne and J. C. Scaiano, *Langmuir*, 2012, **28**, 16148-16155.
44. K. Mallick, Z. L. Wang and T. Pal, *J Photochem Photobiol A Chem*, 2001, **140**, 75-80.
45. X. Liu, M. Atwater, J. Wang and Q. Huo, *Colloids Surf B Biointerfaces*, 2007, **58**, 3-7.
46. G. Frens, *Kolloid-Z.u.Z.Polymere*, 1972, **250**, 736-741.
47. S. Guerin, B. E. Hayden, D. Pletcher, M. E. Rendall and J.-P. Suchsland, *J Comb Chem*, 2006, **8**, 679-686.

CHAPTER 4: PRECIPITATION OF MERCURY FROM AQUEOUS SOLUTIONS USING A FERRITIN PHOTOCHEMICAL REACTION

Abstract

Mercury compounds are produced by mineral smelting, other industrial processes and urban discharges and constitutes a toxic chemical that becomes incorporated into biological ecosystems. A variety of methods exist to isolate and dispose of mercury wastes. In this work we proposed a photochemical method to precipitate mercury from aqueous solutions as a method to decontaminate mercury from waste water. We proposed that illumination of a ferritin, citrate and Hg(II) mixture would photo reduce Hg(II), and precipitate it either as Hg(liq.) or in the presence of chloride ions form Hg₂Cl₂(s). The precipitate from a series of experiments was characterized by UV-Vis, ICP-OES, TEM, EDX, XPS, XRD, and GC-MS in order to characterize the precipitate(s) as well as other potential intermediates produced in the photo decontamination process. Our method effectively precipitated Hg(II) from solution and is comparable to other precipitation methods, but it uses only biodegradable reagents, does not produce additional toxic byproducts, and is applicable across a broad range of pH and salt concentrations.

Introduction

Mercury compounds have been known and used since the early days of civilization and utilized for a number of applications including dyes, medicines, and gold extraction.¹ Over this last century the toxic effects of mercury compounds have been recognized and mercury has been replaced in many instances with more benign compounds.² Unfortunately, large amounts of mercury are still produced by urban and industrial processes.³

A number of techniques for the disposal of mercury waste have been proposed and tested, but all of these have drawbacks.⁴ One major shortcoming of the existing methods is the limited concentration range of applicability: methods that are effective at high mercury concentrations are unable to remove sufficient mercury from solution to meet EPA standards, whereas techniques that effectively remove mercury at low concentrations are not applicable when high levels mercury or suspended materials are present. Another problem that accompanies the current techniques is the stringent conditions of operation: pH and salinity must be adjusted at the beginning of the treatment and then on the effluent.⁴ For example, high pH⁵ or elevated concentrations of chloride⁶ are needed by certain methods, whereas other techniques require low pH^{7 8} or low concentrations of chlorides.⁶ Furthermore, some techniques may require the addition of undesirable or relatively toxic reagents, such as sulfide, that must then be eliminated downstream.⁴ In some instances, these reagents must be added in exact ratios in order to obtain the high yield of precipitation reached using standard mercury solutions in the laboratory;⁴ however, these ratios are not always easily achieved on an industrial scale. Finally, absorbers and flocculants are required to efficiently precipitate the mercury waste but these additives increase the bulk of the waste and therefore the cost of disposal. Table 1 summarizes the pros and cons of the state-of-the-art mercury decontamination techniques.

Method	[Hg] range (ppm)	Pros	Cons	Applicability
Sulfide precipitation	1-50	-Yield: 95-99.9% ^{** 16} Inexpensive ¹⁶	-Excess S ²⁻ resolubilizes the Hg -Difficulty of real-time monitoring of [S ²⁻] -Adjustment to neutral pH (not effective at pH>9 ⁸) -Generation of toxic sulfide in the effluent -Difficulty of clarification and sludge processing -Disposal in landfills with potential resolubilization and leaching ¹⁷ -Hg recovery* -Filtration	Well-established full-scale
Coagulation/co-precipitation (aluminum sulfates, iron salts†, lime‡)	0.06 § 0.05 † 0.5 ‡	-Yield: Alum (§): 94% ^{** 8} Iron (†): 98% ^{** 8} Lime (‡): 70% ^{** 8}	-Narrow pH of operation -Sludge management -Filtration	Well-established full-scale
Adsorption on activated carbon	0.01 or 10	-Yield: 60-80% ^{**} at pH7 (higher if EDTA is added) ^{18, 19} -99.998% ^{** 19}	-pH sensitive -Sludge management -Filtration	Bench scale
Variant with CS ₂ pre-soaking and dried	10			
Xanthate absorption	10 9.5 or 100	Eff: 99.8% at pH1 ⁷ 99.99% ^{**} at pH5 ²⁰	-Requires low pH -Sludge management -0.45µm Filtration	Bench scale Pilot scale
Ion exchange	Usually low ppb but some can work up to 70 ppm (Ritter, 1992)	-Operates on demand -Less sensitive to variability -Achieves ~zero level of effluent contaminant -Is available in a variety of specific resins -Can achieve beneficial selectivity reversal upon regeneration	-Has potential chromatographic effluent peaking -Results in spent regenerant brine that must be disposed of -Can yield variable effluent quality -Cannot be used for waters with high total dissolved solids -Requires pre-filtration -Anion exchange resins require high [Chlorides] ⁶ -Cation exchange resins (Duolite GT73) require low [chlorides] ⁶ , pH~1.5, followed by 3M NaCl at pH=7 to reconstitute the column, and recovery of the re-dissolved Hg by reduction ²¹ -Low flow rate	Bench Scale Full scale
Chemical reduction (current methods) ^{8, 22, 23, 24}	High ppm	-Recovery of metallic Hg ⁸	-Effective only at high [Hg] -Requires a second-stage polishing -pH adjustment -Limited data ⁴ -Oxidation of other metals (Fe, Zn-Cu) in mesh form or use of other strong reducing agents with generation of soluble byproducts	Bench scale
Membrane separation ^{5, 6}	~1	~95% at pH11-12 ⁵	-Multiple stage process -Higher pressure of operation -pH adjustment to pH=11-12, addition of NaHS, on a low Hg feed -Limited data -Sludge management	Full scale

*From HgS+floculant vs. Hg(0) or Hg(I)-chloride proposed by our method.

**This final efficiency is achieved after filtration and/or upon addition of flocculants.

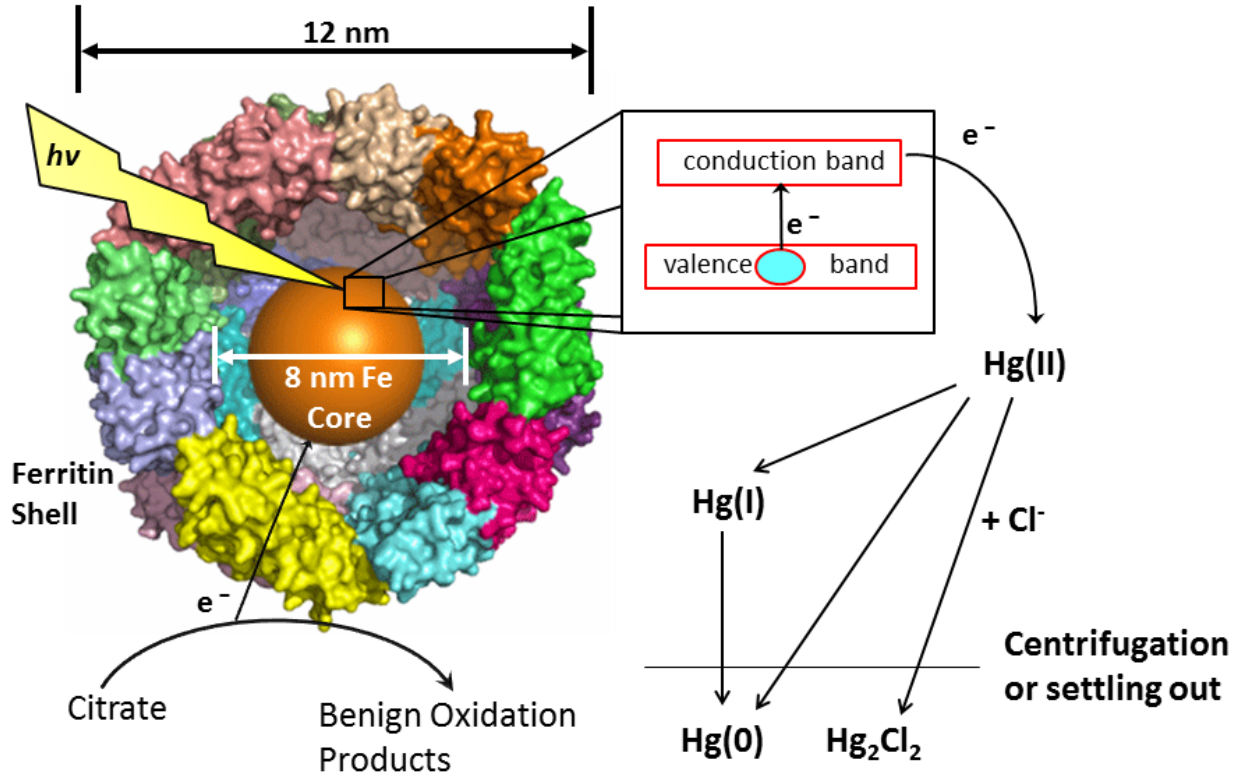
Table 4-1. Data extracted from the 1997 EPA capsule report “Aqueous Mercury Treatment”.

The method presented in this paper addresses many of these issues: the reagents used are all innocuous, the method works across a broad range of pH and salt concentrations, and the waste mass is limited to simple mercury compounds, which can be easily recycled or reutilized. Furthermore, the compounds produced have been characterized to identify the best approach to reduce the environmental and health hazards.

The core reagent used in our technique is ferritin. Ferritin is an iron storage protein present in most living organisms. The protein is assembled from 24 subunits that form a 12 nm spherical cage with an 8 nm hollow center, where iron is stored in the form of ferrihydrite (Scheme 1), Ferrihydrite is a semiconductor capable of light-induced charge separation reactions that oxidize citrate and produce electrons capable of reducing metal ions in solution (Scheme 1). Light that passes through the transparent protein shell can excite electrons from the valence band to the conduction band. Ferritin is a redox active protein and the electrons excited into the conduction band can be transferred through the ferritin protein shell to reduce Hg(II) when these ions come into close proximity with the protein external surface. The presence of a sacrificial electron donor (citrate) provides a continuous flux of electrons to the electron acceptor mercury and prevents charge build up in the iron core. Several naturally occurring carboxylic acids function as electron donors for ferritin photochemistry; among these are citrate, oxalate, tartrate, malate, and gluconate (see Chapter 2).^{9 10}

Scheme 1 shows our proposed mechanism by which ferritin could reduce Hg(II) to Hg(0) or to Hg₂Cl₂ ($K_{sp} = 1.43 \times 10^{-18}$) when chloride ions are present.

We report the ability of the ferritin photochemical method to reduce and precipitate Hg(II) from solution. We test the robustness and applicability of our method under various conditions of pH and salinity that could be present in the waste-water produced by a wide variety



Scheme 4-1. Proposed reaction mechanism. Light promotes electrons to the conduction band of ferritin semiconductor iron core. Electrons reduce Hg(II) to Hg(I) , which in the presence of Cl^- precipitates as Hg_2Cl_2 . In the absence of Cl^- Hg(II) could accept $2e^-$ and precipitate as Hg(0) .

of human activities. We characterize the products of the reaction by UV-Vis, TEM, STEM, EDX, XPS, XRD, and GC-MS; this is essential to determine the toxicity of the reaction products and to select the most appropriate method to recycle the mercury from the precipitate. Finally, we determine effectiveness of the mercury elimination by elemental analysis of the resulting aqueous solution by ICP-OES.

Materials and Methods

Native horse spleen ferritin (Ftn) was purchased from Sigma-Aldrich (Sigma F4503). The Ftn protein concentration was 39.8 mg/mL, as determined by the Lowry method.¹¹

Three concentrations of mercury were selected to test the ability of the ferritin-based photo-reduction method to reduce and precipitate mercury: 20, 200, and 2000 ppm Hg (as HgCl₂). Our laboratory has developed a protocol able to reduce a number of transition metals, as reported in other papers published by our group.^{10 12} Therefore, we used a modified version of such protocol as follows: 40 μ L 1 M TRIS-HCl pH 7.4, 60 μ L 1 M sodium citrate, 7.54 μ L Ftn (corresponding to 150 μ g/mL or 0.34 μ M), 2 μ L or 20 μ L 1 mM HgCl₂ (~20 or 200 ppm Hg), 100 μ L 1M NaCl, and deionized water to a final volume of 2 mL.

A sample containing 200 ppm Hg was prepared without NaCl to test how the ionic strength of the solution would affect the yield of the reaction (amount of Hg precipitated) and the character of the final product (e.g.: chloride, oxide, metallic mercury, and oxidation state).

The 2000 ppm Hg samples, with or without chloride, were prepared as follows: 40 μ L 1 M TRIS-HCl pH 7.4, 100 μ L 1 M sodium citrate, 5 μ L Ftn (corresponding to 200 μ g/mL), 100 μ L 100 mM HgCl₂ (~2000 ppm Hg), 50 μ L 1M NaCl, and deionized water to a final volume of 1 mL; the 2000 ppm Hg sample containing no chloride was prepared in the same way but

substituting the TRIS-HCl with TRIS-HNO₃ and the 100 μ L 100 mM HgCl₂ with 200 μ L of 50 mM Hg-acetate.

Reaction controls and optimizations were executed on 200 ppm Hg samples (2 mL total volume) and included the following conditions and reagents: 10 μ L 1 M sodium citrate (5 mM citrate); 200 μ L sodium citrate (100 mM citrate); 100 μ L 400 mM acetate buffer pH 5 (20 mM acetate); 100 μ L 400 mM phosphate buffer pH 7 (20 mM phosphate); 100 μ L 400 mM borate buffer pH 9 (20 mM borate); no Ftn control; no light control; no light control; 300 μ L 1 mg/mL BSA (150 μ g/mL); 200 μ L 6.14 mM iron oxyhydroxyde nanoparticle suspension (equivalent to the 614 μ M iron oxyhydroxyde present in 150 μ g/mL ferritin); and 12.27 μ L 100 mM Fe(III)-citrate (equivalent to the 614 μ M iron oxyhydroxyde present in 150 μ g/mL ferritin) (Fig. 9).

Each sample was exposed for 25 minutes to a full-spectrum floodlight (Integrated Dispensing Solutions, Inc.) equipped with a 400 W metal halide bulb and kept between 25-30°C for the length of the reaction.

The reaction products were characterized by UV-Vis spectroscopy (Agilent 8453), transmission electron microscopy (TEM, Tecnai F20 operating at 200 kV), scanning transmission electron microscopy (STEM, Tecnai F20 operating at 200 kV), energy dispersive X-ray spectroscopy (EDX), X-ray photoelectron spectroscopy (XPS, SSX-100 instrument Surface Sciences with an Al K α source and an hemispherical analyzer), X-ray diffraction (XRD, PANalytical X'Pert Pro diffractometer), gas chromatography-mass spectrometry (GC-MS, Trace GC ultra with ITQ 900, Thermo Scientific), and inductively coupled plasma optical emission spectroscopy (ICP-OES, Optima 2000 ICP Emission Spectrometer, Perkin Elmer).

Qualitative Analysis of Hg

UV-Vis spectrophotometry

During the initial tests, the samples were prepared in a quartz cuvette and the photochemical reactions were monitored in the 200-1100 nm range in kinetic mode with an Agilent 8453 UV/Vis spectrophotometer with a temperature controlled water-jacketed cuvette holder maintained at 25°C by a circulating water bath.

Transmission electron microscopy and energy-dispersive X-ray spectroscopy

3.5 uL of the freshly prepared samples were deposited on a copper carbon grid (300 mesh, #01813, Ted Pella Inc.) for 30 seconds, the excess suspension was wicked off the grid with filter paper, and the grid was immediately washed with 5 uL of double distilled water and dried again with filter paper. Images of the samples were collected with a Tecnai F20 set at 200 kV and the samples were further characterized by energy-dispersive X-ray spectroscopy (EDX).

X-ray photoelectron spectroscopy

Five 2000 ppm Hg samples were prepared for XPS by following the method reported in the previous section. Two samples contained 50 mM NaCl, two samples contained no NaCl, and one contained no chloride. Two samples, one with and one without NaCl, were photo reduced for 12 minutes until an orange precipitate appeared. The other three samples were kept under the light for a total of 25 minutes, when the precipitate had completely turned grey and clearly separated from the supernatant (no apparent cloudiness left). All samples were further processed as follows: each sample was centrifuged for 10 minutes at 14000 rpm, the supernatant discarded,

the pellet washed once with 0.5 mL of double distilled water, briefly vortexed, centrifuged again, and finally vacuumed dried over night at room temperature or for 40-60 min at 30°C. Then a small amount of each sample was deposited and pressed into indium foil, and placed in the XPS instrument to be characterized.

X-ray diffraction

Three 9 mL samples containing 2000 ppm mercury were prepared with NaCl, with NaCl, or without Cl⁻. In each case, the precipitates from three samples were isolated and vacuum dried for 40-60 min at 30°C. The dry precipitate was then poured onto wax paper, crushed into a finer powder with a blade, and loaded onto a zero background holder (Supplementary figure 1b). A PANalytical X'Pert Pro diffractometer equipped with a Cu X-ray source, a Ge monochromator to select the Cu K α_1 wavelength (1.5406 Å), and an X'Celerator detector was used to collect X-ray diffraction data from 10-90°2 θ with a step size of 0.016° at a scan rate of 0.007°/s. The patterns were matched with patterns for Hg₂Cl₂ (00-026-0312) and Hg(0) (04-007-2058) from the ICDD database.

Gas chromatography-Mass Spectrometry

All samples were prepared in 7 mL glass vials and tightly closed with a rubber cap. After the photo reduction, 200 μ L of the headspace gas were taken with a syringe and injected in the GC-MS set at a temperature gradient 60-120°C with a 20°C/minutes ramp, after which the temperature was held at 120°C for 2 minutes. The MS scan range was set at 100-450 amu.

Quantitative Analysis of Hg

Inductively coupled plasma optical emission spectroscopy

The photo reduced samples were transferred into 2 mL centrifuge tubes immediately after the reduction reaction and centrifuged in a bench top centrifuge for 10 minutes at 14,000 rpm. Following, the supernatants were transferred into 15 mL conical tubes. The precipitates of the 20 ppm Hg samples were dissolved in 117.6 μL of 68% nitric acid, whereas the 200 and the 2000 ppm Hg samples were dissolved in 294 μL of 68% nitric acid (calculated to produce 2% HNO_3 when the final dilution is achieved). All samples were then heated to 60°C for 10 minutes, vortexed for a few seconds to completely dissolve the precipitate, incubated in ice for 5 minutes to reduce the production of toxic fumes, and centrifuged again for 10 minutes at 14,000 rpm to eliminate any undissolved solids. The dissolved precipitate solutions were also transferred into 15 mL conical tubes. Both the original supernatants and the corresponding dissolved precipitates were diluted with double distilled water as follows with the appropriate addition of HNO_3 : the 20 ppm Hg samples to 4 mL (final 10 ppm Hg and 2% HNO_3); the 200 ppm Hg samples to 10 mL (final 20 ppm Hg and 2% HNO_3); the 2000 ppm Hg samples to 10 mL, followed by a second dilution 1:10 (final 20 ppm Hg and 2% HNO_3). A standard curve was created with 5 points in the range 0 to 40 ppm Hg using HgCl_2 in 2% HNO_3 .

Results

Previously several research groups have demonstrated that ferritin can photo chemically reduce metal ions. Based on those studies, we postulated that Hg(II) might be photo reduced to a lower valence state for removing Hg(II) from aqueous solutions. For proof of concept, samples containing Hg(II) , ferritin and citrate were exposed to light and changes in absorbance were

monitored by UV-Vis spectrometry. As expected, the illuminated sample formed a dark precipitate that was visible both by eye (Fig. 1a) and spectrophotometrically (Fig. 1b). The production of small mercury particulates increases the absorbance across the entire spectrum.

Based on these results, we designed three goals: 1) evaluate potential pathways that allow the precipitation of mercury from solution by studying reactions in the presence and absence of chloride (Scheme 1); 2) examine the mechanism(s) of photo reduction and precipitation of Hg(II) by studying the chemical intermediates that form in the reaction; and 3) based on what was learned in the previous two goals, establish conditions that maximize Hg(II) precipitation to eliminate as much Hg(II) from solution as possible.

Pathways of Hg(II) Precipitation

In order to process and analyze the samples and determine the efficiency of Hg(II) precipitated by the ferritin photo chemical method the samples were processed by the procedure outlined in Scheme 2. The aqueous phase was quantitatively analyzed for Hg(II) using ICP-OES and the precipitate was analyzed by various physical techniques to characterize the precipitate that formed by the reaction. Additionally, it was important to evaluate the presence and absence of chloride due to the insolubility of Hg(I) chloride species.

Reactions in the Absence of Chloride Ions.

The first photo reduction pathway shown in Scheme 1 evaluates the precipitation of Hg(II) by forming Hg(0) either by a one or two electron reduction. Figure 2a and 2b show the TEM and EDX results of the photo chemical reduction of a Hg(II) sample prepared in the absence of chloride. The mercury precipitate was organized in nanoparticles (or nanodroplets in

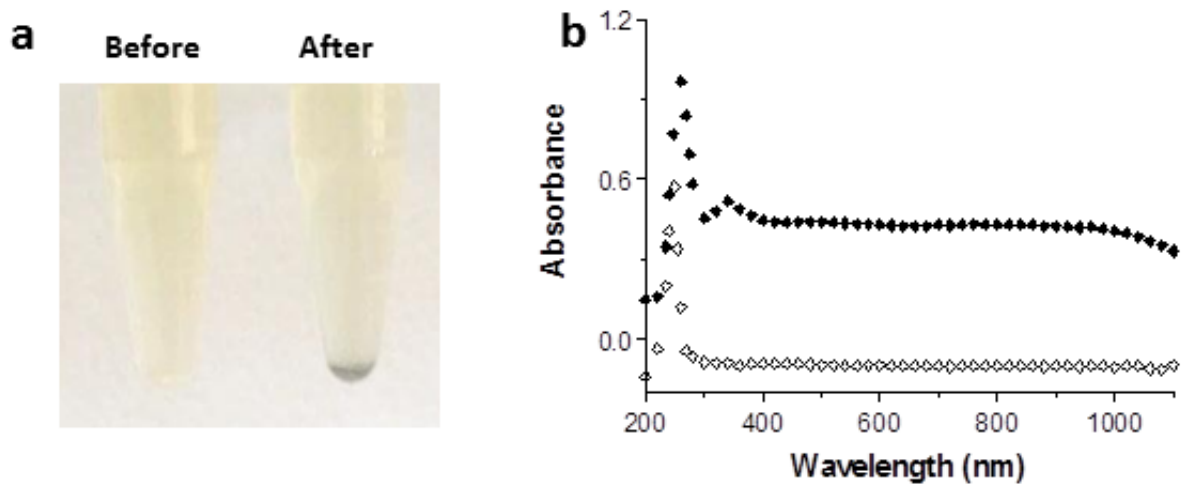
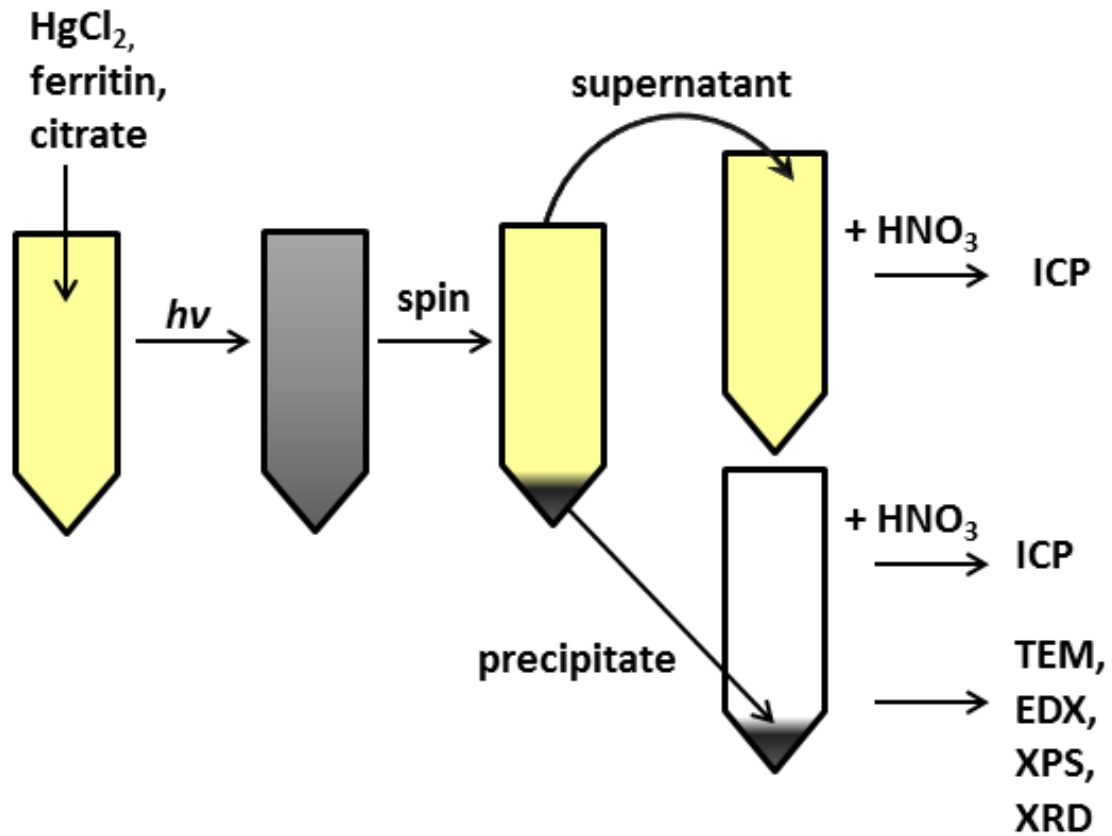


Figure 4-1. Ferritin Photo Reduction of Hg(II). (a) Samples containing mercury before illumination (left) and after illumination (right). Illumination of the ferritin-citrate-Hg(II) solution produces a mercury precipitate. (b) Absorbance spectra of the sample before illumination (◇) and after illumination (◆). The general increase in absorbance across the whole spectrum, confirms the formation of a small particulates that scatter light throughout the spectrum.



Scheme 4-2. Schematic summary of the method employed to reduce and precipitate mercury and for qualitative and quantitative analysis.

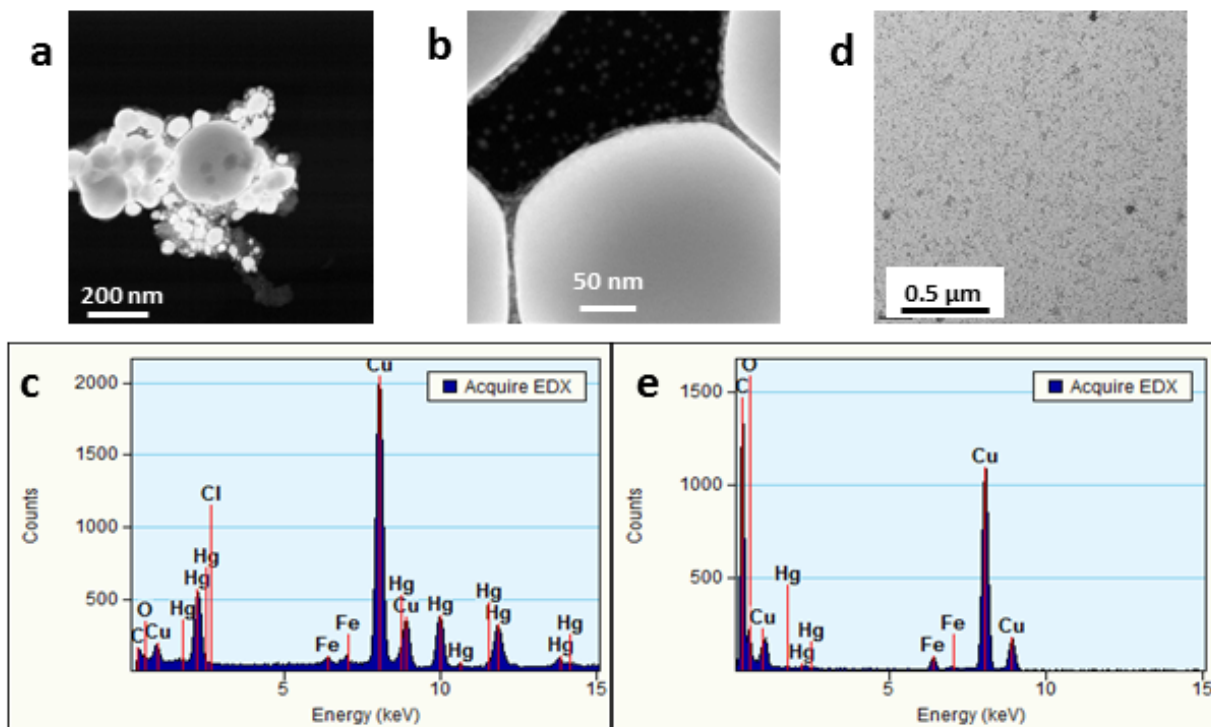


Figure 4-2. Photo chemical reduction of Hg(II) in the absence of chloride. (a) Mercury nanoparticles visualized by TEM (STEM mode); (b) an electron semi-transparent layer surrounds and passivates the nanoparticles preventing them from fusing to each other. (c) EDX showing mercury peaks, no chlorine, and minimal amounts of oxygen; the lack of counter-ion suggests that the nanoparticles in fig. 2a are metallic mercury nanoparticles. TEM (d) and EDX (e) of the area next to the mercury nanoparticles show that the Hg signal in fig. 2b is not due to background signal. The small dots visible in figure 2d are the iron cores of ferritin.

the form of Hg_{liq}) measuring about 200-500 nm in diameter (Fig. 2a). EDX analysis confirms the presence of mercury only in the nanoparticles (Fig.2a–e). Furthermore, the EDX analysis shows the absence of counter anions, like chloride or oxygen, suggests that the nanoparticles are composed of metallic mercury.

The XRD pattern of the samples produced in the absence of chloride ions (Figure 3) indicates that these precipitates are mostly amorphous and the minor peaks discernible under the broad pattern line match those of $Hg(0)$ from the database.

Reactions in the Presence of Chloride.

Figure 4 show the TEM and EDX results of the photo chemical reduction of a $Hg(II)$ sample prepared in the presence of chloride. The TEM and EDX results are comparable to those observed in the absence of chloride (Figure 2). The XRD pattern of the samples produced in the presence of chloride ions (Figure 6) indicates that these precipitates are matches those of Hg_2Cl_2 from the database. The high background signal below 30 degree theta, similar to what was observed in the absence of chloride, suggests the presence of an amorphous substance, most likely $Hg(0)$.

Studying Intermediates to Understand the Mechanism of $Hg(II)$ Photo Reduction

We noticed the formation of an orange precipitate (Supplementary fig. 1a) as the reaction proceeded towards the dark final product characterized in Fig. 2. One feasible orange mercury compound is mercury(II)-oxide. We decided to run a reaction until the orange sample formed and analyze the intermediate precipitate. Figure 5 a - f shows two nanostructures visualized at

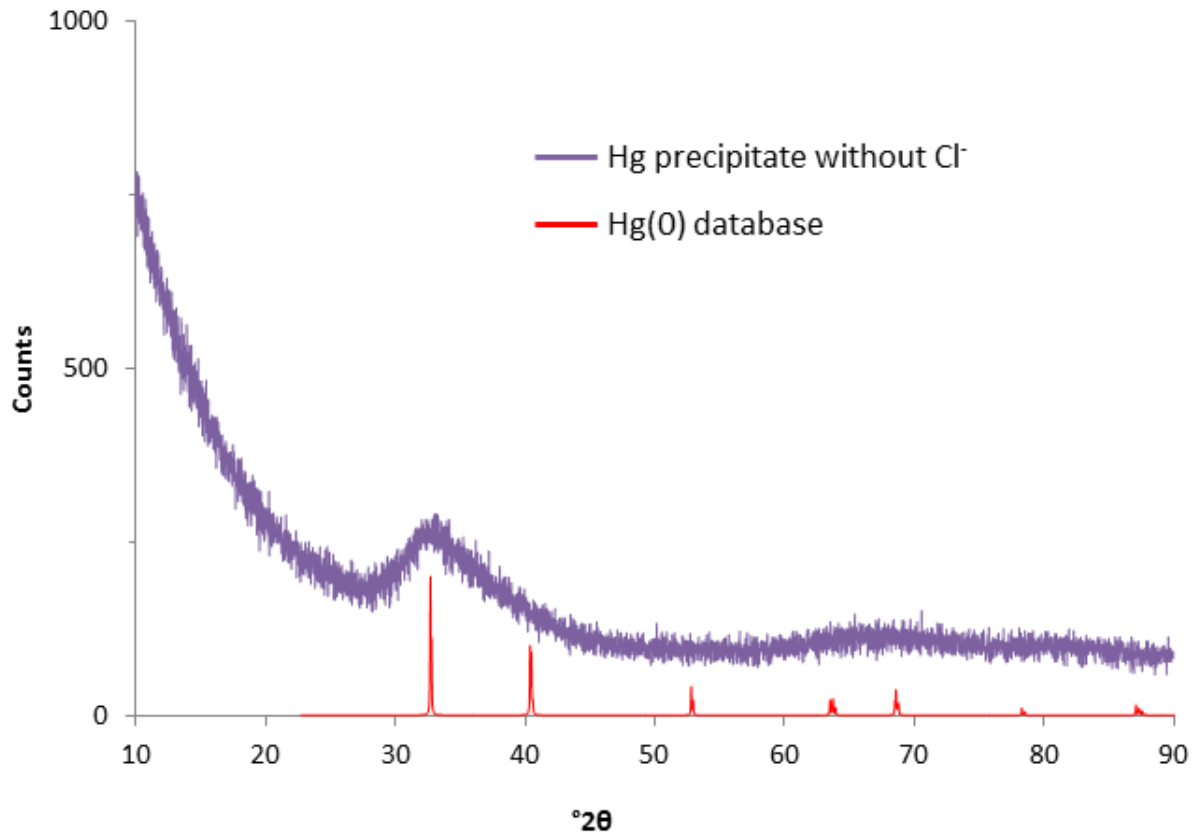


Figure 4-3. XRD diffraction pattern showing the spectrum of mercury precipitates in the absence of Cl⁻ ions (purple); the pattern matches the database for Hg(0) (red).

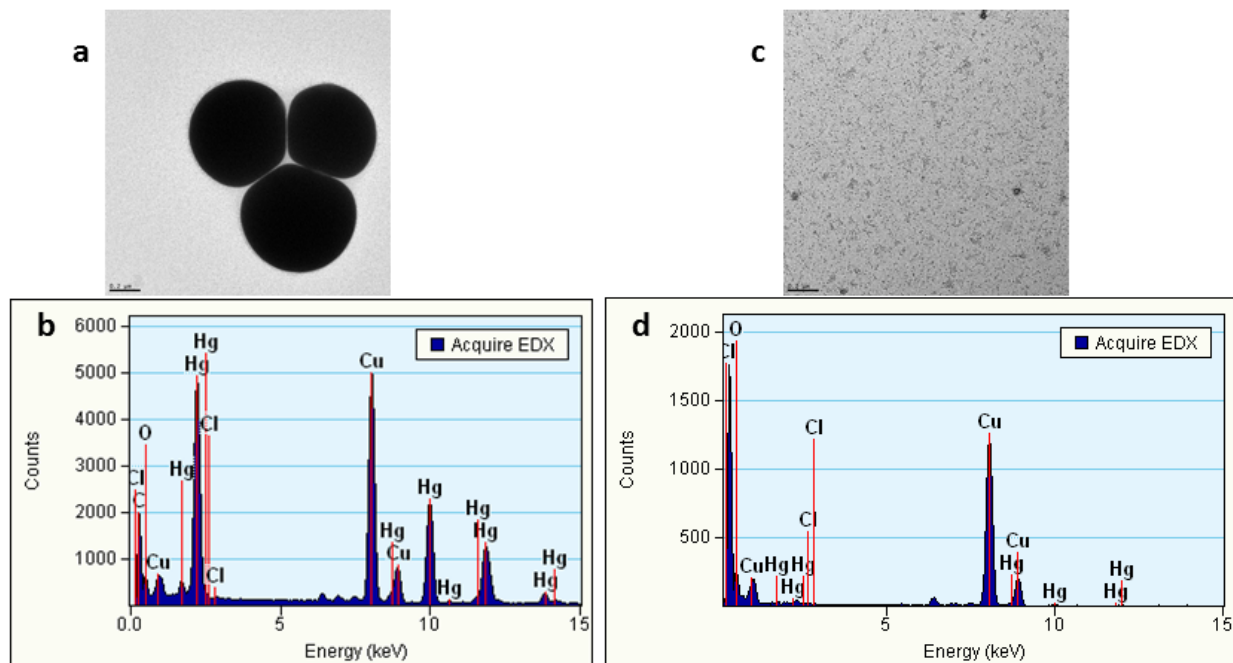


Figure 4-4. (a) TEM micrograph of mercury nanoparticles formed in the presence of chloride. (b) EDX confirming that the nanoparticles in a) are metallic mercury nanoparticles (there are no detectable amounts of chlorine or oxygen). (c) TEM micrograph taken from the area surrounding the HgNP (the small particles visible in this image are the iron cores of ferritin). (d) EDX analysis showing the absence of mercury in the area surrounding the HgNP.

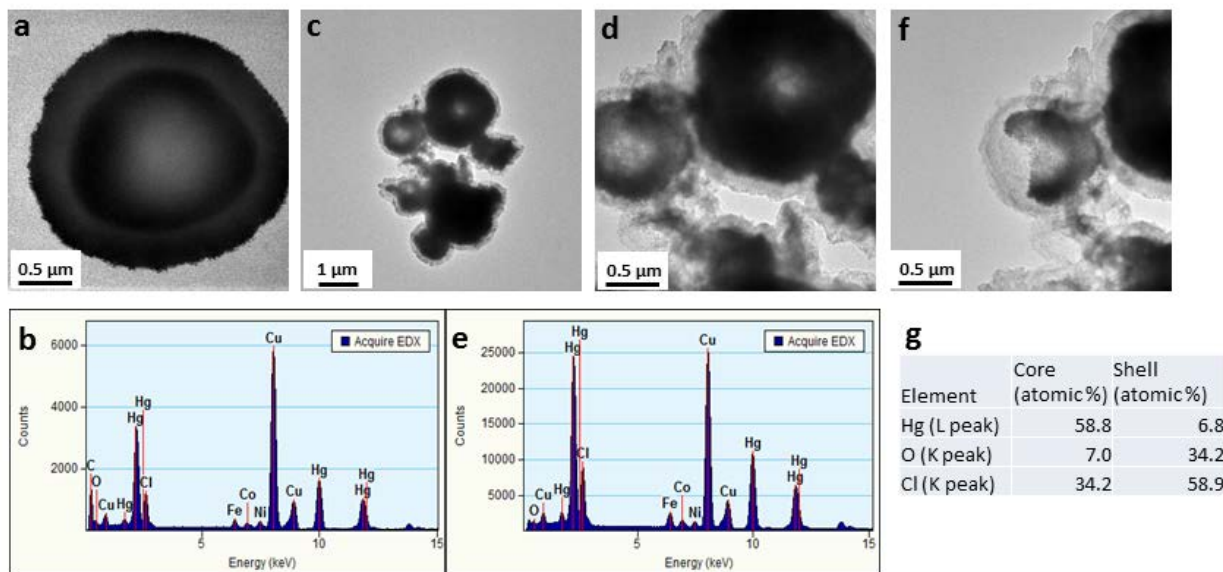


Figure 4-5. HgNP after partial reduction. (a) This figure shows a core-shell structure. The particle seems to be thinner at the center, similar to a doughnut. (b) EDX of the Hg particle in fig. 3a shows strong mercury and chlorine signals. (c-d) Cluster of doughnut-like HgNPs at two different magnifications, surrounded by an electron transparent layer and their EDX spectra (e) showing the presence of mercury and chlorine. (f) The same HgNP cluster shown in fig. 3d vaporized by the electron beam. The more volatile core started vaporizing while the shell remained intact. (g) Table showing the different composition of the core and the shell obtained by focusing the electron beam at the center of the HgNP or on the edge of the shell shows that the core is predominantly constituted of mercury, whereas the shells are more rich in oxides and chlorides. Together fig. 3f and 3g suggest that the more volatile and Hg-rich cores could contain Hg(0).

the TEM. Most structures formed after partial reduction display two common features: first, the presence of a core-shell structure; second, a doughnut-like shape denser at the edges and less dense at the center. It is unclear why the mercury precipitate should assemble in such a manner. The core-shell could evolve from a more oxidative environment outside the nanostructure, where the presence of oxygen would favor the formation of a thin layer of HgO, while the protected inner environment might allow the formation of more reduced mercury species, like Hg(I) compounds and metallic mercury. Another possibility is that the shell-structures could be due to a passivating layer created by citrate and/or ferritin. Further studies, beyond the scope of this work, are required to confirm if either one or both these situations are occurring. EDX analysis (Fig. 5b, e, g) shows that the cores are essentially composed of mercury and chlorine, whereas the shells contain mainly oxygen and chlorine, accompanied by a significant percentage of iron (Fig. 5g).

The presence or absence of NaCl did not seem to affect the size, morphology, or composition of the precipitate (data not shown).

One last piece of information produced by the TEM concerns the volatility of the two nanoparticle layers: when the TEM electron beam was focused over a particle for a prolonged period of time only the core vaporized, suggesting a higher volatility of the material composing the core compared to the shell (fig. 5f).

To obtain further clues about the composition and oxidation states of the mercury contained in the partially or completely reduced mercury precipitates, XRD was employed (fig. 6). Surprisingly, in the presence of chloride, the XRD pattern of the partially and the completely reduced samples did not differ from each other and are both consistent with the database pattern

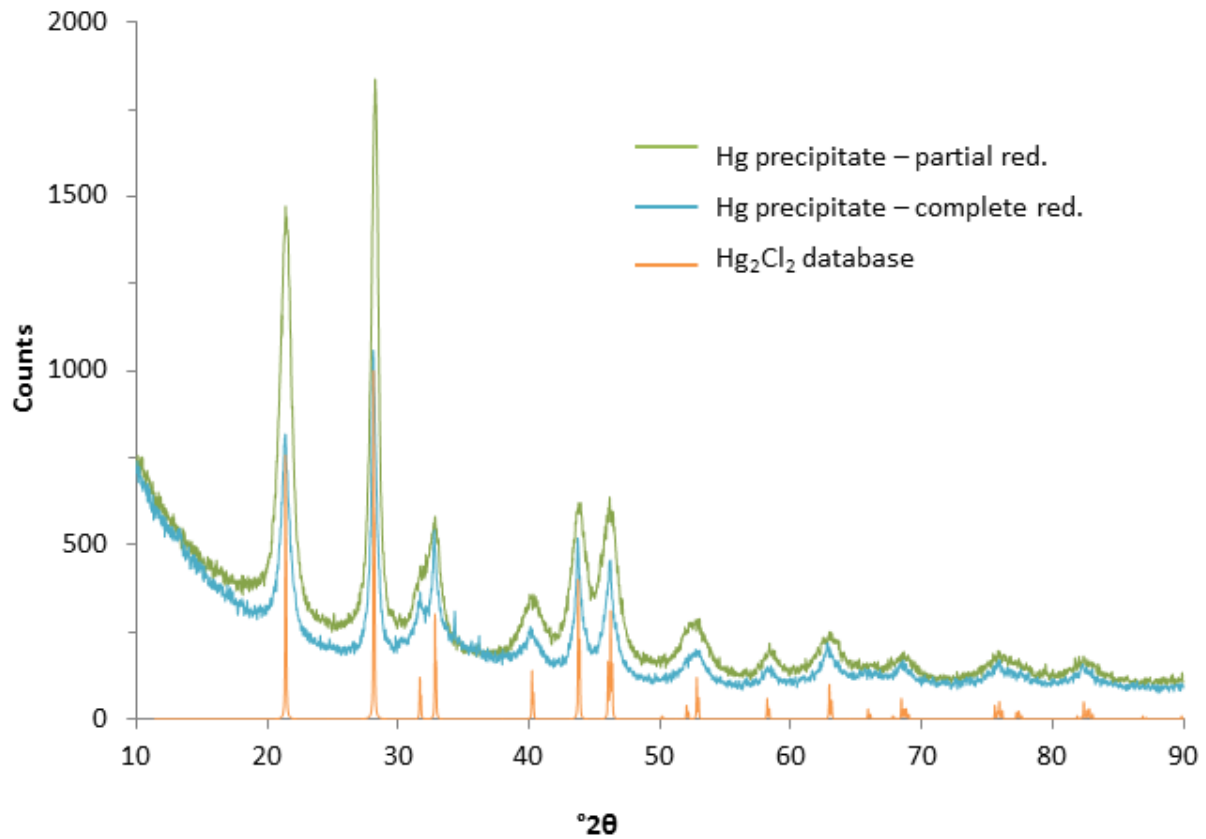


Figure 4-6. XRD diffraction pattern showing the spectrum of mercury precipitates in the presence of Cl^- ions completely (light blue) or partially reduced (green line) ; the patterns match the database for Hg_2Cl_2 (orange).

for Hg_2Cl_2 . The broad humps, more clearly visible below 30° , suggest the presence of an additional amorphous substance. Taken together the XRD and the EDX data suggest that the precipitate formed in the absence of chloride ions is mostly composed of $\text{Hg}(0)$, whereas the precipitate formed in the presence of chloride ions contains both $\text{Hg}(0)$ and Hg_2Cl_2 .

The XRD pattern of the precipitate formed in the presence of NaCl completely overlapped that of the samples not containing NaCl (data not shown), showing that the presence of additional Cl^- ions, beside those provided by the HgCl_2 reagent, does not influence the quality of the reaction products.

Organomercury Compounds

At this point it was important to find out whether during the speciation of the mercury organomercury compounds were also created; among those, volatile, highly toxic species like methylmercury and ethylmercury were our first targets. GC-MS results (Fig. 7) shows that no methylmercury, dimethylmercury, or methylethylmercury were formed during the photochemical reduction of $\text{Hg}(\text{II})$. On the other hand low levels of elemental mercury were detected.

Our partial conclusion from our qualitative analysis confirms the accuracy of our model mechanism for mercury photo-reduction and precipitation in that the $\text{Hg}(\text{II})$ ions were reduced and precipitated as $\text{Hg}(0)$ in the absence of chloride. In the presence of chloride the predominant product was still $\text{Hg}(0)$ but a small amount of Hg_2Cl_2 was also formed. Furthermore, no organomercury compounds were created in the process.

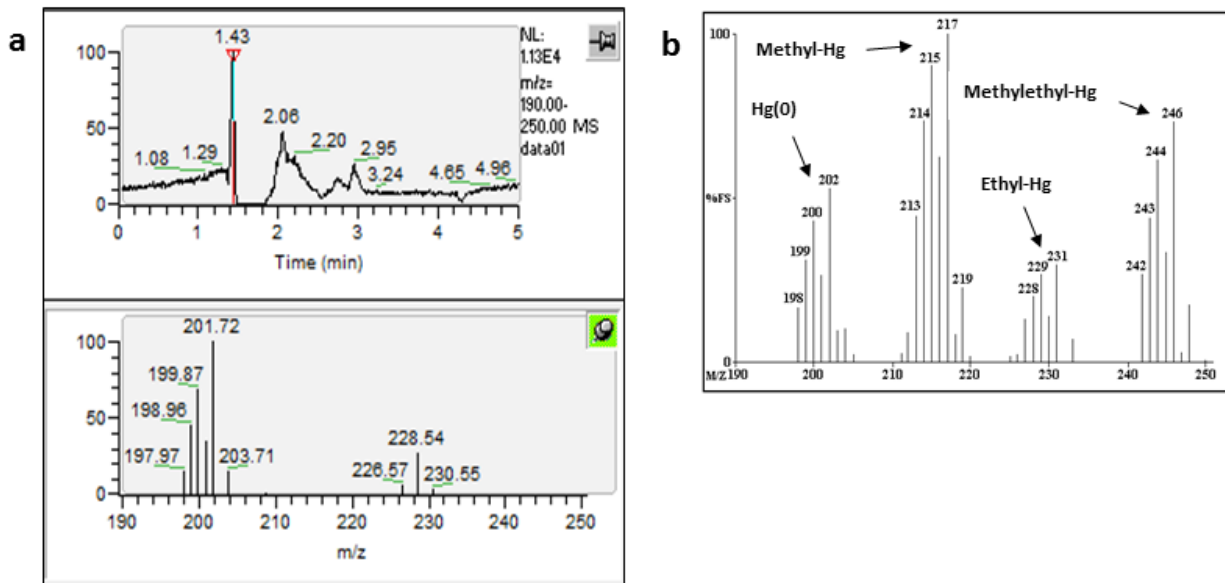


Figure 4-7. (a) GC-MS analysis detected elemental mercury but no organo-mercury. (b) Reference spectrum for the most common volatile organo-mercury compounds. No organomercury compounds were detected.

Quantitative Analysis on the Photo Catalysis Methods for Hg(II) Precipitation.

An important purpose of this work was to evaluate how efficiently this photo chemical Hg(II) process precipitated Hg(II) from solution. For this purpose, ICP-OES analysis was performed on the precipitate and the supernatant of the samples isolated after the photo-reduction reaction. Figure 8 shows that we successfully eliminated between 79% and 95% from 20 parts per million (ppm) and 200 ppm mercury solutions, respectively.

Stability of Ferritin as a Photo Catalyst

We observed that in the 2000 ppm sample that only 87% of the Hg(II) was precipitated but that in the 200 ppm sample we precipitated 95% of the Hg(II) (Fig. 8). We hypothesized that the lower yield of the reaction at higher concentrations of Hg(II) could be due to limiting concentrations of the reducing agent (citrate). To test this theory we removed the mercury precipitate from a 2000 ppm sample by centrifugation and added more citrate and buffer to the supernatant, without adding more ferritin. Figure 9 shows that the addition of more citrate (additional sacrificial electron donor) helped precipitate more Hg(II) from the solution. Furthermore, it suggests that ferritin was still active after prolonged exposure to light. This is consistent with previous research that demonstrated that ferritin undergoes minimal damage after multiple photoreaction cycles¹³. About this topic, Kim *et al.* stated “Thus, there is only a small degradation of the catalyst, even after many catalytic turnovers. The protein stabilization of the semiconductor catalyst in the ferritin system may represent a significant advantage for future photocatalytic applications, such as in environmental remediation chemistry.”¹⁴

We wanted to test the stability of ferritin in our mercury photo-reduction system. For this purpose, a 2 mL sample containing 200 µg/mL (0.45 µM) of ferritin, 100 mM citrate, and 2000

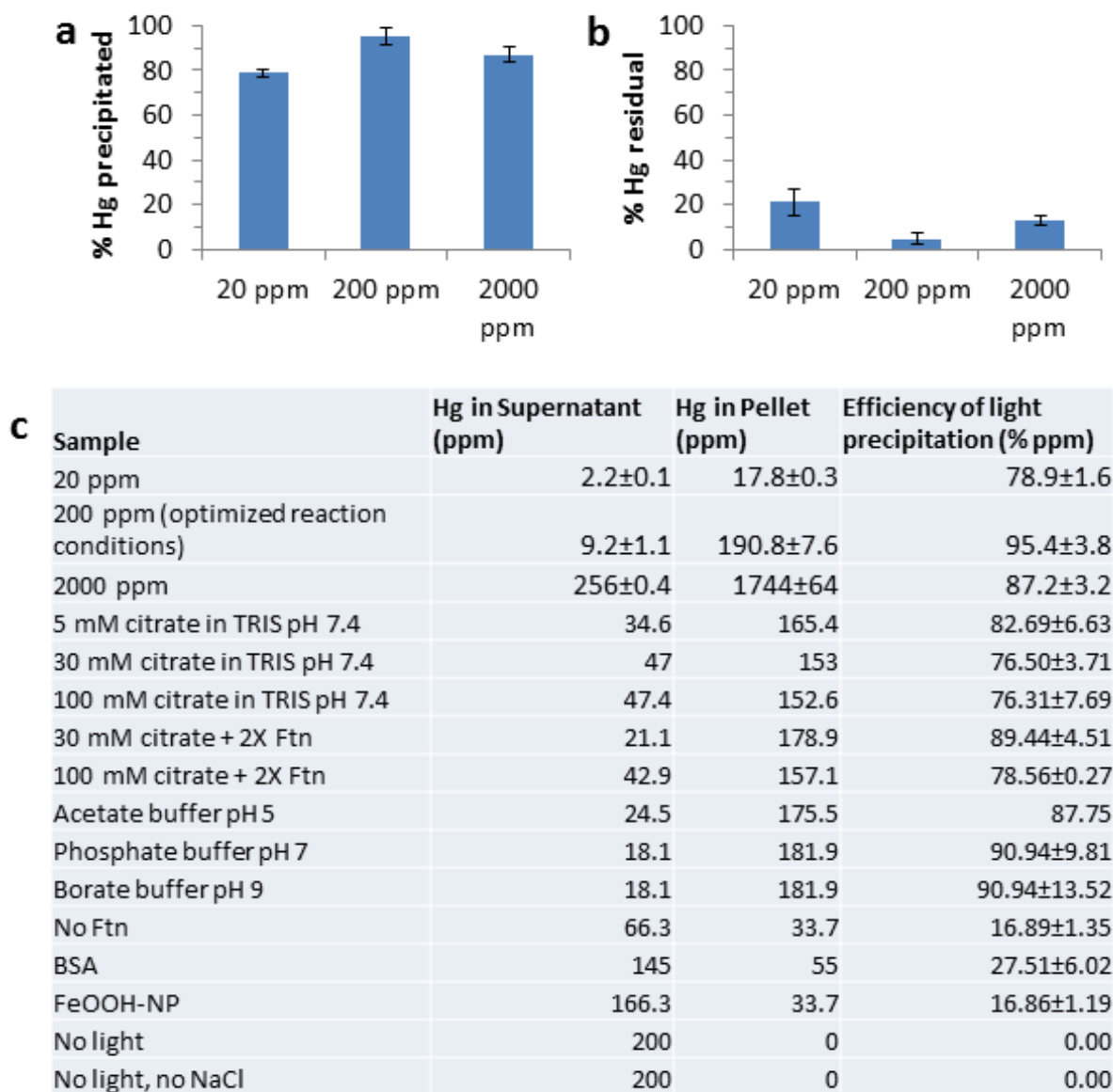


Figure 4-8. ICP quantification of the mercury precipitated (a) and residual mercury in solution (b) at various initial concentrations of the contaminant (20-2000 ppm Hg²⁺). The bars represent the means of 3 experiments, each run at least in duplicates, ± the SD. (c) Table reporting the numerical values of the graphs shown in a) and b) and controls.

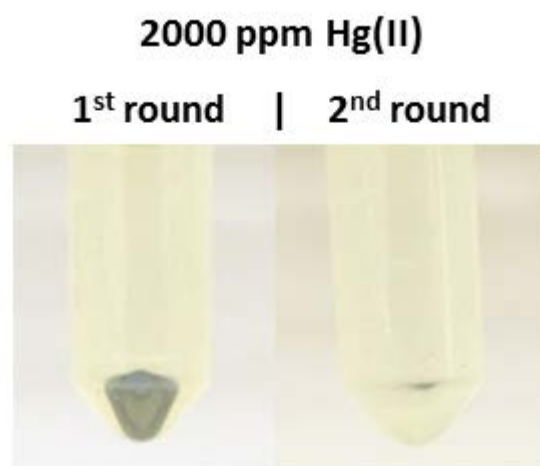


Figure 4-9. Precipitates formed after a first (left tube) and a second round (right tube) of photo-reduction of the same starting sample. At higher concentrations of mercury, the limiting electron donor reduces the yield of the reaction. After removing the first mercury precipitate, the addition of more citrate and further exposure to light allowed the abatement of more mercury from the solution, thus increasing the overall reaction yield.

ppm HgCl_2 (10 mM) was irradiated for five photo-reduction cycles. At the end of each cycle the precipitate was removed by centrifugation, after which 100 mM citrate together with 2000 ppm HgCl_2 were added again to the supernatant, and the sample was irradiated again. The amount of mercury precipitated did not vary across five photo-reduction cycles, thus demonstrating that ferritin worked as a true catalyst, not being consumed during the reaction (Figure 10). By the end of the fifth cycle each ferritin has catalyzed the transfer of 110,000-220,000 electrons, depending if mercury is reduced to Hg(I) or Hg(II) , without significant loss of activity.

At this point we wanted to demonstrate that the precipitation of mercury was dependent on ferritin. We, therefore, ran a series of control experiments by substituting ferritin with bovine serum albumin (BSA), FeOOH nanoparticles (FeOOH-NP), or Fe(III)-citrate , to respectively mimic the protein, the FeOOH semiconducting core of ferritin, or the Fe(III)-citrate formed upon the reduction, diffusion, re-oxidation, and chelation of the iron from the core of ferritin.

Also, we tested the robustness of the method under various conditions, by changing the concentrations of citrate and/or ferritin, or the pH (Fig. 8 and Fig. 11). Our results show that there is not statistical difference in the elimination of mercury in the pH range 5-9, or using 5-100 mM citrate with 0.34-0.68 μM ferritin. Our controls show that BSA was somewhat able to catalyze the reduction of mercury (with 3-fold less efficiency); similarly, using no ferritin or substituting ferritin with FeOOH-NP also produced a mercury precipitate but the yield was reduced by 5-fold in both cases. Fe(III)-citrate seemed to have an inhibitory effect on the reaction. Also, no reaction occurred in the absence of light. Taken together these data show that ferritin is essential for an effective photo-catalytic removal of mercury from contaminated water.

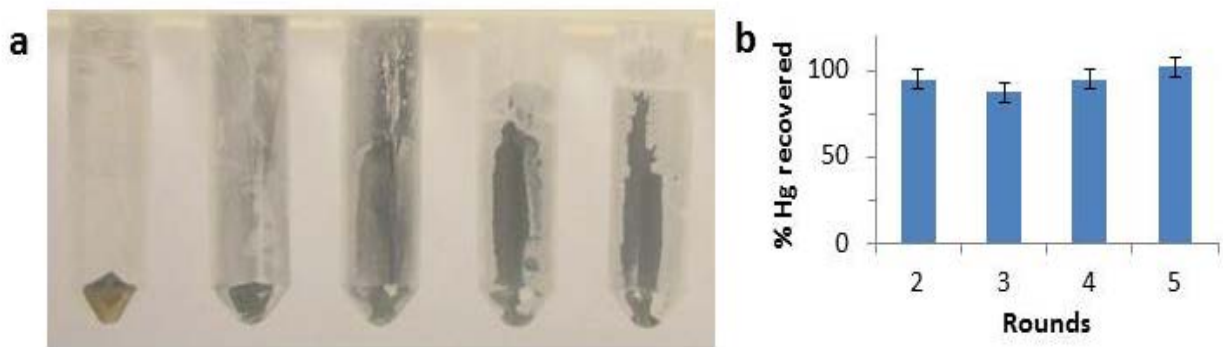


Figure 4-10. Photo-catalytic properties of ferritin. (a) Precipitates formed after six rounds photo-reduction (left to right). After each round, the precipitate was removed and the same equivalents of citrate and mercury used at the beginning were added again. (b) Mercury recovery as a percentage of the yield of the first round precipitation. No significant changes in the reaction yield were observed, correlating with minimal loss ferritin catalytic activity after five rounds.

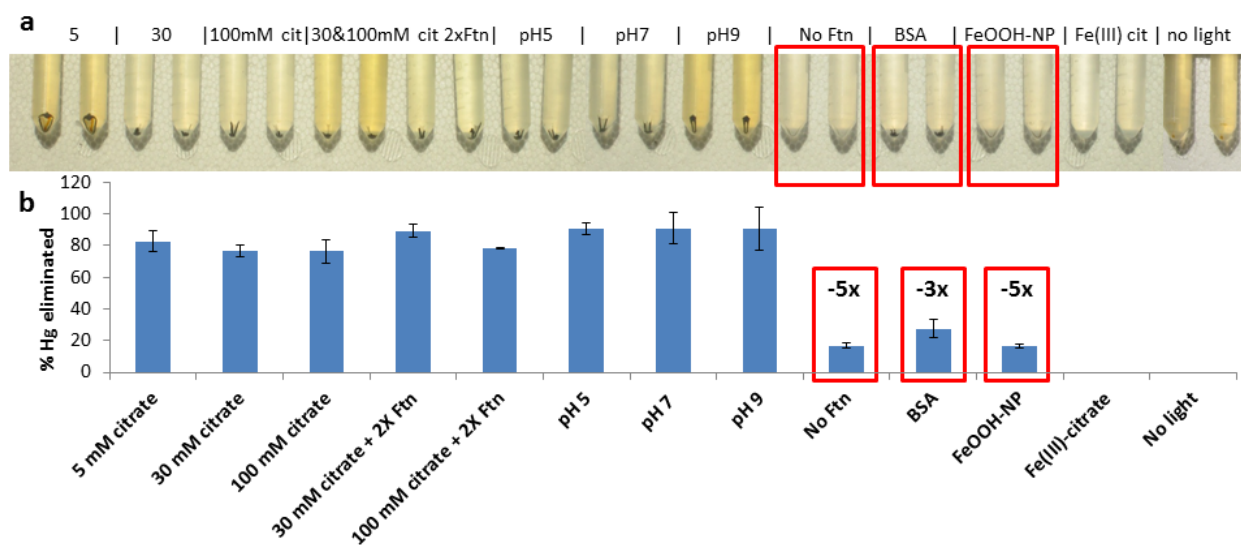
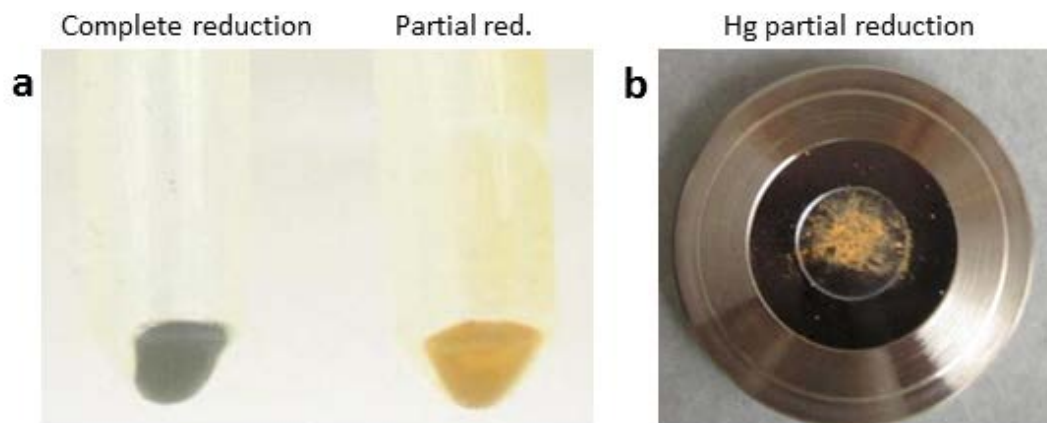


Figure 4-11. Test of the robustness of the method in various conditions and experimental controls. (a) Tubes containing the reaction solution before (last two tubes on the far right) and after the photoreaction. A mercury precipitate is visible in all tubes other than those not exposed to light or in the presence of Fe(III)-citrate (last four tubes and two columns on the right). (b) ICP quantification of the mercury precipitates. No significant change in mercury decontamination efficiency was observed in all of the conditions tested when ferritin was present (first eight columns of the graph). The absence of ferritin reduced by 5 fold the efficiency of the reaction and FeOOH nanoparticles were unable to recapitulate function in the photo-decontamination process (left and right red boxes). BSA performed the best among the controls but its ability to decontaminate the solution from mercury is about 3 fold lower than that of ferritin (middle red box). Fe(III)-citrate seem to have an inhibitory effect over the photo-chemical reduction of mercury. The results are the means of an experiment performed in triplicates.

Conclusions

We hypothesized that the ferritin photochemical method previously used to reduce Cu(II) and Au(III) to elemental nanoparticles could be effective in reducing and precipitating Hg(II) from a contaminated solution. Consistent with this hypothesis, we were able to precipitate up to 95% of the Hg(II) from water solutions and eliminate it by simple centrifugation or settling out. Both ferritin and light were essential to maximize the efficiency of the process. According to our proposed model, mercury precipitated as Hg(0) or Hg₂Cl₂, although other forms of amorphous mercury compounds cannot be ruled out. Importantly, no volatile organomercury compounds were formed during the photocatalysis. Our results, together with the work performed by Ensign *et al.* and Kim *et al.*,^{15 14} suggest that ferritin works as a true catalyst, not being consumed during the reaction. The mercury precipitate byproduct was organized in nanoparticles or “nanodroplets”. These nanostructures could find an application in material sciences. The efficiency of this technique across a broad pH range, with or without salt, and the catalytic nature of ferritin make this method potentially applicable for the remediation of waste waters or water bodies contaminated by high to medium-low concentrations of soluble ionic mercury.



Supplementary figure 4-1. (a) Sample precipitates after complete (left) and partial reduction (right). (b) The partially reduced sample was dehydrated and pulverized and placed on an XRD plate.

References

1. S. Wei, Q. Ma and M. Schreiner, *Journal of Archaeological Science*, 2012, **39**, 1628-1633.
2. A. Rubo, Kellens, R., Reddy, J., Steier, N. & Hasenpusch, W., 2000.
3. Q. Wang, D. Kim, D. D. Dionysiou, G. A. Sorial and D. Timberlake, *Environmental pollution (Barking, Essex : 1987)*, 2004, **131**, 323-336.
4. J. Patterson, *EPA/625/R-97/004*, 1997.
5. G. P. e. a. Broom, *J. Membrane Sci.*, 1994, 219-230.
6. T. J. Sorg, *J. AWWA*, 1979, **71**, 454-456.
7. L. Campanella, *Water Res.*, 1986, **20**, 63-65.
8. J. W. Patterson, *Wastewater Treatment Technology, 2nd ed. Ann Arbor, MI: Ann Arbor Science.*, 1985.
9. V. V. Nikandrov, C. K. Gratzel, J. E. Moser and M. Gratzel, *J Photochem Photobiol B*, 1997, **41**, 83-89.
10. J. D. Keyes, R. J. Hilton, J. Farrer and R. K. Watt, *J. Nanopart. Res.*, 2011, **13**, 2563-2575.
11. O. H. Lowry, N. J. Rosebrough, A. L. Farr and R. J. Randall, *J. Biol. Chem.*, 1951, **193**, 265-275.
12. O. D. Petrucci, D. C. Buck, J. K. Farrer and R. K. Watt, *RSC Advances*, 2014, **4**, 3472-3481.
13. D. Ensign, M. Young and T. Douglas, *Inorg. Chem.*, 2004, **43**, 3441-3446.
14. I. Kim, H. A. Hosein, D. R. Strongin and T. Douglas, *Chem. Mater.*, 2002, **14**, 4874-4879.

15. D. Ensign, M. Young and T. Douglas, *Inorg. Chem.*, 2004, **43**, 3441.
16. R. Perry, *EPA/660/2-74/086*, 1974.
17. C. L. a. D. K. S. Hansen, *EPA/600/R-92/105. pp. 121-125*, 1992.
18. L. Thiem, D. Badorek, and J.T. O'Connor, *J. AWWA*, 1976, 447-451.
19. M. J. J. Humenick, M. Asce, and J.L. Schnoor, 1974.
20. G. Tiravanti, *Patterson, J.W. and R. Passino, eds. Metals Speciation, Separation, and Recovery. Lewis Publishers. , 1987, 665-686.*
21. N. S. C. a. R. J. E. Becker, *Reactive polymers* 1993, 5-14.
22. J. P. Gould, *J. WPCF* 1984, **56**, 280-286.
23. J. M. a. J. B. Grau, *J. Chem. Tech. Biotechnol. , 1995, 1530158.*
24. A. a. L. O. Sites, *New Jersey Department of Environmental Protection and Energy*, 1992.

CHAPTER 5: A FERRITIN PHOTOCHEMICAL SYNTHESIS OF MONODISPERSED SILVER NANOPARTICLES THAT POSSESS ANTIMICROBIAL PROPERTIES

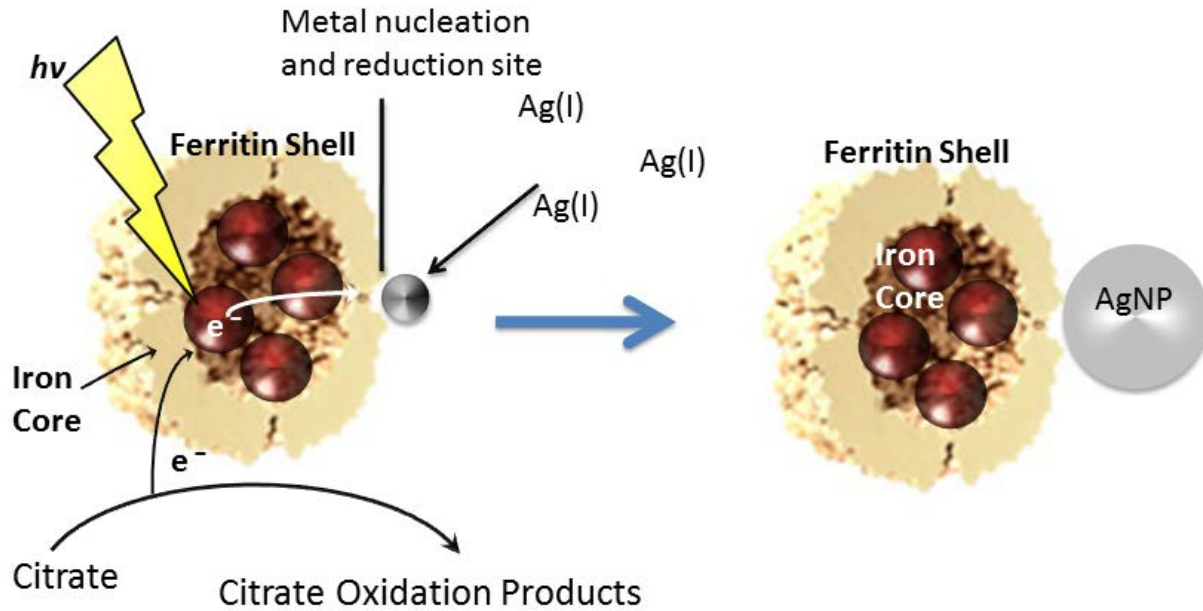
Abstract

We previously reported that ferritin acts as a photo catalyst to form monodispersed gold nanoparticles (Chapter 3). Because silver possesses a favorable reduction potential (+0.80 V), we postulated that the ferritin photochemical method should be able to reduce Ag(I) to Ag(0), and similar to gold, the reduced silver should nucleate and form silver nanoparticles (AgNPs) on the external surface of ferritin. This study reports that Ag(I) can function as an electron acceptor to form monodispersed AgNPs using the ferritin photo catalytic method. The formation and growth of the AgNPs was monitored by following the appearance and growth of the surface plasmon resonance (SPR) peak at 420 nm by spectrophotometry. The resulting monodispersed AgNPs were analyzed by transmission electron microscopy (TEM), scanning transmission electron microscopy (STEM), and energy dispersive X-ray spectroscopy (EDX). Gel filtration demonstrated that the AgNPs co-migrated with ferritin through the column suggesting a strong association with ferritin. AgNPs are known to possess antimicrobial properties. The antimicrobial properties of Ferritin-AgNPs were compared to commercially available AgNPs by testing growth inhibition of *Staphylococcus aureus*. Commercially available AgNPs inhibited bacterial growth at 5 ppm AgNPs and Ferritin-AgNPs inhibited growth at 20 ppm Ferritin-AgNPs.

Introduction

Ferritin is a large spherical protein measuring 12 nm in diameter with an 8 nm hollow interior occupied by a ferrihydrite core (FeOOH) that possesses semiconductor properties.^{1, 2} This protein, with or without its iron cargo, has been used as a scaffold for forming metal nanoparticles on both the inside and outside by a variety of techniques.^{3 4} Early research focused on depositing metal oxides on the interior of ferritin as a size-constrained reactor to form nanoparticles with a tight size distribution by replacing iron with other metals (see table 1-1 in chapter 1).² Later studies produced elemental forms of the metals inside ferritin by using powerful reducing agents.^{5, 6 7} Ferritin has also been used as a scaffold for the formation of metals nanoparticles on the external surface of ferritin.^{3 4 8}

Recently a photochemical method has been described where ferritin is used as a charge separation catalyst to oxidize organic acids and channel the liberated electrons to reduce metal ions in solution (Cr(VI), Cu(II) and Au(III)).^{9, 10 4, 8, 11} This photochemical reaction is represented in Scheme 1 and the goal of this work was to determine if this system could reduce Ag(I) to silver nanoparticles (AgNPs). The ferritin photo catalyst functions because light can excite electrons from the valence band into the conduction band of the ferrihydrite semiconductor allowing ferritin to act as a charge separation catalyst.⁹ The excited electrons are donated to the target ions on the ferritin exterior surface through the redox active protein shell of ferritin.¹² To replenish the electron holes created by the charge separation event, ferritin is able to oxidize sacrificial electron donors present in solution. Typically citrate or oxalate is used as the electron donors in these reactions. The ferritin protein shell possesses additional advantages for photochemical reactions. Ferritin makes the semiconductor soluble facilitating reactions in



Scheme 5-1. Ferritin containing an iron mineral absorbs light and transfers the excited electrons to Ag(I) ions bound to the nucleation sites on the exterior of the ferritin protein shell. This process oxidizes citrate to replenish the holes and continue the electron flow for further reactions. Continued light exposure allows the AgNPs to grow to larger sizes.

aqueous solutions. Additionally, ferritin possesses negatively charged 3-fold channels that funnel positive ions into ferritin and act as nucleation sites on the exterior of ferritin for metal nanoparticle synthesis to occur.^{8 13 14}

Nanoparticles have a variety of applications due to their unique properties that set them apart from the bulk material, atomic element, or ion.¹⁵ Nanosilver or AgNPs have antimicrobial properties so they have been deposited on the surfaces of medical devices and in consumer products as disinfectants.^{16, 17} In this work we desired to synthesize AgNPs using the ferritin photochemical method and test the efficacy of the resulting AgNPs for antimicrobial properties.

This work describes the successful photoreduction of silver ions to form silver nanoparticles (AgNPs) on the surface of ferritin, using the ferritin photo catalytic reaction system. The AgNP samples were characterized by UV-Visible spectrophotometry, transmission electron microscopy (TEM), scanning transmission electron microscopy (STEM), and energy dispersive X-ray spectroscopy (EDX). Size exclusion chromatography was used to confirm that the AgNPs are attached to the external surface of the ferritin protein. Finally we report that Ferritin-AgNPs possess antimicrobial activity against *Staphylococcus aureus*.

Materials and Methods

We obtained the native horse spleen ferritin (Ftn) and silver chloride from Sigma-Aldrich. Ferritin protein concentrations were determined by the Lowry method.¹⁸ The iron content of the native ferritin was 1800 Fe/Ftn as determined by the dithionite/bypyridyl method (Watt et al. 1992). The silver nanoparticles (AgNPs) were formed in a solution containing Ftn (150 µg/mL) with TRIS buffer at pH 7.4 (20 mM), sodium citrate (30 mM), AgNO₃ (800 µM) and NaCl (50 mM). The temperature of the samples during illumination was maintained at 25°C

using a water-jacketed cuvette holder connected to a temperature-controlled water bath in an Agilent 8453 UV-Vis spectrophotometer. 1 mL samples were placed in a quartz cuvette and exposed to a full spectrum Hg-halide floodlight (Integrated Dispensing Solutions, Inc.) and the reaction progression was monitored in the 200-1100 nm range in kinetic mode for the length of the reaction in a UV-Vis spectrophotometer (Agilent 8453). AgNPs were formed and monitored at 420 nm during an 800 seconds irradiation time. The appearance and size of the NPs was evaluated and visualized by transmission electron microscopy (TEM) performed on a Tecnai F30 operating at 300 kV, and by scanning electron microscopy (STEM) and Energy-dispersive X-ray spectroscopy (EDX) on a Tecnai F20 operating at 200 kV. Size exclusion chromatography was performed with a Superdex 200 10/300 GL column (GE Healthcare Life Sciences, cat.17-5175-01) by injecting 0.5 mL of freshly prepared AgNPs or 0.5 mL of 150 µg/mL Ftn. Control reactions were conducted in the dark or without ferritin.

Bacterial Growth Minimal Inhibitory Concentration Test

Fifteen 12 x 75 mm tubes were prepared by adding 1 mL of tryptic soy broth (TSB) containing 1×10^6 colony forming units (CFU) of *Staphylococcus aureus* (ATCC 6538). Then 1 mL of a solution containing Ferritin-AgNPs (at 80, 40, 20, 10, 5, 2.5, or 1.25, 0.625 ppm silver) or commercial AgNPs (American Biotech Labs, at 10, 5, 2.5, or 1.25, 0.625 ppm) was added to eight or five of the tubes, respectively. The two remaining tubes, one containing only 2 mL of TSB and one containing 2 mL of TSB plus 1×10^6 CFU of *S. aureus*, were used as experimental controls. The experiment was performed in triplicates.

Results

The photo catalytic formation of the AgNPs was monitored by following the change in absorbance at 420 nm which corresponds to the surface plasmon resonance band of AgNPs (Fig. 1A and B).¹⁹ A visible color change from colorless to amber, characteristic of silver nanoparticles in aqueous solution was observed and provides further evidence supporting the conclusion that AgNPs were successfully synthesized by this method (Fig. 1C). Control reactions conducted in the dark, as well as in the light but without ferritin, were not able to produce AgNPs.

After illumination the samples were placed on TEM grids and analyzed by TEM and STEM. Two populations of particles were observed, very dense particles and diffuse particles (Fig. 2A). We hypothesized that the darker particles were AgNPs and that the lighter particles were the iron core of ferritin. The increased atomic density of AgNPs gives a better contrast than the iron cores of ferritin (Fig. 2A). Analysis of these particles by STEM using the elemental analysis capability of EDX confirmed the diffuse particles were iron and the dense particles were silver (Fig. 3). The size of the AgNPs is uniform with diameters of 4.92 ± 1.17 nm (Fig. 2B; calculated from 126 AgNPs).

To determine if the AgNPs were attached to or possessed a strong association with ferritin, the sample was passed over a gel filtration column to determine if the AgNPs could be separated from ferritin. The AgNPs co-elute with ferritin, but earlier than a control of native ferritin alone (Fig. 4). These data suggest that the majority of the AgNPs remain attached to the external surface of the ferritin protein shell, thus achieving a larger radius as a complex and eluting faster than the ferritin alone.

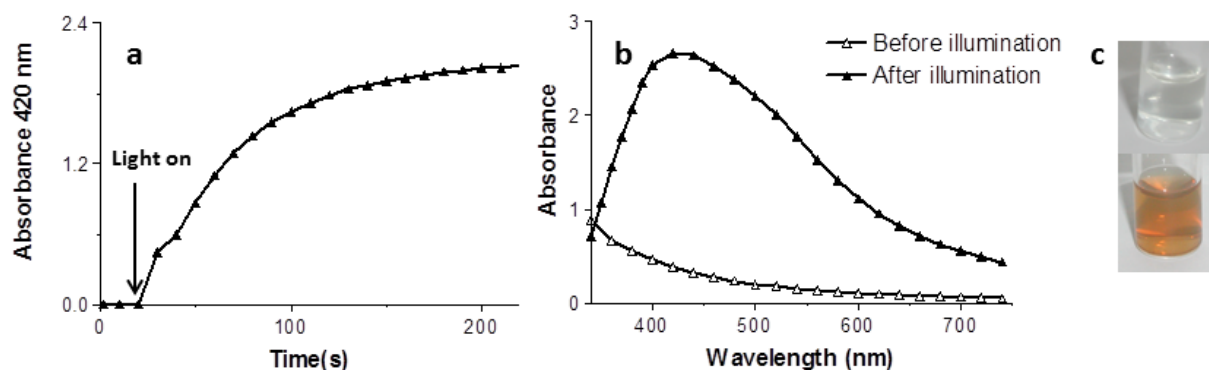


Figure 5-1. The synthesis of AgNPs using the ferritin photochemical system. Kinetic trace (a) of AgNPs formation and spectra (b) of the samples before (Δ) and after (\blacktriangle) illumination. Upon illumination, the absorbance increases at 420 nm due to the formation of AgNPs. This absorbance is due to the surface plasmon resonance properties of AgNPs. (c) The color of the solution changes from almost colorless before (top) to amber after (bottom) illumination.

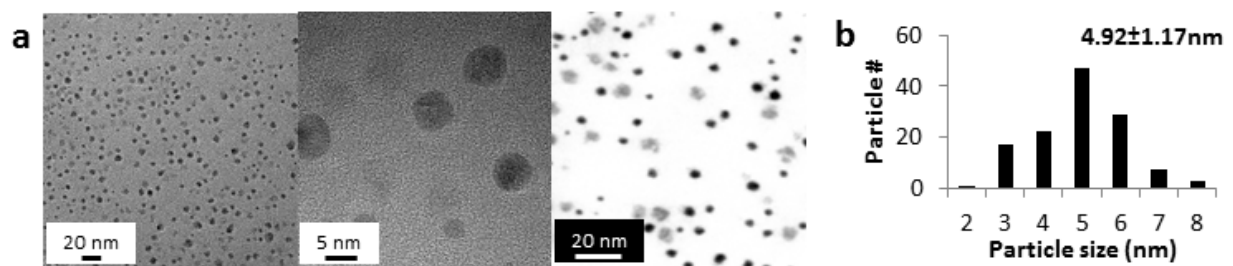


Figure 5-2. TEM and STEM of AgNPs. (a) TEM micrographs at lower magnification (left) and higher magnification (center); STEM image in negative mode (right). These images clearly show the presence of two types of particles: the less dense iron cores of ferritin and the more dense AgNPs. (b) Size distribution of the AgNPs \pm S.D.(126 AgNPs analyzed).

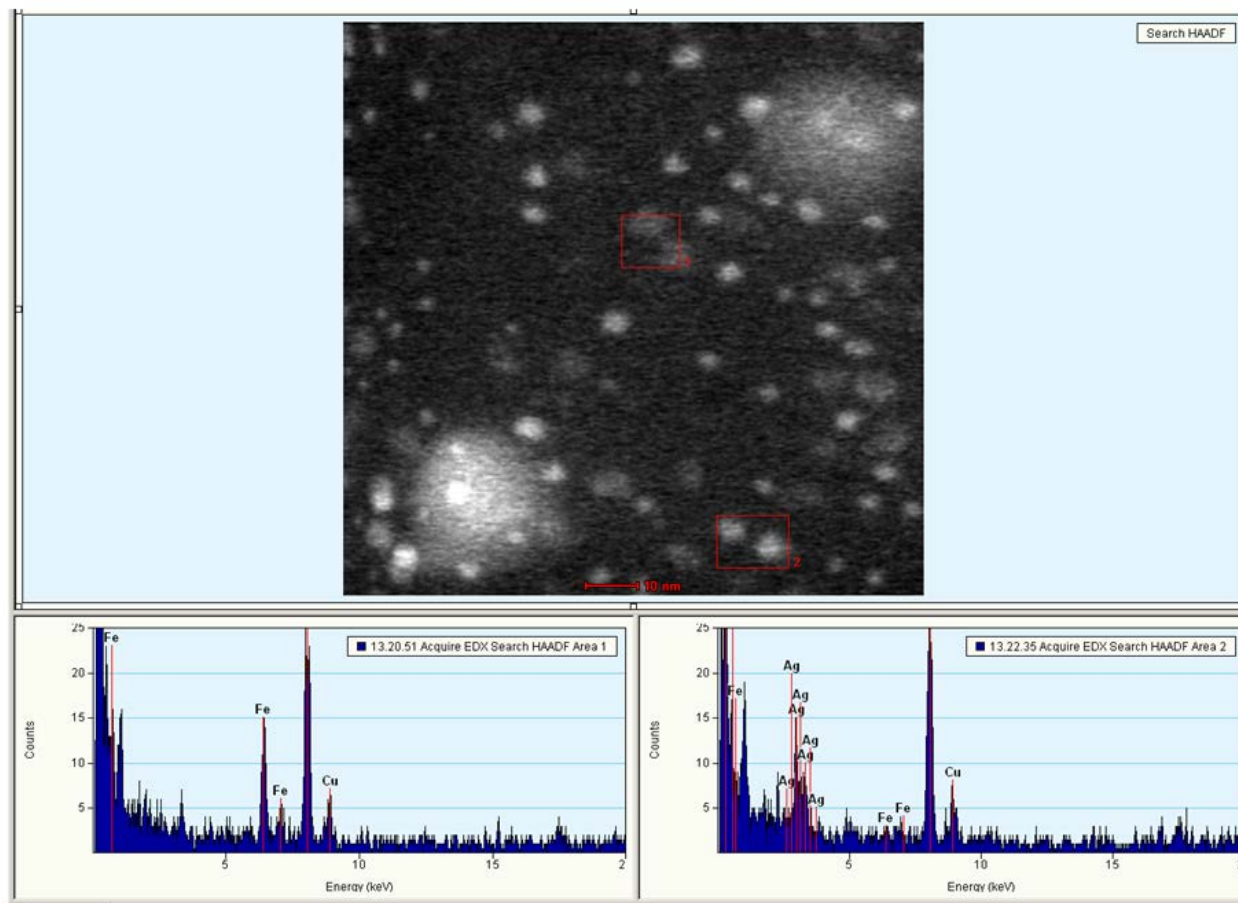


Figure 5-3. STEM and EDX Elemental Analysis of Nanoparticles. STEM image (top) and EDX patterns (bottom). EDX confirms that the less dense particles in area 1 are the iron cores of ferritin (bottom left) and the more dense particles are AgNPs (bottom right).

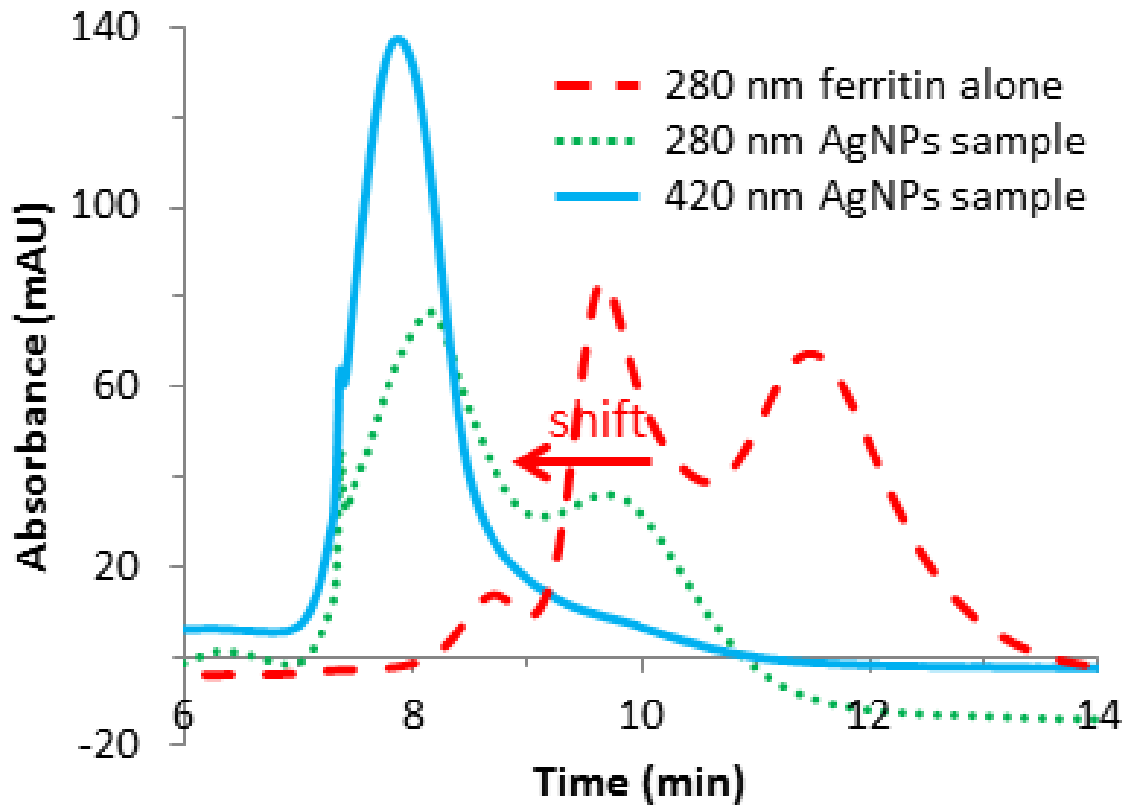


Figure 5-4. Size exclusion chromatography of the ferritin AgNP solution. A standard of native ferritin was passed over the column and the elution profile was monitored at 280 nm. Ferritin runs as a dimer and monomer so it has two peaks. A sample of ferritin and AgNPs was passed over the column and the absorbance was monitored at 280 nm (detecting the protein) and 420 nm (detecting the AgNP plasmon resonance). The AgNPs (420 nm peak, continuous line) and the ferritin (280 nm peak, dotted line) in the sample both co-elute before the ferritin standard (dashed line), showing that the particles are attached to the external surface of the protein shell.

AgNPs are known for their potent antimicrobial properties; ^{20, 21} for this reason we decided to run a minimal inhibitory concentration test on *Staphylococcus aureus* (in collaboration with the Savage group) to test whether the AgNPs that were associated with ferritin retained antimicrobial activity. For an experimental positive control for AgNP antimicrobial activity we used a commercially available 10 ppm water solution of AgNPs of the same size as those produced by the ferritin photochemical method. Figure 5 shows that the Ftn-AgNPs inhibit growth at 20 parts per million. In contrast, commercial AgNPs inhibit at 5 parts per million. These results were consistent in all three triplicate samples. Although the Ferritin AgNPs are effective at inhibiting the growth of *S. aureus* they are about 4-fold less effective. It is possible that the interaction with ferritin blocks some of the surface of the AgNPs and prevents some of the available surface area for inhibiting the bacterial growth. The tubes containing bacteria without antimicrobial agents or no bacteria showed growth or no growth, respectively.

Conclusions

The purpose of this research was two-fold: 1) to test whether our ferritin photo catalytic method could form AgNPs; and 2) to determine if ferritin AgNPs possessed antimicrobial properties even if part of the AgNP surface was passivated by ferritin. This work demonstrates that AgNPs were successfully synthesized, that the AgNPs remained associated on the surface of ferritin and that the resulting Ftn-AgNP solution possesses potent antimicrobial activity at low parts per million concentration range. Furthermore, the AgNPs produced by the ferritin photochemical method are small and monodispersed, characteristics required by a number of applications. ¹⁵

Finally, we suggest that due to the absence of harsh reagents and surfactants, and the presence of ferritin, our AgNPs solution, alone or in a formulation, could find use in medicine as a mild topical disinfectant. In fact, the combined antimicrobial and iron-sequestering abilities (iron is an essential nutrient for all microorganisms^{22 23}) of the AgNPs and ferritin, respectively, might represent an effective combined treatment to prevent the growth of human pathogens. Unfortunately, testing this theory is beyond the scope of the current chapter.

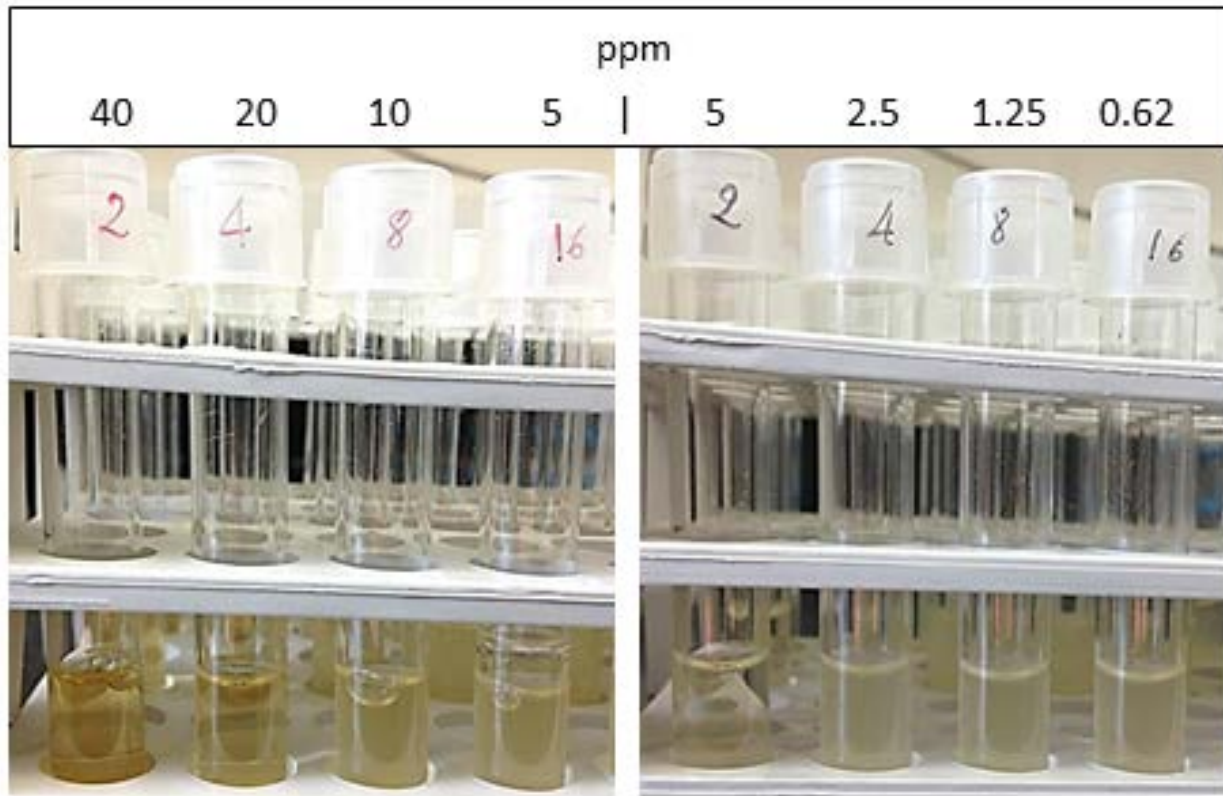


Figure 5-5. AgNP minimal inhibitory concentration. The broth in the tubes where the bacterial growth was inhibited look clear (instead of turbid). The dilution factor is reported on the tube caps and the corresponding concentration above the pictures. The ferritin-AgNPs (left image) and control commercial AgNPs (right image) inhibit bacterial growth at 20 ppm and 5 ppm, respectively. The test was executed in triplicates.

References

1. R. R. Crichton and J.-P. Declercq, *Biochimica et Biophysica Acta (BBA) - General Subjects*, 2010, **1800**, 706-718.
2. R. K. Watt, O. D. Petrucci and T. Smith, *Catalysis Science & Technology*, 2013, **3**, 3103-3110.
3. L. Zhang, J. Swift, C. A. Butts, V. Yerubandi and I. J. Dmochowski, *J Inorg Biochem*, 2007, **101**, 1719-1729.
4. J. D. Keyes, R. J. Hilton, J. Farrer and R. K. Watt, *J. Nanopart. Res.*, 2011, **13**, 2563-2575.
5. C. A. Butts, J. Swift, S. G. Kang, L. Di Costanzo, D. W. Christianson, J. G. Saven and I. J. Dmochowski, *Biochemistry*, 2008, **47**, 12729-12739.
6. I. Yamashita, K. Iwahori and S. Kumagai, *Biochimica et Biophysica Acta (BBA) - General Subjects*, 2010, **1800**, 846-857.
7. M. Uchida, S. Kang, C. Reichhardt, K. Harlen and T. Douglas, *Biochimica et Biophysica Acta (BBA) - General Subjects*, 2010, **1800**, 834-845.
8. O. D. Petrucci, D. C. Buck, J. Farrer and R. K. Watt, *RSC Advances*, 2013.
9. V. V. Nikandrov, C. K. Gratzel, J. E. Moser and M. Gratzel, *J Photochem Photobiol B*, 1997, **41**, 83-89.
10. D. Ensign, M. Young and T. Douglas, *Inorg. Chem.*, 2004, **43**, 3441-3446.
11. I. Kim, H. A. Hosein, D. R. Strongin and T. Douglas, *Chem. Mater.*, 2002, **14**, 4874-4879.
12. R. K. Watt, R. B. Frankel and G. D. Watt, *Biochemistry*, 1992, **31**, 9673-9679.
13. T. Douglas and D. R. Ripoll, *Protein Sci*, 1998, **7**, 1083-1091.

14. T. Takahashi and S. Kuyucak, *Biophys J*, 2003, **84**, 2256-2263.
15. K. M. M. Abou El-Nour, A. a. Eftaiha, A. Al-Warthan and R. A. A. Ammar, *Arabian Journal of Chemistry*, 2010, **3**, 135-140.
16. T. Faunce and A. Watal, *Nanomedicine*, 2010, **5**, 617-632.
17. K. W. Lem, A. Choudhury, A. A. Lakhani, P. Kuyate, J. R. Haw, D. S. Lee, Z. Iqbal and C. J. Brumlik, *Recent patents on nanotechnology*, 2012, **6**, 60-72.
18. O. H. Lowry, N. J. Rosebrough, A. L. Farr and R. J. Randall, *J. Biol. Chem.*, 1951, **193**, 265-275.
19. S. Pattanayak, A. Priyam and P. Paik, *Dalton Transactions*, 2013, **42**, 10597-10607.
20. J. S. Kim, E. Kuk, K. N. Yu, J.-H. Kim, S. J. Park, H. J. Lee, S. H. Kim, Y. K. Park, Y. H. Park, C.-Y. Hwang, Y.-K. Kim, Y.-S. Lee, D. H. Jeong and M.-H. Cho, *Nanomedicine: Nanotechnology, Biology and Medicine*, 2007, **3**, 95-101.
21. W.-R. Li, X.-B. Xie, Q.-S. Shi, H.-Y. Zeng, Y.-S. OU-Yang and Y.-B. Chen, *Applied Microbiology and Biotechnology*, 2010, **85**, 1115-1122.
22. M. Caza and J. W. Kronstad, *Frontiers in cellular and infection microbiology*, 2013, **3**, 80.
23. E. Deriu, J. Z. Liu, M. Pezeshki, R. A. Edwards, R. J. Ochoa, H. Contreras, S. J. Libby, F. C. Fang and M. Raffatellu, *Cell host & microbe*, 2013, **14**, 26-37.

CHAPTER 6: A FERRITIN PHOTOCHEMICAL SYNTHESIS OF MONODISPERSED PLATINUM AND PALLADIUM NANOPARTICLES

Abstract

The previous chapters show that our ferritin-based photo catalytic method was able to produce nanoparticles (NPs) from gold, mercury, and silver. Due to the great industrial interest in the platinum and palladium nanoparticles (hydrogen evolution, hydrogenation of olefins, catalytic activation of synthetic reactions, etc.) we decided to test whether the previously reported photo chemical method could be optimized for the synthesis of catalytically active monodispersed PtNPs and PdNPs. We report the production of 1-2 nm spherical PtNPs and PdNPs on the surface of ferritin. These nanoparticles remain stable in solution and do not precipitate for over one year. This chapter will focus on the synthesis of the particles, while the application will be described in the next chapter. UV-Vis spectrophotometry and transmission electron microscopy were used to follow the growth of the nanoparticles and analyze the products, respectively.

Introduction

Platinum and palladium are some of the most commonly used catalysts in the world. They are used in chemical synthetic processes, olefin reduction, production of high octane fuels, the reduction of the emission of toxic fumes from vehicles, the hydrogenation of vegetable oils, and in hydrogen evolution. Nanoparticles derived from these two precious metals have higher catalytic activity and lower cost than their bulk materials.^{1 2 3 4 5 6 7 8 9} Therefore, we decided to test whether the ferritin photo catalytic nanoparticle synthesis method could be used to synthesize platinum and palladium nanoparticles (PtNPs and PdNPs). The reduction potentials of Pt(II) to Pt(0) (+0.98 V) and Pd(II) to Pd(0) (+0.915 V) are consistent with the reducing power of our ferritin-citrate photo catalytic method, hence we were confident that our experiments should yield positive results.

This work describes the successful ferritin photo reduction of platinum and palladium metal ions in solution and the deposition of the reduced metals in the form of nanoparticles on the surface of ferritin. The nanoparticle characteristics are evaluated by transmission electron microscopy.

Materials and Methods

We obtained horse spleen ferritin (HoSF), potassium tetrachloroplatinate, and potassium tetrachloropalladate from Sigma-Aldrich. Ferritin protein concentrations were determined by the Lowry method¹⁰. The iron content of the native ferritin was 1800 Fe/Ftn as determined by the dithionite/bypyridyl method (Watt et al. 1992). The platinum and palladium metal nanoparticles (PtNPs and PdNPs) were formed by mixing Ftn (150 µg/mL) with TRIS buffer at pH 7.4 (30 mM), sodium citrate (30 mM), the noble metal salt (Pd²⁺ 4 mM; Pt²⁺ 2 mM) and NaCl (50 mM).

The PtNPs could be formed in the temperature range 25-70°C, whereas the PdNPs required a higher temperature (>60°C). The temperatures for the reactions were maintained in a water-jacketed cuvette holder in the Agilent 8453 spectrophotometer. 1 mL samples were placed in a quartz cuvette and exposed to a full spectrum Hg-halide floodlight (Integrated Dispensing Solutions, Inc.) and the reaction progression was monitored in the 200-1100 nm range in kinetic mode for the length of the reaction in a UV-Vis spectrophotometer (Agilent HP 8453). PdNPs and PtNPs were allowed to photo react for up to 2 hours and monitored at 330 nm and 320 nm, respectively. The appearance and size of the NPs was visualized and evaluated by transmission electron microscopy (TEM) performed on a Tecnai F30 operating at 300 kV.

Results

The photo catalytic formation of the nanoparticles was followed by monitoring the changes in the full absorbance spectrum for each metal (Fig. 1). As PdNPs form, an absorbance peak centered on 330 nm appears. The formation of PtNPs is characterized by an increase in the entire spectrum but with a peak around 320 nm. The solutions of the PdNPs and PtNPs changed from a pale yellow to a light brown or a dark brown color, respectively (Fig. 1).

TEM analysis of the Pt sample (Fig. 2) shows that PtNPs form and reach their final 1-2 nm size within 15 minutes. The images show that the PtNPs nucleate and remain attached to the ferritin protein shell (that surrounds the iron cores – larger faint spheres visible in Fig. 2). PdNPs start growing within 10 minutes and reach their full 1-2 nm size after about 30 minutes of illumination (Fig. 3). Like the PtNPs, PdNPs also nucleate and remain attached to the protein shell. For Pd samples, we observed that extended times of illumination (approximately an hour) resulted in the formation of more prismatic shape PdNPs.

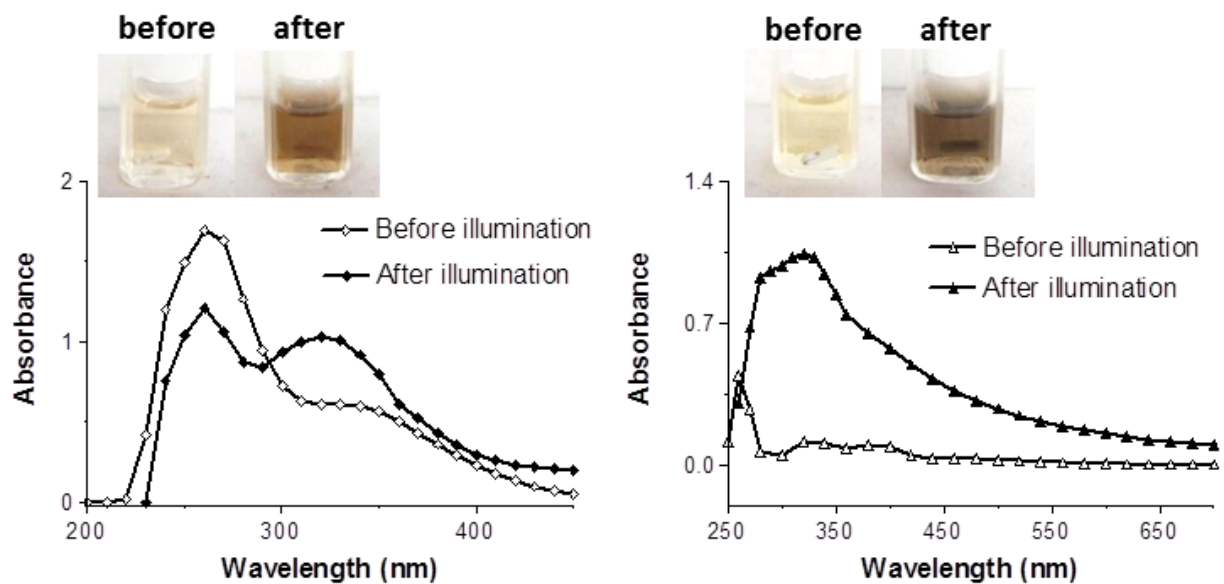


Figure 6-1. Pictures and spectra of the PdNP (left) and PtNP (right) samples before and after illumination. Spectral changes occur that are indicative of nanoparticle formation for each metal.

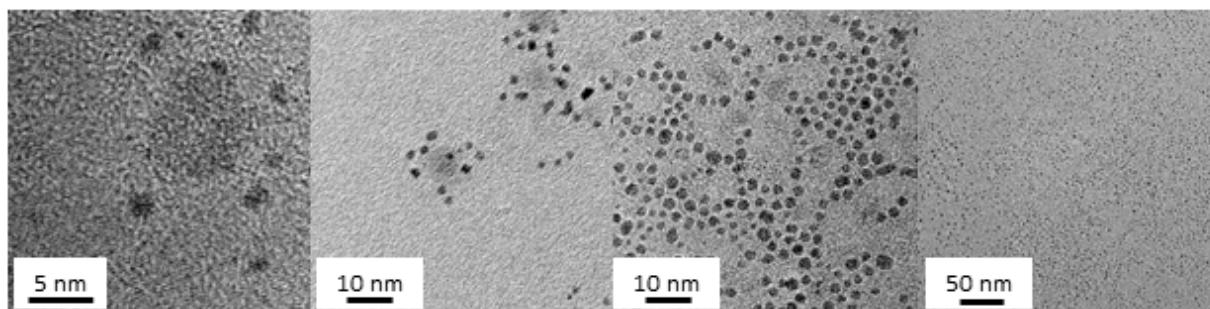


Figure 6-2. TEM micrographs of PtNPs. PtNPs are visible after 15 minutes of illumination (left image). The PtNPs assemble three dimensionally around the ferritin protein (of which only the iron core is visible as a lighter larger sphere) (two central images). The particles cover the entire surface of the TEM grid (far right image).

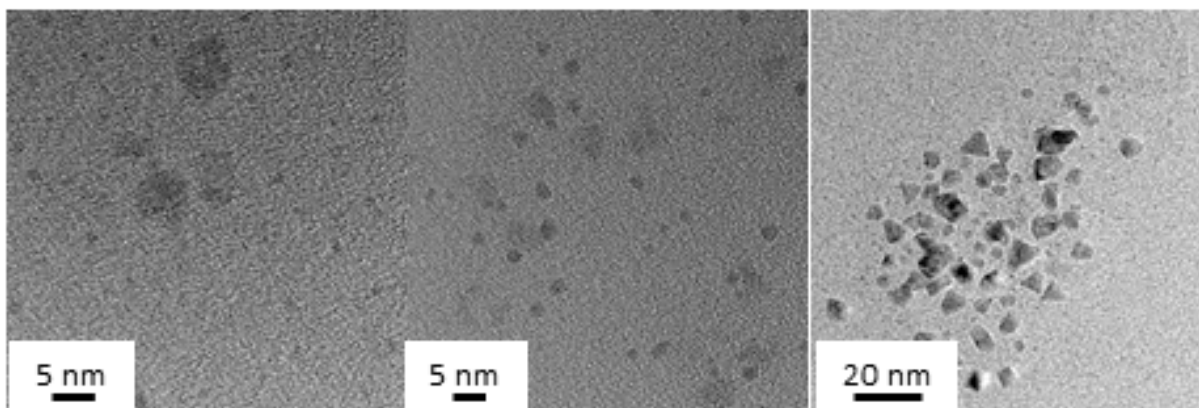


Figure 6-3. TEM micrographs of PdNPs. PdNPs are visible already after 11 minutes of illumination (left image) and reach their final size within 30 minutes (middle image). As with the PtNPs, the lighter larger spheres represent the iron core of ferritin. Illumination of Pd samples for longer periods of time resulted in prismatic nanoparticles (far right image).

Conclusions

We successfully synthesized PdNPs and PtNPs on the surface of ferritin. The particles are monodispersed 1-2 nm in size, which is reportedly the size that features the maximal catalytic ability for these noble metals.¹

References

1. M. Shao, A. Peles and K. Shoemaker, *Nano Letters*, 2011, **11**, 3714-3719.
2. Z. Guo, L. Hu, H.-h. Yu, X. Cao and H. Gu, *RSC Advances*, 2012, **2**, 3477-3480.
3. X.-F. Guo, D.-Y. Jang, H.-G. Jang and G.-J. Kim, *Catalysis Today*, 2012, **186**, 109-114.
4. M. Schwarze, J. Keilitz, S. Nowag, R. Y. Parapat, R. Haag and R. Schomacker, *Langmuir*, 2011, **27**, 6511-6518.
5. Q. Liu, J. Li, X.-X. Shen, R.-G. Xing, J. Yang, Z. Liu and B. Zhou, *Tetrahedron Letters*, 2009, **50**, 1026-1028.
6. J.-W. Park, Y.-M. Chung, Y.-W. Suh and H.-K. Rhee, *Catalysis Today*, 2004, **93-95**, 445-450.
7. Y. Niu, L. K. Yeung and R. M. Crooks, *Journal of the American Chemical Society*, 2001, **123**, 6840-6846.
8. R. J. Pellet, *Journal of Catalysis*, 1998, **177**, 40-52.
9. S. Golunski, *JOM*, 2001, **53**, 22-24.
10. O. H. Lowry, N. J. Rosebrough, A. L. Farr and R. J. Randall, *J. Biol. Chem.*, 1951, **193**, 265-275.

CHAPTER 7: PHOTOCHEMICAL EVOLUTION OF HYDROGEN BY METHYL VIOLOGEN

Abstract

Citrate and oxalate can be photo oxidized by illuminating these carboxylic acids in the presence of the electron mediator methyl viologen (MV). The reduced form of MV (MV_{red}) is a known electron donor in hydrogen evolution reactions when the appropriate catalyst is present, typically platinum. By combining these observations we have demonstrated hydrogen evolution by illuminating citrate and MV in the presence of a platinum catalyst. This work constitutes a simple model for hydrogen evolution.

Introduction

As the price of fossil fuels increases in response to limited supply, practical alternative energy sources become more urgent. Hydrogen gas (H_2) is a highly efficient energy source, as well as a carbon-neutral and clean fuel source because its only byproduct is water. However, current production of H_2 comes from fossil fuels, resulting in large volumes of CO_2 emissions.¹ Therefore, H_2 production from renewable biomass is currently being investigated.²

Many H_2 evolving photo-catalytic methods have been reported to convert solar energy into hydrogen, and they typically consist of a light absorber, a shuttle redox mediator, a sacrificial electron donor, and a catalyst for H_2 formation.^{3,4} A number of organo-metallic light absorbing complexes have been developed with various efficiencies, band gaps, and durability; these complex molecules are expensive and not immediately available on a large scale.³⁻⁵ The sacrificial electron donors utilized in most studies are not produced from natural sources on a large scale (e.g.: triethanolamine, EDTA).^{3,4,6} Finally, each step of a reaction reduces the efficiency, thus a method that requires fewer steps to move electrons from the electron donor to the protons in solution is desirable.

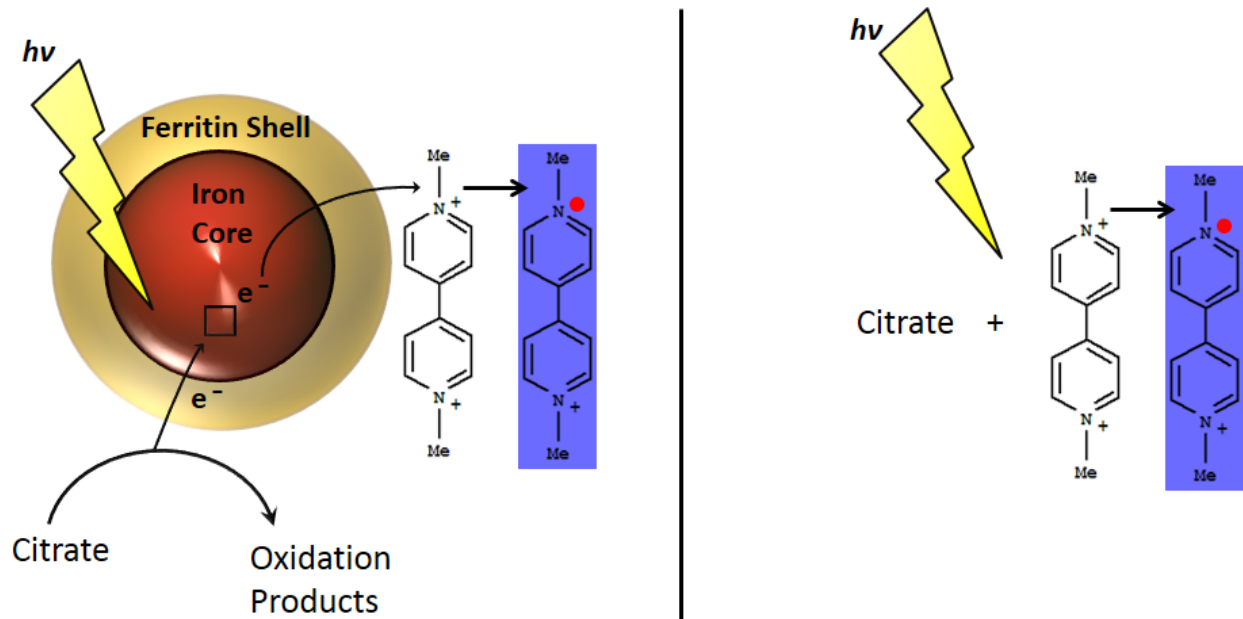
We report the discovery of a simplified system based on methyl viologen (MV), organic acids and a Pt catalyst. MV functions as both a light absorber and as an electron shuttle, and the organic acids as sacrificial electron donors, with Pt as the H_2 catalyst.

Reduced methyl viologen (MV_{red}) is known to have the right potential (-420 mV) to reduce H^+ ions and produce H_2 .⁷ Also, our laboratory has extensively used ferritin- (photocatalyst) -citrate (sacrificial electron donor) as a powerful reducing couple in a photochemical method to produce nanoparticles starting from a multitude of ionic metal ions (Au, Pt, Pd, Ag, Hg, Cu). Nikandrov demonstrated that this ferritin photochemical system could

also reduce proteins such as cytochrome c (+0.240 V) and redox dyes such as propyl viologen sulfonate (-0.36 V).⁸ Our initial goal was to test whether the ferritin-citrate photochemical system could achieve a sufficiently negative reducing potential to photo reduce methyl viologen (MV) under anaerobic conditions. The test was successful as the ferritin-citrate-MV solution turned blue after a few minutes of illumination under a full spectrum flood light. At this point we wanted to show that ferritin was essential in the photo-reduction of MV. To our surprise, this control sample containing only citrate and MV turned blue faster and reached a higher peak of absorbance than the sample where ferritin was present (Scheme 1). This chapter reports the results obtained from testing a series of conditions in the pursuit of maximizing the production of hydrogen gas from this three-component system.

Materials and Methods

The base system consisted of water, methyl viologen, and a sacrificial organic compound as an electron donor (e.g.: oxalate or citrate). The system was then placed under anaerobic conditions in gas-tight glass ampules by alternating between 5 cycles of vacuuming for 25 seconds and flushing with Ar gas for 15 seconds respectively with stirring. The ampules were then kept at 25°C in a water bath and irradiated with a 400 W mercury halide full spectrum flood lamp (Integrated Dispensing Solutions Inc.) with stirring for 30 minutes (unless stated otherwise) to produce H₂. The quantity of H₂ generated was measured using gas chromatography (GC) (Hewlett Packard Series II 5890) with a molecular sieve column (5A 80/100 #80473-810, Restek Co.) and using N₂ as carrier gas. The H₂ in the samples was quantified by comparing the



Scheme 7-1. Photo reduction of methyl viologen (MV) by ferritin (left quadrant) and control reaction without ferritin (right quadrant). MV was reduced in both reaction conditions, but in the absence of ferritin the reaction proceeded faster and reached a higher peak of absorbance.

sample peaks against standard gas mixture of 1000 ppm of H₂ in N₂ (Airgas Inc.). Various organic substrates, pH conditions, catalysts, irradiation times, temperatures, and concentrations of substrate, salt, MV, and Pt catalysts were investigated to determine their effects on H₂ production in the system.

We investigated a variety of organic substrates as sacrificial electron donors that include oxalate, citrate, tartrate, gluconate, glucose, succinate, fumarate, glycerol, glyceraldehyde, and dihydroxyacetone, all at pH 4. Separate oxalate samples at different pH, ranging from 2–5 were tested. Concentrations of NaCl and KCl ranging from 25–500 mM were investigated with the base system. Concentrations of oxalate and citrate ranging from 25–500 mM were investigated. Methyl viologen concentrations ranging from 1–40 mM were investigated. Concentrations of platinum nanoparticles (PtNP) synthesized in the lab ranging from 0.1–40 ppm were investigated. Concentrations of commercially available and known H₂ evolving catalysts Pt-black and Pd-black (Sigma-Aldrich, cat. #205915 and # 520810) ranging from 1–10 ppm were also investigated.

Results

The photochemical evolution of hydrogen gas with MV was tested using oxalate as the electron donor in the pH range 2-5 and showed maximal efficiency at pH 4 (Fig. 1) with the PtNP catalyst. Oxalate solutions at pH 4 produced between 0.7 and 12 times more H₂ than the other investigated pH conditions, with the general results resembling a bell-shaped curve (Fig. 1). However, the optimal pH for H₂ production may vary with other electron donors. After H₂ production was quantitated, the pH of the resulting solution was measured and found to be

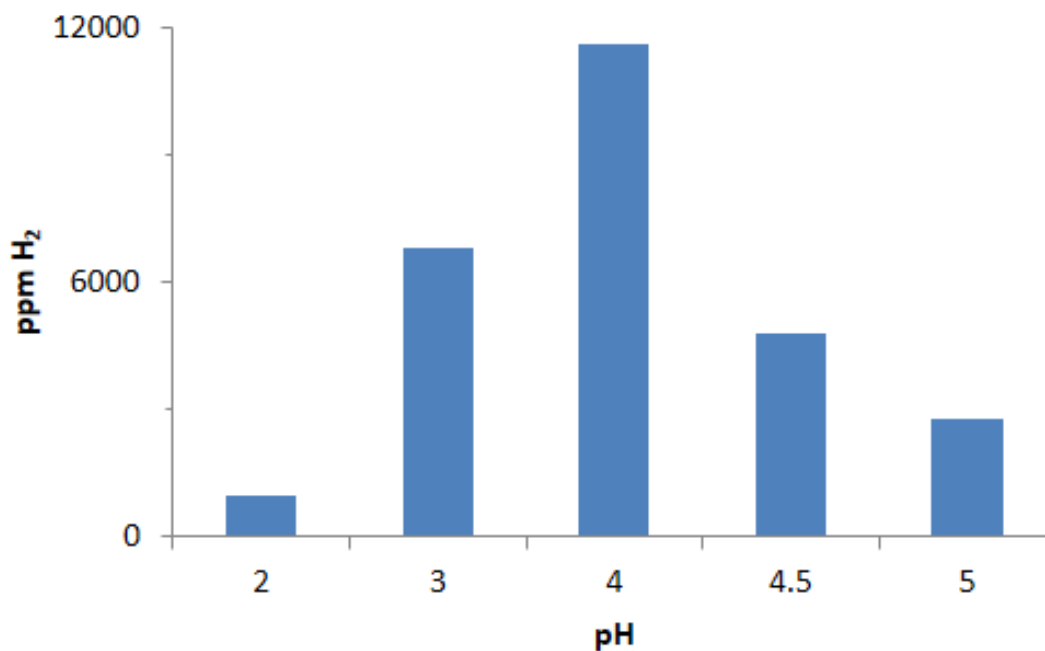


Figure 7-1. pH Dependence on hydrogen evolution. Hydrogen evolution was tested using oxalate as the electron donor in solutions at different pH values. The pH maximum for hydrogen evolution is observed at pH 4. The reactions contain 200 mM oxalate, 2.5 mM MV, 1 ppm PtNP, but no NaCl (30 min irradiation time).

typically 1–2 units higher than the starting pH.

Oxalate was the best electron donor among those selected (Fig. 2). Other carboxylic acids were able to reduce protons; among these are citrate, tartrate, and gluconate, whereas dihydroxyacetone, fumarate, glucose, glyceraldehyde, glycerol, and succinate did not generate appreciable amounts of H₂ at pH 4. Oxalate, citrate, tartrate, and gluconate yielded significant amounts of H₂ (Fig. 2). Because oxalate produced more H₂ than the other substrates investigated, all subsequent experiments conducted in this study used oxalate as the electron donor unless stated otherwise.

Hydrogen evolution is known to be catalyzed by platinum group metals. Our first tests were carried out using platinum foil or platinum grid materials. The H₂ evolved increased by at least ten fold in the presence of Pt foil and even more with Pt grid compared to the non-catalyzed reaction (data not shown).

Knowing that a greater catalyst surface area increases the performance of a catalyst we decided to test the H₂ evolution mediated by commercially available platinum black (Pt-black) and palladium black (Pd-black) (Fig. 3). The use of these large surface area noble metal catalysts greatly improved the production of hydrogen.

Next we wanted to see how the platinum nanoparticles (PtNP) synthesized in our laboratory (see Chapter 6) would behave (Fig. 4). Various concentrations of the PtNP catalyst were tested showing that 10 ppm of PtNP was the optimal concentration for H₂ evolution (Fig. 4).

By comparing the H₂ yield by Pt-black, Pd-black or PtNP at various concentrations we concluded that the PtNP catalyst is the most efficient at producing H₂ under our reaction

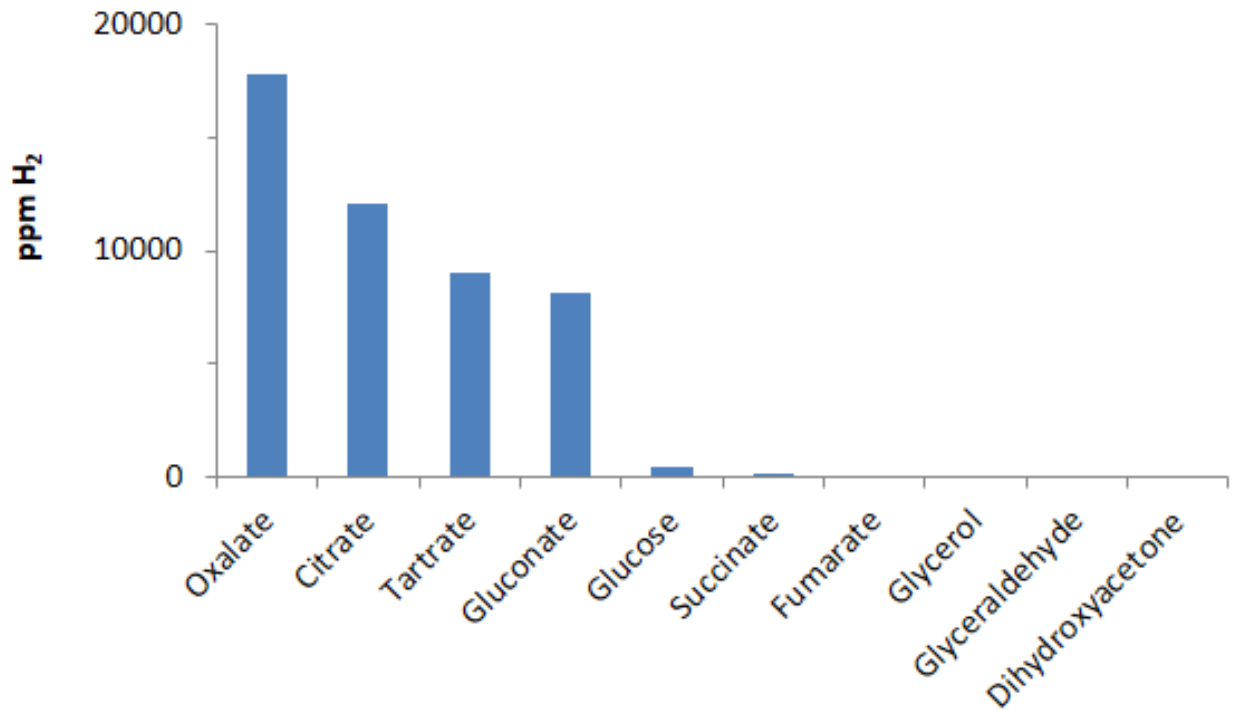


Figure 7-2. Hydrogen Production. Assay conditions are 100 mM of various electron donors at pH 4.0, with 2.5 mM MV, 50 mM NaCl, 1 ppm PtNP (30 min irradiation time). Oxalate produces more H₂ than the other donors investigated. Citrate, tartrate, and gluconate are feasible electron donors as well.

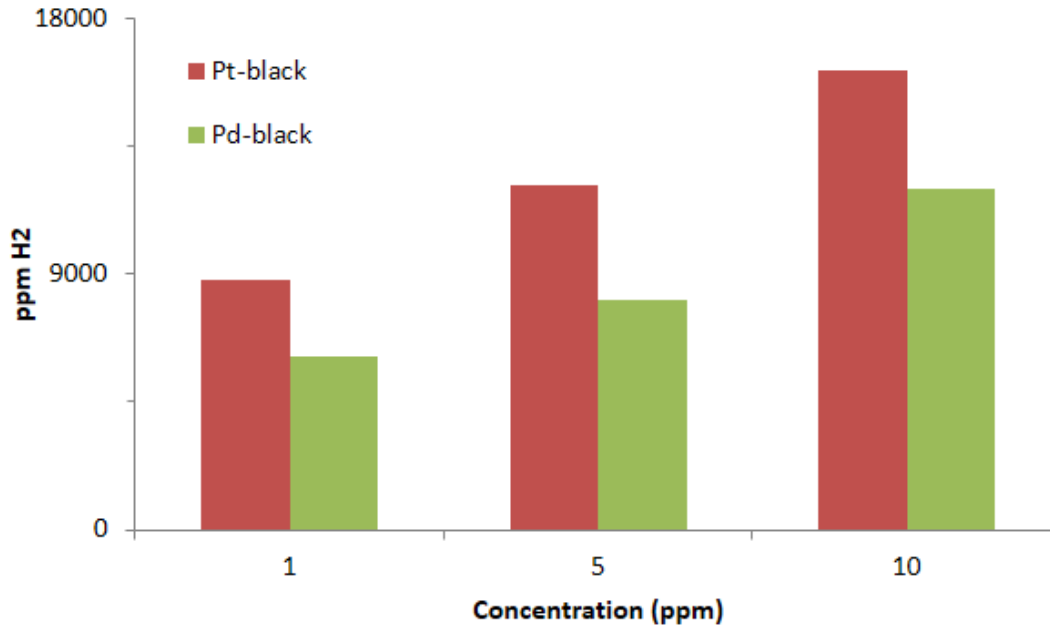


Figure 7-3. Hydrogen evolution by various concentrations of commercial Pt-black or Pd-black, in the presence of 150 mM oxalate pH 4, 2.5 mM MV, 50 mM NaCl (30 min irradiation time).

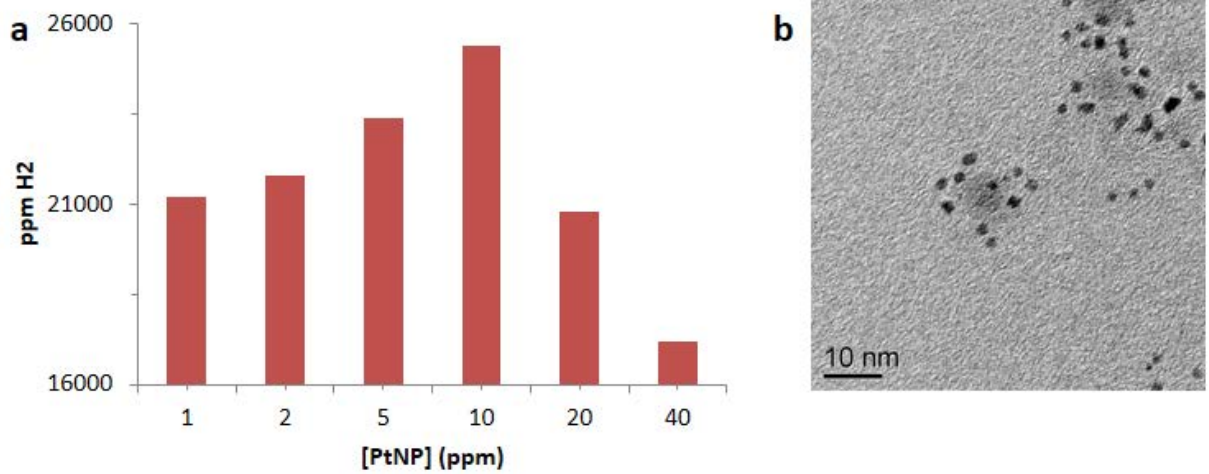


Figure 7-4. (a) Hydrogen evolution as a function PtNP concentrations with 0.5 M oxalate pH4, 2.5 mM MV, 50 mM NaCl (30 min irradiation time). This graph indicates that 10 ppm of PtNP is the optimal concentration for maximum H₂ yield. Beyond concentrations of 10 ppm, the ferritin present in solution (used to synthesize and cap the PtNP) begins to absorb a significant number of photons. (b) PtNP (small dark dots) attached to the ferritin protein shell (only the grey 8 nm iron cores are visible) visualized by TEM. The AuNPs measure 1-2 nm in diameter.

conditions with 1 ppm of the PtNP catalyst producing 2.4 and 3.4 more H₂ than the same concentrations of Pt-black or Pd-black, respectively. The H₂ produced in the presence of 0.1 ppm of PtNP is comparable to that produced by 100 fold more Pt- or Pd-black (Fig. 5).

It was postulated that ionic salts in solution might assist the shuttling of electrons from the sacrificial donor to the protons in solution; therefore, we investigated the effect of various concentrations of NaCl and KCl and found that 50 mM of NaCl and 100 mM KCl were equally optimal conditions, both enhancing H₂ production (Fig. 6). The alkaline earth metals were also tested at different concentrations. Figure 7 summarizes the significant results obtained: while higher concentrations of Mg²⁺ or Ca²⁺ reduce the production of H₂, small amounts of CaCl₂ (5 mM) improve the production of H₂ by about 15%, when compared to the NaCl or KCl previously tested. Seeing that larger ions tend to be more effective enhancers of H₂ production, we decided to test other divalent metal ions including strontium, copper and zinc. We report that 5 mM strontium produced the highest amount of H₂, that copper was comparable to magnesium, while zinc produced no H₂ (Fig. 8). We do not have a model at this time to justify these observations; therefore, these results leave the door open to further mechanistic studies.

We tested the concentration dependence of oxalate (electron donor) on H₂ production. As expected, increasing the concentration of oxalate increased the yield H₂. Therefore, H₂ production is restricted by solubility limits of the electron donor. The change in slope after a sharp, initial rise from 25–100 mM is due to the H₂ pressure build-up in the reaction vessel and proton consumption (Fig. 9). Additionally we varied the concentration of citrate as the electron donor and demonstrated the same trend as oxalate (Figure 10). The effect of methyl viologen concentration was also evaluated for its effect on H₂ yield (Fig. 11).

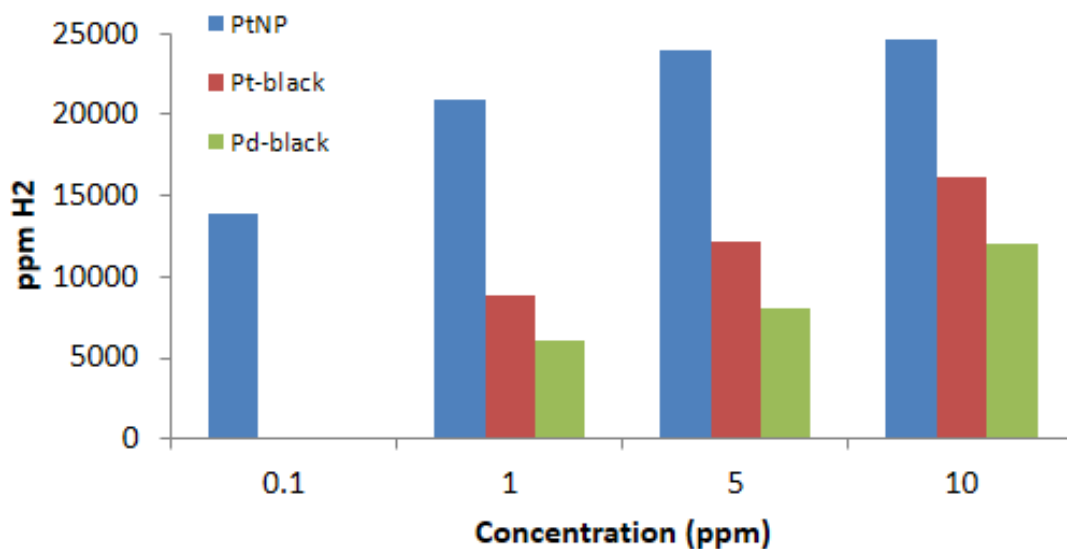


Figure 7-5. Hydrogen evolution by various concentrations of PtNP synthesized by our laboratory vs. commercial Pt-black or Pd-black, in the presence of 150 mM oxalate pH 4, 2.5 mM MV, 50 mM NaCl (30 min irradiation time). 1 ppm of PtNP produces 2.4 and 3.4 more H₂ than the same concentrations of Pt-black or Pd-black, respectively. The H₂ produced by 0.1 ppm of PtNP is comparable to that produced by 100 fold more Pt- or Pd-black.

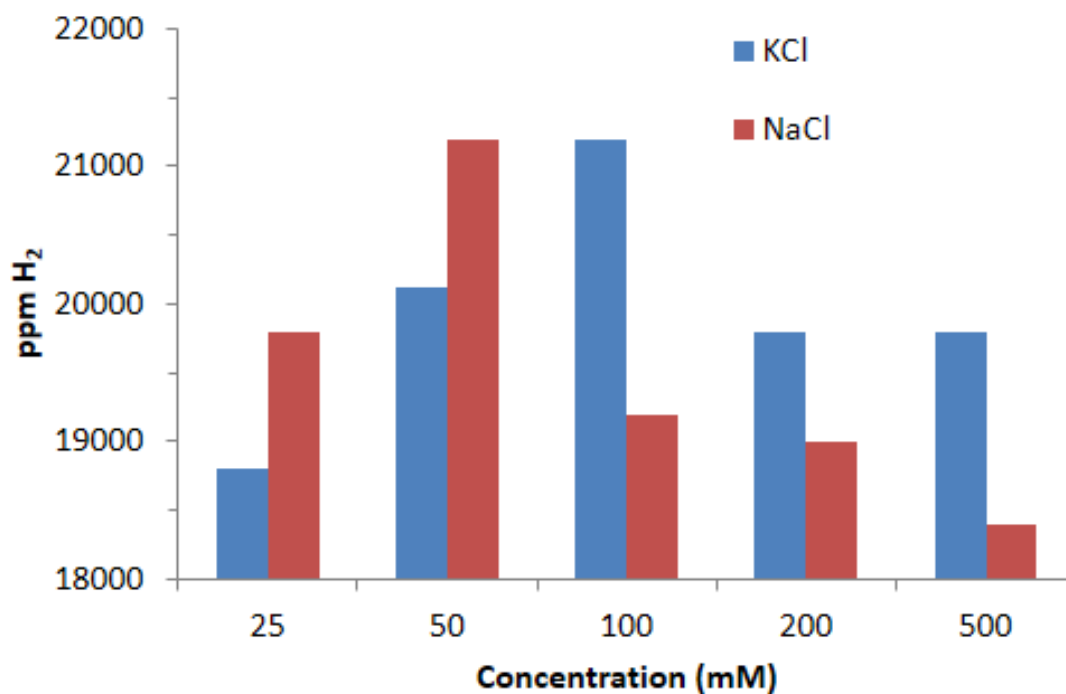


Figure 7-6. The effect of salt on hydrogen evolution. Hydrogen evolution as a function of salt concentrations in the presence of 100 mM oxalate pH4, 2.5 mM MV, and 1 ppm PtNP (30 min irradiation time).

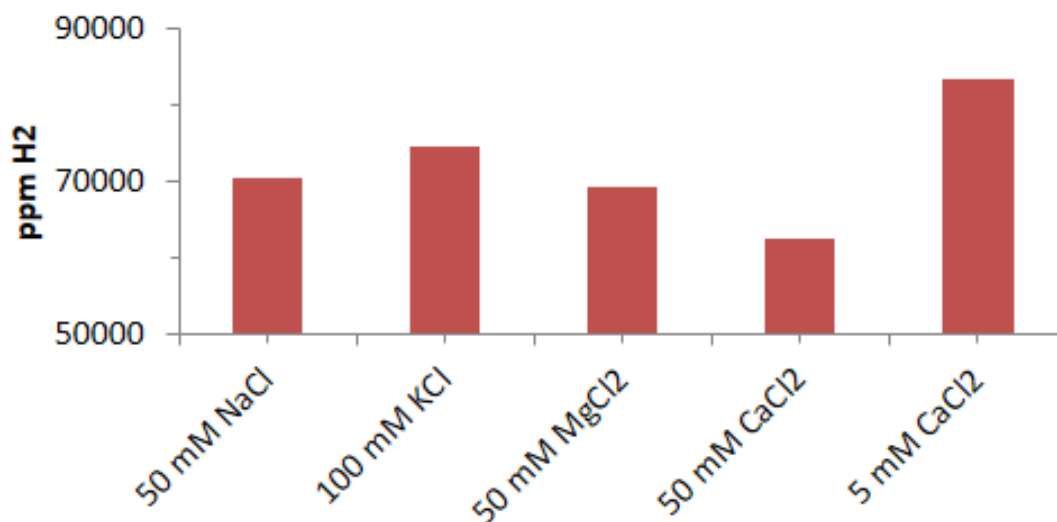


Figure 7-7. Influence of various ions over hydrogen production in the presence of 0.5 M oxalate pH4, 10 mM MV, and 10 ppm PtNP (30 min irradiation time). Mg- and Ca-oxalate compounds tend to precipitate; higher concentrations of Ca²⁺ and Mg²⁺ were tested for comparison with the reference Na⁺ and K⁺; lower concentrations of Ca²⁺ increase the reaction yield by about 15% when compared to NaCl or KCl (far right column).

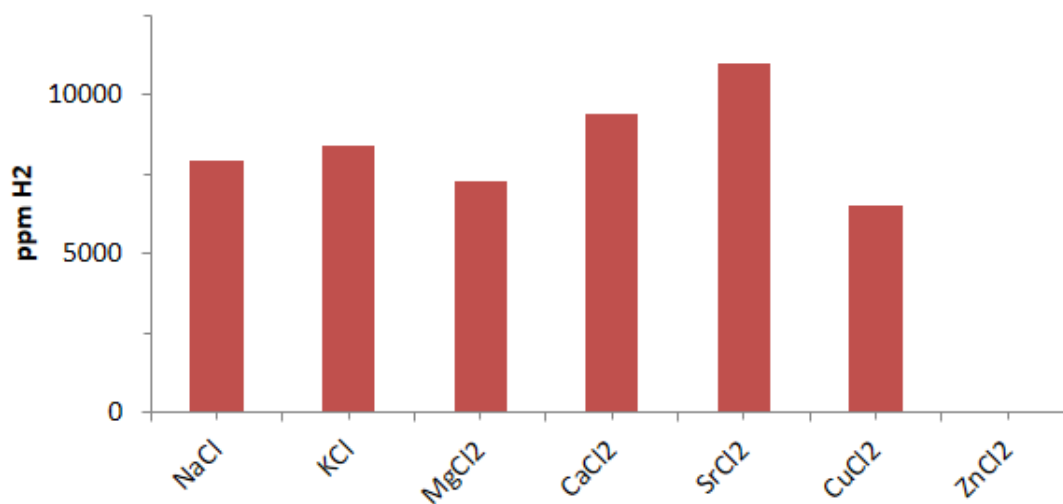


Figure 7-8. Influence of other alkaline-earth ions over hydrogen production in the presence of 0.625 M oxalate pH4, 40 mM MV, and 10 ppm PtNP (5 min irradiation time). NaCl and KCl are present at 50 mM and 100 mM, respectively; all other ions are present at 5 mM concentrations.

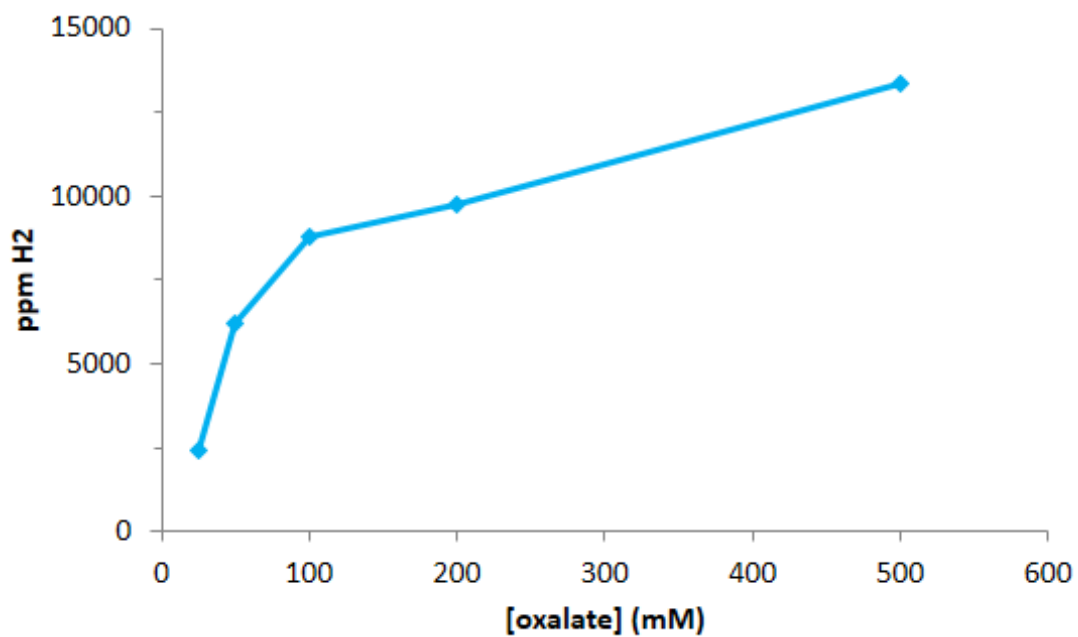


Figure 7-9. Hydrogen evolution as a function of the concentration of oxalate at pH 4 with 40 mM MV, 5 mM CaCl₂, 10 ppm PtNP (5 min irradiation time).

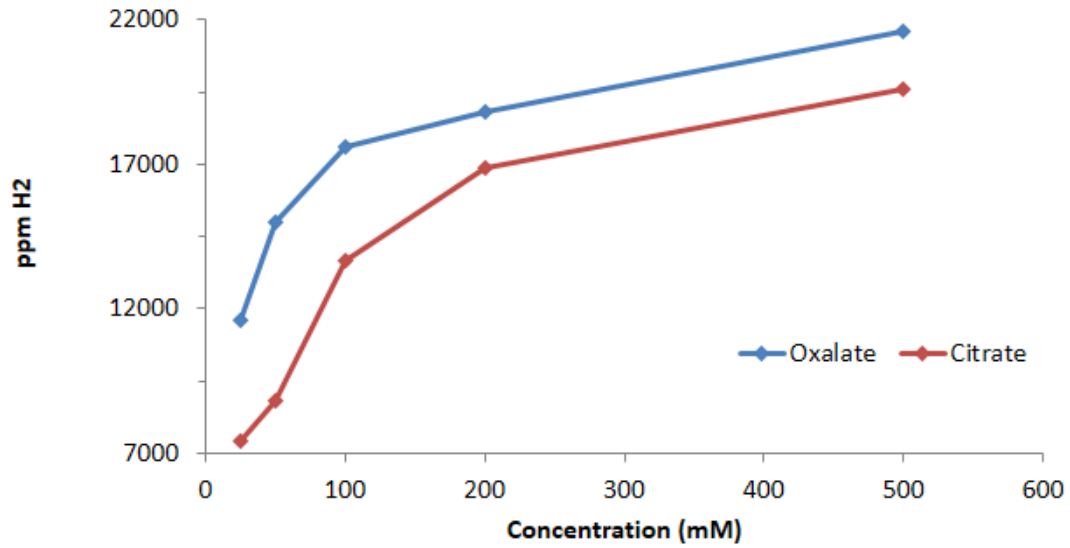


Figure 7-10. Production of hydrogen dependent on the concentration of oxalate vs. citrate pH 4 (30 min irradiation time).

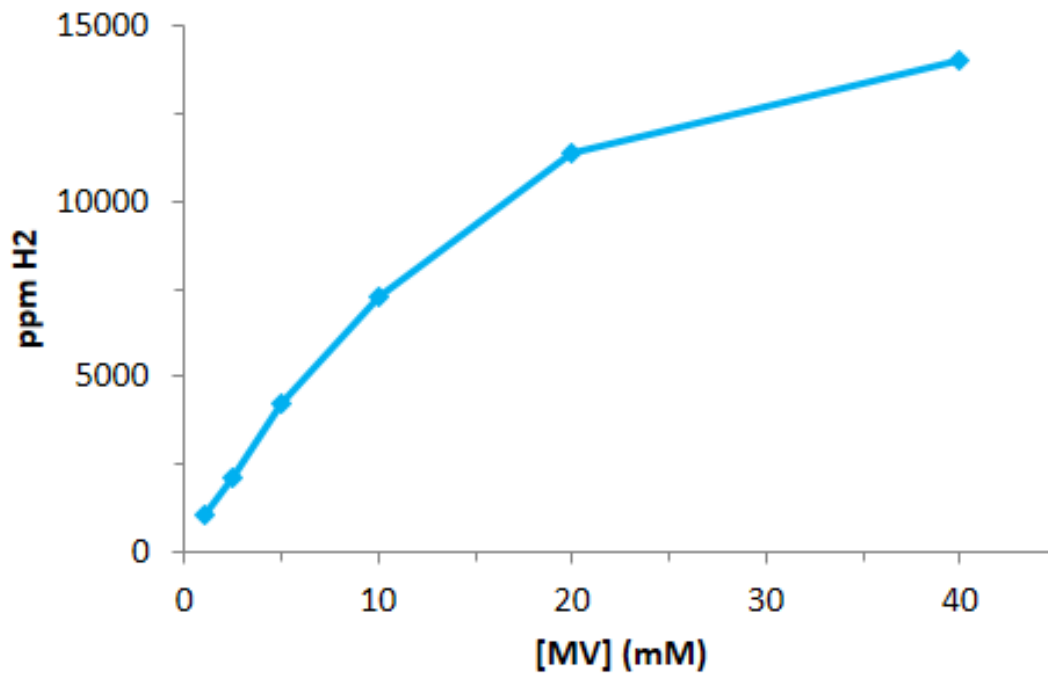


Figure 7-11. Hydrogen evolution as a function of the concentrations of MV with 0.625 M oxalate, 5 mM CaCl₂, 10 ppm PtNP (5 min irradiation time).

In the effort of maximizing the production of hydrogen, the kinetics of hydrogen production as a function of light exposure time was evaluated. Figure 12 shows the results of such experiments from which three important pieces of information can be extracted: first, as expected, the reaction rate slows down as the reaction proceeds, due to the accumulation of the products and consumption of protons; second, a 45 minutes light exposure represents the time limit for our experimental set up, when the formation of H₂ is almost completely halted (close to equilibrium); third, the slope of the initial part of the curve allows the calculation of the initial rate of H₂ formation, which is ~59.2 ppm H₂/sec (3550/min). This number can be used in the ideal gas law to calculate the moles H₂/sec produced by 2 mL of solution, as follows:

$$PV = nRT \leftrightarrow n = PV/RT \quad (1)$$

$$\frac{1 \text{ atm} \times 2 \times 10^{-3} \text{ L/headspace}}{0.08206 \times 298.15 \text{ K}} = 8.17 \times 10^{-5} \text{ mol gas/headspace} \quad (2)$$

Multiplying this number by the ppm of the H₂ contained in the 2 mL sample allows the calculation of the total number of H₂ moles produced by it:

$$\frac{8.17 \times 10^{-5} \text{ mol gas}}{\text{headspace}} \times \frac{59.2 \text{ parts}}{1 \text{ million} \cdot \text{sec}} = 4.83 \times 10^{-9} \text{ mol H}_2/\text{sec} \quad (3)$$

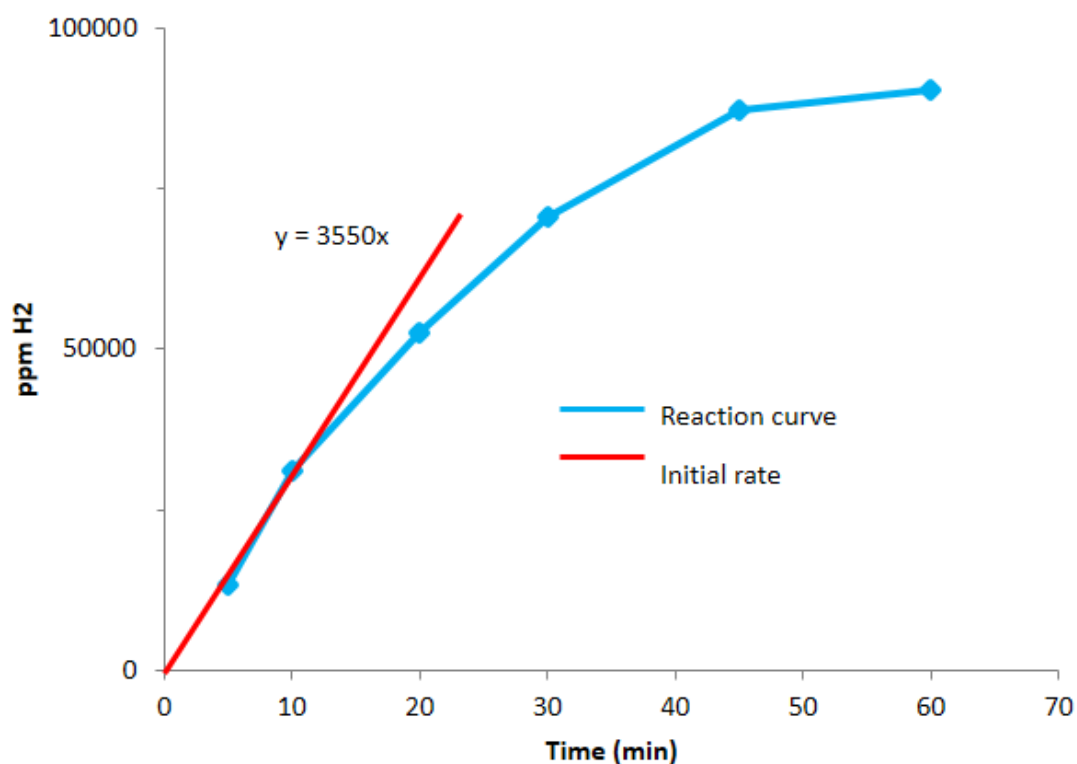


Figure 7-12. Hydrogen evolution as a function of light exposure time at 0.5 M oxalate pH 4 with 2.5 mM MV, 50 mM NaCl, 10 mM MV, and 10 ppm PtNP. The initial rate of formation is 3550 ppm H₂/min (red intercept and equation on the graph) or 59 ppm H₂/sec. As the reagents are consumed and the products formed the curve becomes logarithmic (blue line and black dotted trend line and relative R² value).

The result from eq. 3, corrected for the local atmospheric pressure (Provo, UT: average pressure = 0.85 atm), equals 4.11×10^{-9} mol H₂/sec.

The result of equation 2 can be used to calculate the total H₂ produced by each sample by simply multiplying by the final ppm of H₂ produced.

Conclusions

This paper proposes a simplified method to reduce protons to H₂ through a light driven reaction composed of methyl viologen, platinum and oxalate. The advantages of this technique are that all the reagents are easily attainable: methyl viologen is produced on large scale as herbicide, and constitutes a robust and affordable photo-catalyst that, unlike other light harvesting systems, does not require additional electron shuttles to transfer the reducing equivalents to the H₂ catalyst.^{9, 10 4, 11, 12} Platinum is an expensive catalyst and significant research efforts have been dedicated to substitute it with cheaper and more abundant metal compounds that catalyze H₂ evolution.^{4, 5, 12-15} Our laboratory has optimized a method to synthesize PtNP that show up to 100 fold more activity than traditional Pt- or Pd-black catalysts, thus allowing the reduction of the costly H₂ catalyst by up to 100 fold. In future studies we propose to synthesize and test other cheaper H₂ evolving catalysts such as PdNP and NiNP by the ferritin photochemical method (see Chapter 6). The carboxylic acids we have tested are affordable, commonly found in nature and therefore potentially attainable from renewable sources. Oxalate and gluconate are particularly interesting electron donors: the first has the advantage of leaving no byproducts other than CO₂; the second is easily produced by a single

step air oxidation of glucose performed in 30 minutes at room temperature in a solution containing gold.¹⁶

A down-side of the method described in this paper is that methyl viologen absorbs light in the UV spectrum. We suggest that the modification of methyl viologen by the substitution of the methyl groups with longer conjugated groups may shift the absorbance into the more abundant visible spectrum of the solar radiation.¹⁷

The H₂ evolution reaction described in this work could be combined with other water oxidation reactions (evolving O₂) described previously^{3-5, 11-13, 18, 19} to finally reach a potentially efficient water splitting method that uses abundant biomass and solar radiation as renewable resources for the production of H₂ fuel.

References

1. K. Christopher and R. Dimitrios, *Energy & Environmental Science*, 2012, **5**, 6640-6651.
2. S. Freni, G. Calogero and S. Cavallaro, *Journal of Power Sources*, 2000, **87**, 28-38.
3. V. Artero and M. Fontecave, *Comptes Rendus Chimie*, 2011, **14**, 799-810.
4. R. Abe, *Journal of Photochemistry and Photobiology C: Photochemistry Reviews*, 2010, **11**, 179-209.
5. Q. Yin, J. M. Tan, C. Besson, Y. V. Geletii, D. G. Musaev, A. E. Kuznetsov, Z. Luo, K. I. Hardcastle and C. L. Hill, *Science*, 2010, **328**, 342-345.
6. H. A. F. Werner and R. Bauer, *Journal of Photochemistry and Photobiology A: Chemistry*, 1996, **97**, 171-173.
7. Z. Varpness, J. W. Peters, M. Young and T. Douglas, *Nano Letters*, 2005, **5**, 2306-2309.
8. V. V. Nikandrov, C. K. Gratzel, J. E. Moser and M. Gratzel, *J Photochem Photobiol B*, 1997, **41**, 83-89.
9. K. Sayama, K. Mukasa, R. Abe, Y. Abe and H. Arakawa, *Chemical Communications*, 2001, 2416-2417.
10. K. Sayama, K. Mukasa, R. Abe, Y. Abe and H. Arakawa, *Journal of Photochemistry and Photobiology A: Chemistry*, 2002, **148**, 71-77.
11. R. Abe, K. Sayama and H. Sugihara, *The Journal of Physical Chemistry B*, 2005, **109**, 16052-16061.
12. K. Maeda and K. Domen, *The Journal of Physical Chemistry Letters*, 2010, **1**, 2655-2661.

13. Z. Zou, J. Ye, K. Sayama and H. Arakawa, *Journal of Photochemistry and Photobiology A: Chemistry*, 2002, **148**, 65-69.
14. A. Das, Z. Han, M. G. Haghghi and R. Eisenberg, *Proceedings of the National Academy of Sciences*, 2013.
15. V. Artero, M. Chavarot-Kerlidou and M. Fontecave, *Angewandte Chemie International Edition*, 2011, **50**, 7238-7266.
16. W. Luo, C. Zhu, S. Su, D. Li, Y. He, Q. Huang and C. Fan, *ACS Nano*, 2010, **4**, 7451-7458.
17. K. Tanabe, T. Yasuda, M. Yoshio and T. Kato, *Organic Letters*, 2007, **9**, 4271-4274.
18. J. J. Pijpers, M. T. Winkler, Y. Surendranath, T. Buonassisi and D. G. Nocera, *Proc Natl Acad Sci USA*, 2011, **108**, 10056-10061.
19. Y. Surendranath, M. W. Kanan and D. G. Nocera, *Journal of the American Chemical Society*, 2010, **132**, 16501-16509.

CHAPTER 8: CONCLUSIONS AND OUTLOOK

In the introduction I talked about two goals, that I named “Holy Grails”, that I pursued with my research: Artificial Photosynthesis and Low Temperature Biomass Oxidation. Throughout this dissertation I have shown that ferritin is a feasible medium to reach these goals. In the process of better understanding ferritin photochemistry and electron transfer, I was able to produce size controlled nanoparticles from the noble metals gold, silver, platinum, and palladium. I have also shown that these nanoparticles are catalytically active.

Ferritin was also able to reduce mercury and precipitate it out of solution. This method could be employed for decontamination purposes.

Finally, we demonstrated the evolution of hydrogen by the simple photo oxidation of naturally occurring carboxylic acids like oxalic acid, citric acid, gluconic acid, and tartaric acid, mediated by methyl viologen.

The results described in this dissertation open the way to further research that should pursue the following four goals: first, trying to better understand the nanoparticle nucleation and growth on ferritin; second, discovering in more details ferritin photochemical electron transfer mechanism; third, test the quantum yield of the hydrogen production by the oxalate-methyl viologen method and improve the efficiency of the hydrogen evolution by fine tuning the variables already applied in Chapter 7 and testing viologens able to absorb light in the visible spectrum; fourth, split water by coupling our hydrogen evolution system to oxygen oxidizing catalysts.

Artificial Photosynthesis could be right around the corner.